WAVE EMISSION FROM HETEROGENEITIES FOR LOW-ENERGY TERMINATION OF CARDIAC ARRHYTHMIAS

A Dissertation

Presented to the Faculty of the Graduate School

of Cornell University

in Partial Fulfillment of the Requirements for the Degree of

Doctor of Philosophy

by

Amgad Andrew Squires

Januaray 2011

WAVE EMISSION FROM HETEROGENEITIES FOR LOW-ENERGY TERMINATION OF CARDIAC ARRHYTHMIAS

Amgad Andrew Squires, Ph.D.

Cornell University 2011

Cardiac fibrillation is a leading cause of death in the modern world. Its treatment has so far been limited to painful and damaging defibrillation shocks. In this thesis, we experimentally investigate the possibility of using low-energy electric pulses to terminate fibrillation.

We built two high-resolution fluorescence optical mapping systems to investigate the phenomenon of wave emission from heterogeneities in *in vitro* canine cardiac tissue preparations and whole rabbit hearts. The activation sequence from single pulses of varying amplitude was captured and quantified. The global activation time is found to obey a power-law with exponent -0.5 in rabbits and -0.15 in canines. We also present a novel model of tissue activation based on the density of wave sources within the tissue, valid for both 2d and 3d.

Using data from CT scans of our tissue preparations, we found that the size distribution of the cardiovasculature also follow a power-law distribution over an order of magnitude, with scaling exponents -1.8 in canines and -2.13 in rabbits. Our model of activation time links the activation time with the size distribution via their scaling exponents.

Finally, we tested the hypothesis that anti-fibrillation pacing (AFP) can terminate ventricular fibrillation with lower pulse energy than conventional defibrillation. We found an 81 % reduction in pulse energy in canine experiments. We saw no such reduc-

tion in rabbit hearts, suggesting additional interactions between the fibrillatory activity and the far-field induced wave emission.

Our results are presented as a contribution to our understanding of excitable systems and to the development of new treatment approaches in clinical cardiology.

BIOGRAPHICAL SKETCH

Amgad Andrew Squires grew up in Burundi and in Eastern Canada. After receiving his high school diploma from Nancy Campbell Collegiate Institute in 1998 and spending a year of service at the New Era Development Institute in India and touring Southwestern Ontario with the Wildfire Dance Theatre, he attended Mount Allison University in Sackville, NB in 1999. In 2003, he received a Bachelor of Science degree in Physics and Mathematics. The same year, he entered the Physics department of Cornell University where, after a brief stint in network theory, he joined the research group of Professor Bodenschatz in 2005.

This thesis is dedicated to my family, especially my parents, without whose unfailing love and support this thesis would have never seen the light,
and to the thousands and millions whose suffering inspires us to strive every day a little more.

ACKNOWLEDGEMENTS

Thank you first of all to my thesis advisor, Prof. Eberhard Bodenschatz, who taught me to value even the smallest accomplishments and to pursue one's work with passion. My thanks also to my coadvisors: Prof. Robert Gilmour, whose skill, kindness and generosity are recognized by all, and Prof. Paul Ginsparg, whose enthusiasm and natural curiosity first attracted me to biophysics. I cannot adequately thank Dr. Stefan Luther. He has been a mentor, an exemplar, and a strong pillar. From him I learned that true encouragement requires patience, and that perseverance and conviction truly can overcome great obstacles. Prof. Valentin Krinsky is extremely generous in sharing his extensive knowledge and experience. From him I learned to make ideas as clear and as simple as possible, and to focus on what is most important, even at the expense of what is important.

Prof. Valentin Krinsky and Prof. Alain Pumir's theory of wave emission from heterogeneities (WEH) [1] and their subsequent proposal to leverage WEH in order to implement multisite pacing [2] provided the theoretical foundation on which this thesis stands. To both of them: my deepest thanks and admiration.

I would be remiss if I did not acknowledge the many exceptional individuals who have been guides and mentors along the way: Prof. Ahmady and all the physics faculty at Mount Allison University, my dear teacher Ms. Brenda Radford, my uncle Sherif and aunt Shaku who, in opening their home to me in India, also opened my eyes to the life of the majority of the people of the world, and the distinguished speakers at countless physics conferences as well as Baha'i conferences and schools.

Needless to say, a life is shaped by the thousands of people we meet, who fill our days with joy and wonder. Whether in a brief encounter or a long-lived friendship, their impact reverberates for years. Special thanks to those with whom I have shared these seven years of my life. First, to my lab mates: Claudia R., Philip B., Johannes

S., Jan W., Jan C., Dong-Xia W., Alexander S., Daniel H., Mohammed C., Tariq B., Anna B., Alexander A. and Marion K.! I also want to thank all my fellow students in Ithaca and Göttingen, without whom late-night assignments and Friday night dinners would have been terribly lonely. Special mention to my roommates over the years: Gabriel P., Chris J., Mohammed H., Gabriel A. and Dario V., whom I thank for their patience and generosity (thanks for all the food guys!) and for their sense of humour and understanding. A special note of thanks to the administrative staff on both sides of the ocean: your superb administrative skills and generosity of spirit made life in a foreign country incredibly easier. You went out of your way to accommodate an unusual circumstance and I am deeply grateful.

I should additionally like to thank the Baha'i communities of Canada, of the United States and of Germany, particularly those of Sackville, Stratford, Ithaca, Göttingen and Hanover, for opening your lives and your hearts to someone passing through. You were at times a refuge, a fountain of joy and a refreshing breeze, and I am eternally grateful for all that I have learned from you.

To all those whom space was insufficient to acknowledge by name: thank you for sharing of yourselves with me, and may your paths be richly blessed.

Finally, I wish to thank my incredible family from the bottom of my heart: Mom, Dad, Munir and Jamila, Nonna, the Hannahs, the Rushdys, the Squires and the Klassens. I love you all and I am proud to be a part of you. Thank you for believing in me when I did not believe in myself, for lifting me up when I fell down, for suffering with me through the lows and celebrating with me every high, for lifting my vision beyond the next step towards the vast and promising future, for your counseling voice in times of need and your strong bulwark when the going got tough. May you be everlastingly blessed and rewarded, in both this life and in the life to come.

TABLE OF CONTENTS

LIST OF TABLES

LIST OF FIGURES

LIST OF ABBREVIATIONS

NR	=	Normal Rhythm
NSR	=	Normal Sinus Rhythm
VF	=	Ventricular Fibrillation
VT	=	Ventricular Tachycardia
AF	=	Atrial Fibrillation
AT	=	Atrial Tachycardia
APD	=	Action Potential Duration
WEH	=	Wave Emission from Heterogeneities
WES	=	Wave-Emitting Site(s)
FFP	=	Far Field Pacing
VE	=	Virtual Electrode
IVE	=	Intramural Virtual Electrode
CT	=	Computerized Tomography
LED	=	Light-Emitting Diode
CMOS	=	Complementary Metal-Oxide Semiconductor
(EM)CCD	=	(Electron Multiplication) Charge-Coupled Device

LIST OF SYMBOLS

Table 1: List of symbols with units and typical scale

Symbol	Description	Unit	Scale
ϕ_i	intracellular potential	V	10^{-1}
ϕ_o	extracellular potential	V	10^{-1}
V_m	membrane potential	V	10^{-1}
R_m	membrane resistance	$\Omega \cdot$ cm	10
C_m	membrane conductance	F	10
v_c	conduction velocity	m/s	10^{-1}–10^{0}
$\varrho_{2d/3d}$	2- or 3-dimensional density	m^{-2} or m^{-3}	
N	number of WES	–	10^{0}–10^{3}
R	heterogeneity radius	m	10^{-5}–10^{-3}

CHAPTER 1

INTRODUCTION

The physical universe that surrounds us is filled with fascinating phenomena that we seek to understand. Our own bodies are like miniature universes too, with processes occurring at every scale: ions are pumped across membranes, cells are transported through the bloodstream, tissues heal and regenerate, the brain learns and adapts, the body ages and decays. Science gives us the tools to investigate these phenomena, to ask how these processes occur, what drives them and, when they malfunction, to find out why.

One very important function in the body is the pumping of the heart. This organ is again like a little universe unto itself. For most people, the heart carries out its evolutionarily-assigned task silently and efficiently through their entire lives, never quitting and rarely complaining. A significant number of people, however, are prone to arrhythmias, disruptions of the heartbeat that leave them gasping for breath, or worse. For many, the only remedy is a large, painful electrical shock that resets the heart's rhythm.

For over a hundred years, doctors and scientists have sought together to understand the electrical workings of the heart's rhythms, normal and abnormal [4]. In the process, physicists have developed a whole toolbox to explain and investigate the electrical activity of the heart. These tools combine elegant mathematical models of excitable media with careful experimental observations in order to better understand this highly complex system.

In this thesis, we set out to understand better the effects of external currents on the heart. We pursued this primarily via experiments on animal hearts. Experimental studies of the heart received a great boost with the discovery of fast voltage-sensitive dyes in the 1980s, by means of which the electrical activity of the heart could be imaged, at least

on the surface. However, accessing the electrical activity inside the bulk of the heart remains an unsolved challenge.

We set out to find means of seeing into the dark, as it were, by combining advanced pacing and imaging setups with a simple, robust model of bulk cardiac tissue activation in response to homogeneous electric fields. In effect, we will probe the heart with electric field pulses and use the optical recordings from the surface to infer the electrical activity within the heart tissue. Along our journey, we will draw on concepts from biology, nonlinear systems, and chaos control, to name but a few.

We begin with an introduction to the anatomy and mechanics of the heart, restricting ourselves to those details most relevant to our purposes.

1.1 Anatomy and Mechanics of the Heart

The heart is an incredible machine: it pumps about 5 litres of blood per minute—or 7000 litres per day—and beats over 2 billion times during an average human lifetime.

It is made up of four chambers. The two upper chambers are the atria and they serve as collection chambers for blood arriving to the heart. Blood returning from the body is collected in the right atrium while blood from the lungs is collected in the left atrium. The two lower chambers are the ventricles; they are larger than the atria because they provide most of the mechanical force that creates the pressure difference that pumps blood through the arteries. The right ventricle (RV) supplies blood to the lungs while the left ventricle (LV) supplies it to the rest of the body. Figure 1.2 shows the main anatomical features of the heart and how blood flows through them. The heart itself is supplied by coronary arteries (not shown) that branch off of the aorta as it exits the heart. The inner surface of the heart chambers is the endocardium and the outer surface is the epicardium.

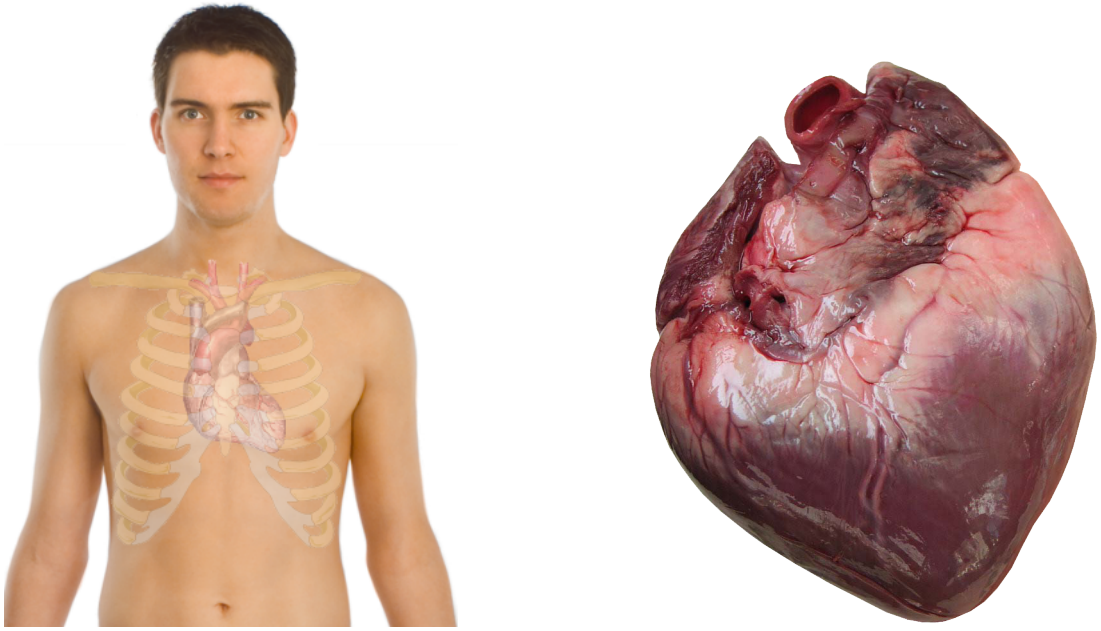

(a) (b)

Figure 1.1: **The human heart.**
(a) Location of the heart in the body.
[http://commons.wikimedia.org/wiki/File:Surface_anatomy_of_the_heart.png]
(b) The human heart. [http://www.officialpsds.com/HUMAN-HEART-PSD25142.html]

The cells responsible for the heart's contraction are specialized muscle cells called cardiomyocytes. Like most muscle cells, cardiomyocytes are shaped like elongated cylinders approximately 10 μm in diameter and 100 μm in length. Cardiomyocytes are arranged end-to-end in fibers, these fibers lie side-to-side in sheets, and the sheets are stacked one on top of the other. The fiber orientation in each sheet rotates by $\sim$120° between the endocardium and the epicardium. As the heart contracts, the rotating fiber orientation produces a twisting or wringing motion that enhances the mechanical pumping of the heart, more powerfully squeezing blood out of the chambers and into the body.

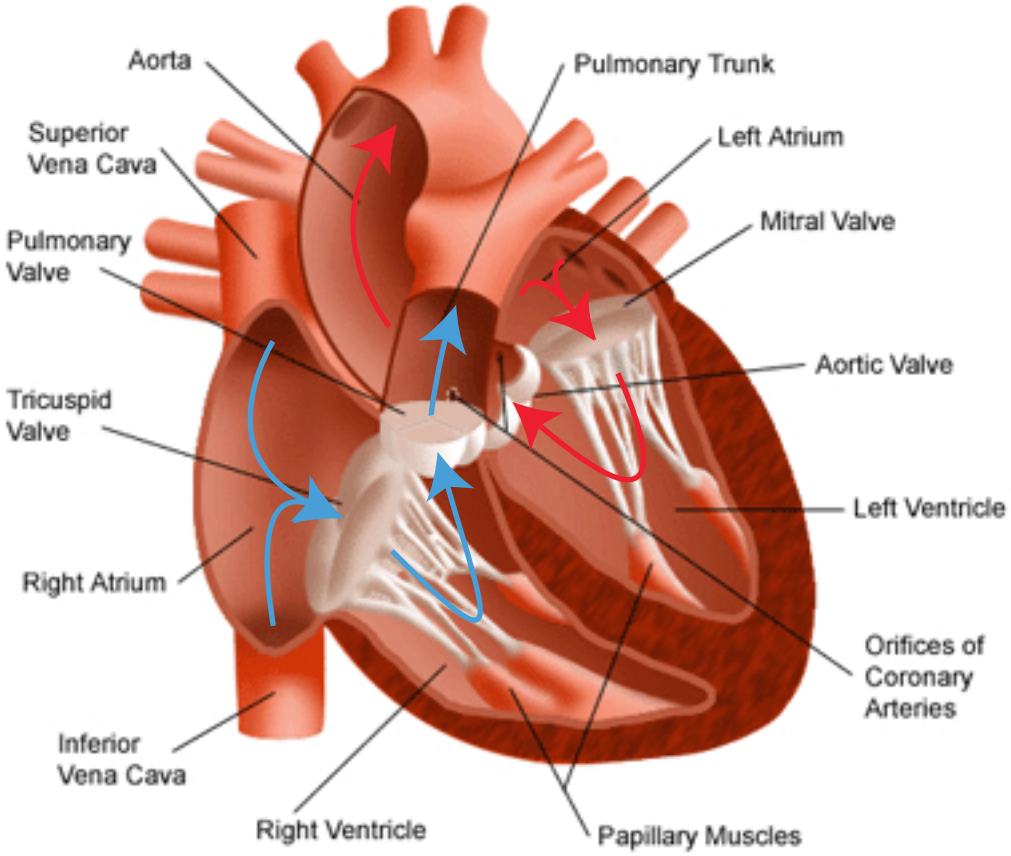

Figure 1.2: **Heart anatomy.**
Cutaway showing main anatomical features of the heart and flows of oxygenated (red arrows) and deoxygenated (blue arrows) blood. The heart has four chambers: two thin-walled atria above (upper left here) and two thick-walled ventricles below (lower right here). [http://www.biologycorner.com/anatomy/circulatory/images/heart02.gif]

1.1.1 Structures in the Heart

The heart is a heterogeneous, highly structured arrangement of cardiomyocytes and fibroblasts, blood vessels and extracellular matrix. It consists of a hierarchy of structures from the organ down to the cell level. Spanning almost this whole range of scales is the branching vascular system that transports blood throughout the heart muscle. Blood vessel walls are made of epithelial cells (as in skin). Epithelial cells have no gap junctions, no electrical connections to cardiomyocytes, so they act as heterogeneities in the

cardiac electrical system. Figure 1.3 shows the network of arterial blood vessels branching from the aorta. This vascular system resembles a fractal tree, with smaller arteries branching away from larger ones, from the aorta all the way down to capillaries.

We would like to know the size distribution of these blood vessels. For this purpose, we collaborated with Daniel Hornung, from the Biomedical Physics research group (BMPG) of Stefan Luther at the Max Planck Institute for Dynamics and Self-Organization (MPIDS) in Göttingen, Germany, to obtain microscopic computerized tomography (microCT) scans of rabbit hearts.

An example of the measurements of the cardiovasculature in whole rabbit hearts using microCT—with a barium sulfate contrast agent first injected into the coronary arteries—is shown in figure 1.4. The barium sulfate contrast agent filled about 5 % of the ventricular myocardium volume. Using an automated algorithm, Hornung identified all non-muscle structures and computed their radius [5].

The relative distribution of vessel radii $p(R)$ from rabbit hearts is plotted on logarithmic axes in figure 1.5. The data seem to follow a straight line between 0.05 mm and 0.7 mm, suggesting they follow a power-law distribution. Fitting a power law of the form $p(r) \propto R^{-b}$ gave an exponent $b_{rabbit} = 2.13$.

A similar procedure was repeated for canine right ventricle, this time with the assistance of Flavio Fenton and colleagues in the Department of Biomedical Sciences at Cornell University (Ithaca, NY, USA), and of Philip Bittihn in the Biomedical Physics Group at the Max Planck Institute for Dynamics and Self-Organization (Göttingen, Germany). The exponent for the distribution of blood vessel sizes in canine right ventricle was $b_{canine} = 1.8 \pm 0.05$ (between 0.07 and 0.7 mm), as shown in figure 1.5.

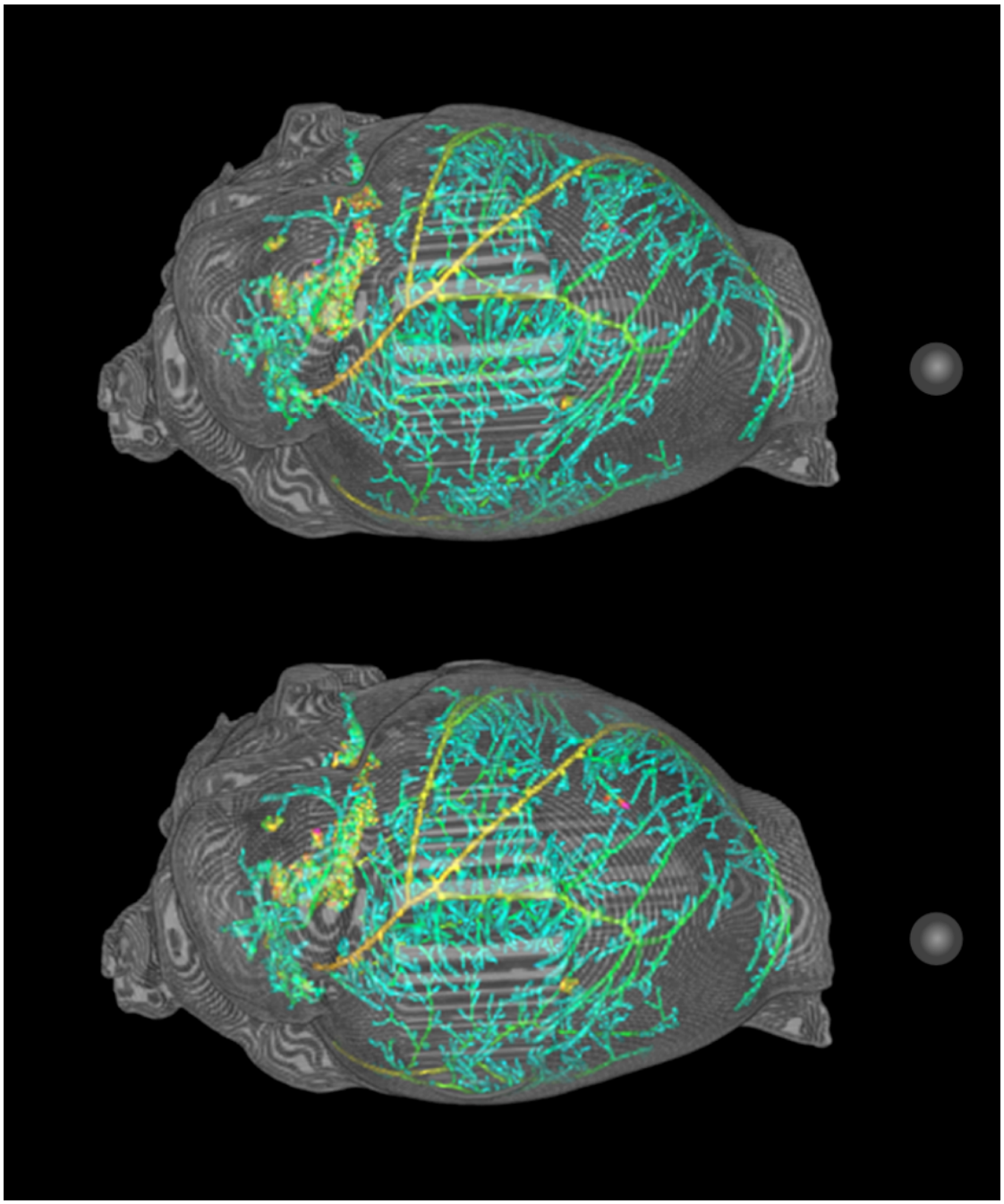

Figure 1.3: **Rabbit cardiovasculature.**
Stereoscopic view of rabbit arterial system colour-coded by size: largest to smallest vessels are colored red-yellow-green-blue. The greyscale surface is the outer surface of the heart. The image has been rotated by 90° CCW so that the top of the heart points to the left on the page. The bottom of the heart (apex) doesn't look "pointy" as it should because the heart was imaged in air and some fluid pooled around the bottom (right in the image). Image courtesy of D. Hornung.

Figure 1.4: **Example of heart structure imaging.**
MicroCT scan of a rabbit heart with barium sulfate contrast agent injected into the coronary arteries. The main coronary arteries are seen branching away from the aorta at the top of the image. The large grey mass in the center of the image is the left ventricle. Small grey bubbles (mostly in the top right) were caused by vessels that burst during contrast agent injection. Image courtesy of D. Hornung.

1.1.2 The action potential

Action potential (AP) waves begin at the level of the cell. Cardiomyocytes maintain ion concentration gradients across their outer membranes via ion pumps. These concentration gradients in turn give rise to a membrane voltage difference. This potential difference can be computed using the Goldman-Hodgkin-Katz equation, a generalization of the Nernst equation to multiple monovalent ionic species:

$$E_m = \frac{RT}{F} \ln\left(\frac{\sum_i^N P_{A_i^+}[A_i^+]_{out} + \sum_i^M P_{B_i^-}[B_i^-]_{in}}{\sum_i^N P_{M_i^+}[M_i^+]_{in} + \sum_i^M P_{B_i^-}[B_i^-]_{out}} \right). \tag{1.1}$$

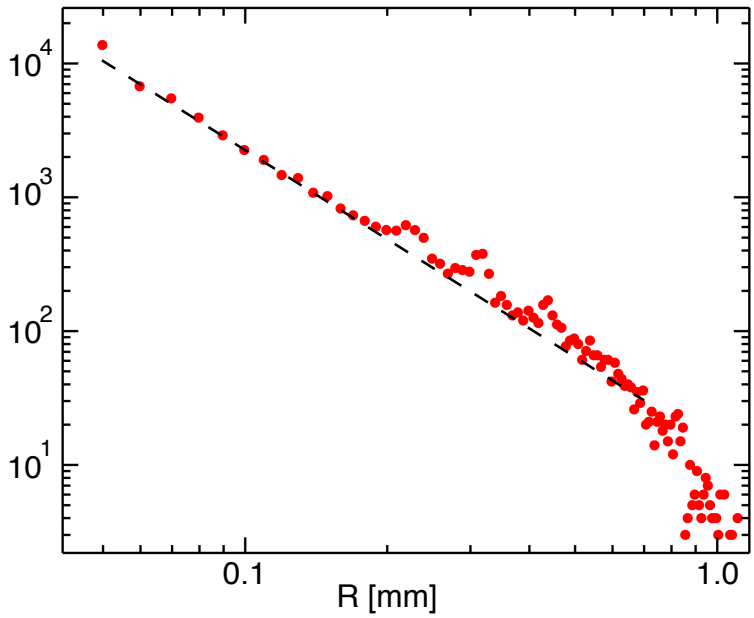

(a)

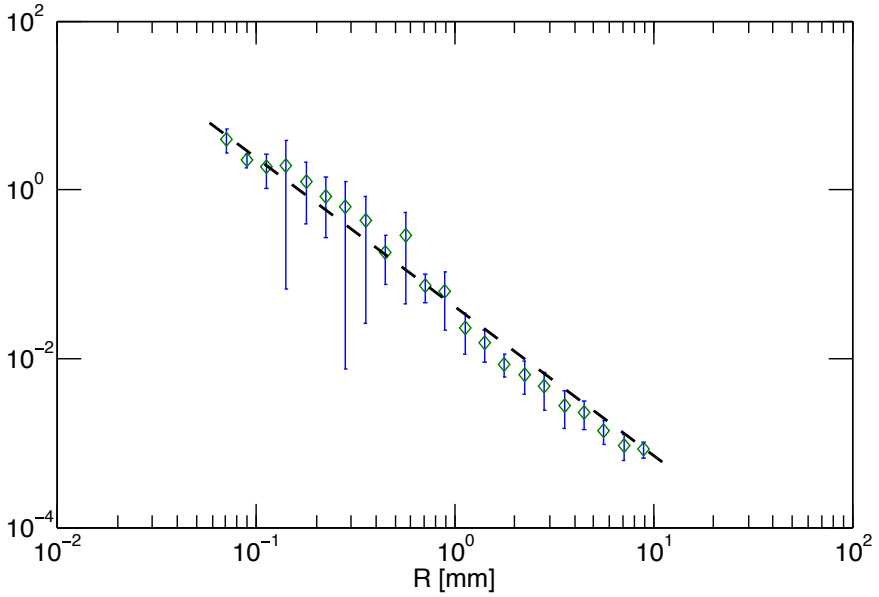

(b)

Figure 1.5: Size distributions of structures in the myocardium.
(a) Arterial cardiovasculature size distributions in rabbit hearts (n = 3). (Courtesy of D. Hornung).
(b) Probability distribution of the number of heterogeneities as a function of size in canine ventricles. Error bars are standard deviations. (Courtesy of P. Bittihn). The data are well fit by the power law $N \propto R^{-b}$ with $b = 1.80$ (canine) and $b = 2.13$ (rabbit) over the range 0.05 to 0.7 mm.

Considering the three most important monovalent ions, Na^+, $K^+$and Cl^-, and using human body temperature ($T = 37°C$), it gives the membrane potential as

$$E_m = -61.5\text{mV} \cdot \log_{10}\left(\frac{P_{Na}[Na^+]_o + P_K[K^+]_o + P_{Cl}[Cl^-]_i}{P_{Na}[Na^+]_i + P_K[K^+]_i + P_{Cl}[Cl^-]_o}\right). \tag{1.2}$$

Including the contributions from multivalent ions such as Ca^{2+}requires solving a higher-order equation.

Table 1.1 gives the internal and external concentrations of the four most common ionic species (and the resulting Nernst potential of each). Under normal conditions, the ion concentrations remain nearly constant. Thus the membrane potential changes when the permeabilities change, which occurs when ion-specific membrane channels open or close. At equilibrium, cardiomyocytes are more permeable to potassium than to other ions so the resting membrane voltage is around −85 mV.

The cellular membrane is highly impermeable to charged ions. The membranes of cardiomyocytes contain ion-selective, voltage-sensitive channels through which the cell can exchange ions with its surroundings. When these channels open or close, the membrane permeability of the associated ion increases or decreases. The selective flow of ions across the membrane is a function of the ion gradients and the selective permeabilities of the membrane. Changes in ion flows cause the membrane to become more or less negative, depending on the relative flux of anions and cations across the membrane.

Heart cells are vulnerable to perturbations of their membrane potential. Perturbations with amplitudes larger than +25 mV (the threshold) trigger an action potential, a sequence of events at the cellular level lasting about 300 ms and composed of three major phases. During an action potential, shown schematically in figure 1.6, the membrane rapidly depolarizes (phase 0), plateaus (phase 2), then slowly repolarizes (phase 3) to its resting value (phase 4). The first phase is the upstroke: Na^+ permeability increases by several orders of magnitude, causing the membrane voltage to depolarize in only a few milliseconds, then permeability decreases again because of channel inactivation. The

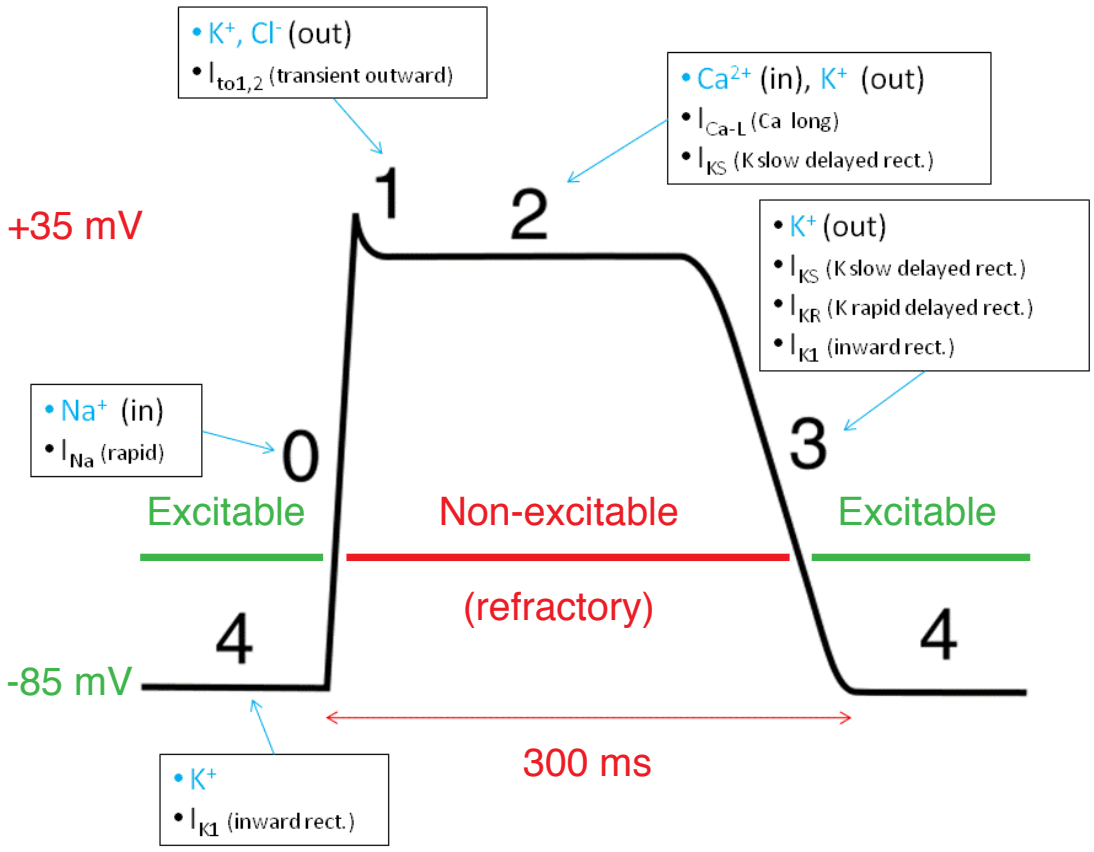

Figure 1.6: Cardiac action potential.
The membrane potential as a function of time during a cardiac action potential follows the time course sketched above. Na^+ currents during phase 0 rapidly depolarize the excitable cell. K^+ and Ca^{2+} currents during phase 2 maintain a plateau of membrane potential before a different set of currents slowly repolarizes the cell membrane during phase 3. The action potential duration is about 300 ms during normal sinus rhythm. The cell is not excitable (refractory) during phases 1–3 and excitable when it is at rest in phase 4.

second phase is the plateau of membrane potential, during which Ca^{2+} and K^+ permeabilities are both high. The inward and outward ion fluxes balance each other so that the membrane remains depolarized. The duration of phase two varies depending on the heart rate and other factors; under normal conditions, it is about 300 ms but this can shorten to as little as 50 ms during fibrillation. The third and final phase is the repolarization, during which calcium channels close, reducing permeability, and remaining outward K^+ flux repolarizes the membrane to its resting potential, ready for the next action potential.

The sharp depolarization in phase one, characteristic of cardiac action potentials, also determines the conduction velocity of the action potential wave front. Larger membrane potential gradients lead to faster wave propagation which helps keep the heart's contraction synchronized.

Table 1.1: Extracellular and intracellular concentrations of the primary ions involved in the cardiac action potential and their Nernst potentials.

	Extra [mM]	Intra [mM]	Ratio	Nernst Potential [mV]
Na^+	140	20	7:1	+52
K^+	4	120	1:30	-91
Cl^-	100	25	4:1	-37
Ca^{2+}	2	10^{-4}	2×10^4:1	+132

The contraction of a cardiomyocyte begins with cell membrane depolarization. As current enters the cell (usually through gap junction proteins: channels that connect the intracellular space of neighbouring cardiomyocytes), the membrane voltage rises until voltage-sensitive sodium channels open. When the channels open, the membrane permeability to Na^+ ions increases by several orders of magnitude. The opening of sodium channels produces a sharp depolarization of the membrane because of the large $[Na^+]$ gradient and associated Nernst potential.

Cardiomyocytes are electrically connected to their neighbours via gap junctions, protein channels. The gap junction density is highest near the ends of the cells, so that electrical resistivity is lowest in the cell's longitudinal direction (parallel to the fiber orientation). The effect of fiber orientation on electrical wave dynamics and on defibrillation shocks has been the subject of many studies. See for example the papers by Fenton and Karma [6] and by Trayanova *et al*. [7].

1.1.3 Electrical conduction pathways

To pump blood efficiently, the heart chambers have to contract in the correct sequence: atria first and ventricles about 100 ms later. Furthermore the contraction of each chamber has to occur within a few tens of milliseconds at most, to ensure maximum force generation. To do this the heart's electrical rhythm must follow a specific pattern of activation. This is accomplished via a set of specialized conduction pathways that ensure that the atria and the ventricles contract when required.

The single-cell action potential can propagate from cell to cell via the gap junctions that connect them, forming waves of electrical excitation that propagate across the heart, triggering its contraction.

A heartbeat begins at the atrial sinus node (ASN), a small group of oscillatory cells in the right atrium. From the ASN, an AP wave spreads across the atria. When the AP wave reaches the atrioventricular node (AVN), conduction slows to allow the atria to contract before the ventricles. After passing through the AVN, the AP wave is rapidly conducted through specialized conduction fibers down the interventricular septum (via left and right bundle branches) and then from apex to base through the outer ventricle walls (via Purkinje fibers) so that the ventricles contract synchronously. The normal sequence of events is thus ASN→atria→AVN→bundle branches→Purkinje fibers→ventricles, as shown in figure 1.7.

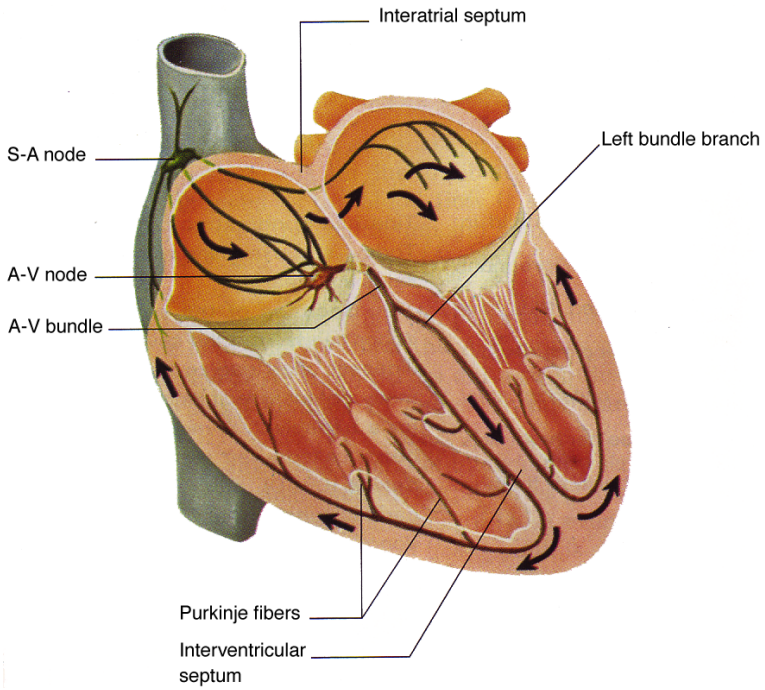

Figure 1.7: Conduction system of the human heart. See section 1.1.3 for description of the conduction pathways. Reproduced from [3].

1.1.4 Rhythm disorders

Heart rhythm disorders, also called cardiac arrhythmias, are a leading cause of mortality and morbidity in the developed world [8]. Although exact statistics are not available, it is widely believed that approximately 300,000 people die of Sudden Cardiac Death in the United States every year, almost 1000 deaths per day.

Deviations from the normal activation pattern described in section 1.1.3 range from the benign skipped beat or extra beat to the debilitating or lethal fibrillation. The former are transient whereas the latter are sustained disturbances of the normal rhythm. Rhythm disorders interfere with the normal pumping cycle of the heart. The most debilitating (though sadly not uncommon) arrhythmias are ventricular tachycardia (VT) and ventricular fibrillation (VF).

VT and VF are characterized by spiral waves (transient or sustained; see also section 1.2.3) [9, 10]. The period of rotation of spiral waves in heart tissue is shorter than the heart's normal period. Consequently, the spiral wave acts as a higher-frequency source that overtakes the rhythm set by the sinoatrial node (the heart's natural pacemaker). This condition is called tachycardia and is characterized by a fast, yet regular, rhythm. Tachycardia typically is not in itself a lethal condition: the pumping of blood continues, albeit with reduced efficiency. Ventricular tachycardia (VT), however, often degenerates into ventricular fibrillation.

Ventricular fibrillation (VF) is a spatio-temporally chaotic electrical state of the ventricles which, if not immediately treated, will kill the patient. When the heart is in VF, it cannot pump blood through the body, depriving organs and tissues of the oxygen they require. Most organs can survive for some time without oxygen before sustaining permanent damage but the brain is highly sensitive to oxygen deprivation: permanent brain damage begins within four to eight minutes of anoxia. Severe or complete loss of brain function, defined as death, occurs after ten minutes. Sadly, these arrhythmias are not easily treated. Tachycardia can sometimes be terminated by Anti-Tachycardia Pacing (see section 1.3.2). In resistant cases, the only effective means of terminating VT—and the only proven means of defibrillating the heart when it is in VF—is to apply a strong global shock that excites the entire heart at once, essentially synchronizing it, so that it can return to its resting state.

1.2 Physics of the Heart

As was described above, the heart is a rich multiscale system which makes its study both interesting and challenging. The hierarchy of spatial and temporal scales is given in table 1.2. Each scale corresponds to a set of structures and dynamics that contribute to the organ's overall function. Molecular processes inside the cell and at its membrane

Table 1.2: Hierarchy of scales in the heart.

(a) Spatial scales.

Size	Structure	Dynamic
10^{-1} m	Diameter of the heart	Normal rhythm wavelength
10^{-2} m	Thickness of left ventricular wall	Fast arrhythmia wavelength
10^{-3} m	Electric length scale of cardiac tissue	Wavefront width
10^{-4} m	Length of cardiac cell	
10^{-5} m	Width of cardiac cell	
10^{-8} m	Thickness of cell membrane	
10^{-9} m	Pore diameter in a membrane protein	

(b) Temporal scales.

10^{9} s	Human lifetime
10^{6} s	Remodeling of the heart
10^{0} s	Period of heartbeat
10^{-1} s	AP duration of normal heartbeat
10^{-2} s	Period and AP duration of fast arrhythmia
10^{-3} s	Rise time of depolarization, membrane time constant

are organized to produce action potentials that propagate from cell to cell. This traveling action potential wave must propagate following a spatial and temporal pattern that ensures that the heart's contraction efficiently pumps blood through the body.

Dysfunction at any scale can throw off this carefully tuned machinery: mutations in ion channels lead to instabilities in action potential generation, variations in the shape and speed of the action potential modify the activation pattern and can lead to conduction failure; deviations from the normal pattern of activation can self-organize into sustained arrhythmias.

The heart is modeled as an excitable medium. The action potential is the fundamental excitation of the system and a resistive coupling between neighboring cardiomyocytes leads to wave propagation.

Excitable media are interesting because—in addition to the stable state—they support a variety of traveling wave solutions in spatially-extended systems: plane waves, target waves, spiral waves and defect-mediated turbulence (a.k.a. spiral breakup) [11,

12, 13, 14, 15, 16, 17]. Of the many patterns exhibited by excitable media, defect-mediated turbulence is of particular interest for the study of cardiac dynamics. This turbulent state is named for the spiral defects around which it is organized.

1.2.1 Mathematical models of cardiac dynamics

Cardiac tissue is modeled using a bidomain model [18, 19].

Models of cardiac dynamics take the general form

$$\nabla \cdot (\tilde{g}_i \cdot \nabla \Phi_i) - C_m \frac{\partial \Phi_i}{\partial t} = I_{ion}(V_m, \mathbf{y}) \tag{1.3a}$$

$$\nabla \cdot (\tilde{g}_e \cdot \nabla \Phi_e) - C_m \frac{\partial \Phi_e}{\partial t} = -I_{ion}(V_m, \mathbf{y}) \tag{1.3b}$$

where Φ_i and Φ_e are the intracellular and extracellular potentials, respectively, and $V_m = \Phi_i - \Phi_e$ is the membrane voltage. The membrane capacitance $C_m = 10^{-2}$ F/m^2 and $\tilde{g}_i$ and $\tilde{g}_e$ are the intracellular and extracellular conductances, respectively, in (S/m^2). Equations 1.3 together are referred to as the bidomain equations or bidomain model.

It will be useful to work with the membrane potential V_m rather than the intra- and extracellular potentials. In addition, we make the simplifying assumptions that the extracellular potential is everywhere at ground ($\Phi_e = 0$), which reduces the bidomain equations to a monodomain equation, and that the intracellular conductivity tensor is a homogeneous and isotropic scalar $\tilde{g}_i = g_i$. This reduces equations 1.3 to:

$$\frac{\partial V_m}{\partial t} = -\frac{I_{ion}(V_m, \mathbf{y})}{C_m} + D\nabla^2 V_m \tag{1.4a}$$

with

$$D = \frac{g_i}{C_m} \tag{1.4b}$$

The excitability and refractoriness of cardiac tissue is modeled by the nonlinear currents I_{ion}, which is where differences between models reside. Regardless of details, all models reproduce these basic properties: (1) an equilibrium state that is stable to small

perturbations in V_m, (2) an amplified response when perturbations to V_m exceed some "excitation threshold," and (3) a finite-time state of refractoriness after the system has been excited.

We will be interested in steady-state solutions to equation 1.4a near the equilibrium state ($V_m \approx V_{rest}$) under constant current conditions. The corresponding differential equation to be solved is

$$\nabla^2 e - \frac{e}{\lambda^2} = 0 \tag{1.5}$$

where $e = V_m - V_{rest}$ and $I_{ion} = \frac{V_m - V_{rest}}{r_m}$. This form of I_{ion} is an approximation where the membrane acts as a passive resistor, with constant resistance r_m and no non-linear currents ($\mathbf{y} = 1$). This is a good approximation for our purposes, since we will only be interested in finding the conditions under which e becomes positive enough to trigger an AP (i.e. reaches the excitation threshold) and not in its behaviour above the excitation threshold.

Equation 1.5 is a Helmholtz equation where, in the usual notation, $k^2 = \lambda^{-2}$. Solving this equation in spherical coordinates using separation of variables, as is commonly done, yields modified spherical Bessel functions.

1.2.2 Excitability

Waves in excitable media differ from waves in a classical medium (such as ocean waves or optical waves) in a few important respects:
(1) there is no superposition of waves—they annihilate upon collision,
(2) there is no dispersion of energy—the wave is regenerated by each cell it passes, and
(3) the cell has a refractory period—it must return to its "resting" state before it can be re-excited.

These properties form the basis of many fascinating natural phenomena in physics, chemistry and biology, such as the ability to form patterns in space and time. Examples

of pattern-forming systems include the Belousov-Zhabotinsky reaction, morphological development of embryos, chemotactic amoeba (Dictyostelium Discoideum). Although it does not obey excitable system dynamics, the complex Ginsburg-Landau equation is a well-studied model of pattern formation that reproduces many of the patterns seen in natural systems (including stripes, hexagonal arrays, dislocations, spirals and spiral defect chaos).

One of the most important corollaries to the properties listed above is that, once initiated, a wave can propagate indefinitely with no further external stimulus, so long as there are non-refractory (excitable) cells ahead of the wavefront. Evidently, any real-world system has a finite size. Thus a plane wave can, at best, last as long as it takes to propagate across the system. The next section introduces a wave configuration whose lifetime is in principle unbounded even inside a finite system.

1.2.3 Spiral waves

Let us imagine a wave propagating in a ring of tissue. Let the wave continue to propagate as the hole is made smaller and smaller until it disappears entirely. The moment the hole disappears, we have a circular piece of tissue with a wavefront pivoting around the center. This type of wave is called a spiral wave and it can propagate indefinitely.

The spiral shape of the wave follows from its (1) finite propagation velocity and (2) finite refractory period. Together, these lead to a curvature-dependent velocity [20]. A flat wavefront connected to the system boundary at one end only will propagate forward at finite velocity while the open end (the end not connected to a boundary) will develop curvature and enter a state of rigid rotation.

The point around which the wave rotates is a topological singularity, by virtue of the fact that all phases of the cardiac action potential meet there. It is most commonly referred to as the "core" or the "phase singularity." Far from the core of the spiral, the

wave pattern resembles the concentric rings of a perodic source, except that a closed path around the spiral's core, no matter how far away away, always encloses a unit of topological charge [21].

1.3 Controlling Chaos

In the phase space of excitable systems there are at least one and sometimes three fixed points, two of them stable (s.f.p.) and one unstable (u.f.p.). This creates three classes of systems: monostable excitable (1 s.f.p.), bistable excitable (2 s.f.p., 1 u.f.p.) and oscillatory systems (1 u.f.p.). Diffusive coupling sometimes destabilizes one of the stable fixed points, creating two classes: monostable systems and bistable excitable systems [22, 23]. The heart belongs to the class of monostable excitable systems.

A spatially-extended excitable system may have other attractors besides the stable fixed point(s), such as limit cycles and strange attractors. In models of the heart, these attractors correspond to self-sustained spiral waves whose centers may be stationary in space or follow a periodic or quasi-periodic orbit or a random trajectory, or the wave may spontaneously "break up" into multiple spiral waves [24]. The lifetime of the spiral wave state(s) depends on the system's size and on its dynamics and parameter values. For example, it is well known that a critical mass of heart tissue is required to sustain stable spiral waves [25].

Control theory searches for approaches to moving an excitable system from one attractor to another with the minimum possible intervention. The goal is usually to coax the system towards a (stable or unstable) fixed point or limit cycle and to keep it there. The diffusive coupling inherent in spatially extended excitable systems allows global control using a small, finite number of control points (the fewer the better).

Control requires knowledge of the system's state and its dynamics [26, 27]. Difficulties in controlling continuous excitable systems arise because, apart from the globally

"quiescent" state, self-sustained patterns in excitable systems are characterized by topological singularities that can only be removed by pair-wise annihilation (combining opposite polarities) or by causing them to move towards a boundary where they annihilate with their virtual partner.

1.3.1 Model-inspired approaches to chaos control

Modeling studies have suggested a number of approaches for converting spiral-defect chaos into a defect-free stable state. Some but not all of the approaches suggested by models are feasible in experimental settings. This is particularly true in the heart because of limited access.

Some approaches, based on detailed cell models grounded in molecular biology and cell electrophysiology, posit that spiral-forming instabilities in action potential wave propagation are due to altered membrane dynamics at the cellular level. These approaches advocate modifying the cellular membrane dynamics via drugs. Following this rationale, a number of drugs were developed that primarily modified the activity of sodium or potassium membrane channels. However many of these drugs proved to be either ineffective and even harmful in patients [28, 29, 30]. The drugs induced changes in the target ion channels that inadvertently created new vulnerabilities while suppressing known vulnerabilities. This highlights the complexity of the heart's dynamics and the challenges of controlling its electrical behaviour.

Prophylactic treatment against the onset or recurrence of a cardiac arrhythmia is not currently available for all symptomatic and at-risk patients. Moreover, healthy individuals can also suffer from acute cases of cardiac arrhythmia, usually as the result of trauma or injury. These cases require emergency medical intervention and are almost always treated with electrical defibrillation. Thus complementary anti-arrhythmic treatments that target the wave dynamics directly are still needed.

Krassowska and Neu [31] have investigated the response of a single heart cell in a uniform electric field. Sobie, Susil and Tung [32], Roth [33, 34, 35, 18], Sepuvelda *et al*. [36], Trayanov *et al*. [7] and Alonso *et al*. [37] have shown in numerical simulations that local gradients in parameters such as the excitability could be used to alter wave dynamics, but it is not clear how to modify these parameters in the heart, or even whether they can be modified.

The most direct approach is to apply an external current via a potential gradient. This is the approach employed by electrical defibrillation, whether from an external or an implanted device. The potential gradient affects both the intracellular and extracellular potentials, Φ_i and Φ_e. However, the state of the system is a function of the *difference* between the intra- and extracellular potentials, i.e. the membrane potential V_m. Thus the potential gradient must affect Φ_i and Φ_e *differently* if it is to have any effect on the state of the heart. Different anisotropy ratios of ionic conductivity in the intra- and extracellular spaces is one way to obtain changes in membrane potential. Another way is to introduce conductivity inhomogeneities in the intra- or extracellular space.[1]

1.3.2 Local overdrive pacing for spiral wave termination

Overdrive pacing is the principle behind the therapy known as anti-tachycardia pacing (ATP), so named because it has been shown to be effective in terminating tachycardia in patients [38]. Given two periodic wave sources with different frequencies in an excitable system, the faster source will eventually overtake and mute the slower source [39]. Let the two sources have periods T_1 and T_2, respectively, such that $T_1 > T_2$ (source 2 is thus the higher-frequency source). Each source emits waves that travel radially outward and collide somewhere between the sources. Each wave collision occurs closer to the slower

[1] One might argue that conductivity inhomogeneities in one space are not fundamentally different from unequal anisotropy ratios, but since distinct anatomical features give rise to each case, we find it useful to discuss them as two separate means of inducing changes in membrane potential.

source T_1 than the previous collision. Thus, the waves from T_2 will eventually reach the source of T_1. Depending on whether T_1 is an ectopic (automatic) source, such as the heart's natural pacemaker, or a reentrant spiral wave, one of two things will happen. A slow ectopic source will be suppressed but not permanently silenced; if the faster source ceases to emit waves, the automatic source will resume its slow periodic wave generation. A reentrant spiral wave, on the other hand, is not spatially bound and will be repelled by the more frequent oncoming waves. The (deliberate) use of a faster wave source to silence or repel a slower wave source in excitable media is called *overdrive pacing* [40].

ATP consists of 8–15 *localized* pulses generated by an implanted *point* electrode in direct contact with heart tissue, with a period ~10% shorter than the dominant period of the tachycardia. Unlike FATP is applied when the heart rhythm exceeds a preset threshold (typically around 200 beats per minute or roughly 3 Hz). Unfortunately, ATP's effectiveness decreases as the VT frequency increases. Sivagangabalan *et al*. measured the effectiveness of ATP in human patients with induced fast ventricular tachycardia (FVT; cycle length 251–320 ms) or very fast ventricular tachycardia (VFVT; cycle length 200–250 ms) during ICD implantation [41]. They found that FVT was successfully terminated by ATP in 62% of cases and accelerated in only 18% of cases. In contrast, VFVT was only terminated in 30% of cases and accelerated in 26% of cases. The success rate of ATP decreases with VT cycle length whereas the acceleration rate increases. Thus ATP is contra-indicated for arrhythmias faster than 5 Hz (300 bpm).

ATP succeeds when it causes phase singularities to drift into the tissue boundaries where they annihilate. The number of ATP pulses required to successfully annihilate a spiral wave can be estimated via the following equation:

$$N = \frac{L_1}{v_c \Delta T/2} + \frac{L_2}{v_c \Delta T} = \frac{2L_1 + L_2}{v_c \Delta T}. \tag{1.6}$$

L_1 is the distance between the pacing electrode and the spiral core, L_2 is the distance between the spiral core and the tissue boundary where it will be annihilated, and $\Delta T = T_s - T_p$ is the difference between the frequency of rotation of the spiral T_s and the frequency of the pacing electrode T_p. One would like to make ΔT as large as possible so as to minimize the number of pulses required, however there is a lower limit to the wave train period that can propagate in heart tissue. Inserting typical human heart values[2],

$$L_1 = 1\text{–}5 \text{ cm}, \qquad T_s = 0.2 \text{ s}, \qquad v_c = 50 \text{ cm/s},$$
$$L_2 = 5\text{–}10 \text{ cm}, \qquad T_p = 0.18 \text{ s}, \qquad \Delta T = 0.02 \text{ s},$$

equation Eq. 1.6 predicts between 7 and 20 pulses to successfully push the spiral core to a boundary. The number of ATP pulses used in patients (8 pulses at 88% of dominant cycle length) falls in this range [41].

The distance between the pacing electrode and the spiral core L_1 has twice the weight of the distance from spiral core to boundary L_2. Thus, judicious placement of the pacing electrode is critical if one wishes to minimize the number of pulses and/or maximize the pacing period T_p. Why would one wish to use larger pacing periods? Because shorter pacing periods are at greater risk of encountering conduction block, which effectively doubles the pacing period and makes the pacing useless.

The only natural non-excitable boundary in the heart is the base (where the ventricles meet the atria, equivalent to the "equator" of the heart). Therefore the pacing electrode used in ATP is usually implanted near the apex of the heart (the lowermost tip of the ventricles) so that it can drive the spiral wave to the base of the heart. The distance from apex to base in a normal human heart is on the order of 10 cm.

Experiments on live dogs with atrial fibrillation showed that local pacing with $T_p = 72 - 84$ ms can entrain tissue only up to 3 cm away [42]. The physical mechanism for this failure was investigated by Fox in a series of articles on dynamical mechanisms of conduction block (see references [43, 44, 45] and citations therein). These modeling

[2]The pacing period is usually chosen to be 90% of the spiral period: $T_p = 0.9 \cdot T_s$.

investigations found that, when the heart is beating faster than usual, the built-in adaptation mechanism[3] can cause propagating waves to collide with the wavebacks (the repolarizing phase of the AP) of preceding waves, blocking further propagation. Conduction block is thought to be one means by which a pair of counter-rotating spiral waves can be initiated: when block occurs along a portion of a wavefront, a pair of phase singularities is nucleated at either end of the block, setting the stage for reentrant spiral waves (provided the "line of block" is longer than the radius of rotation of the spiral cores).

More recently, Johnson *et al.* implemented a real-time feedback control algorithm based on single-electrode pacing [49]. They found that up 18 cm^2 of the pig ventricle could be captured during VF via pacing at 95% of the VF cycle length. However, "while it was possible to capture a fairly large region of the right ventricle in multiple pacing episodes, pacing never halted fibrillation."[49] This provides additional evidence that pacing from one electrode, as is done with ATP, cannot terminate VF.

While these experiments showed that ATP is not suitable for terminating arrhythmias faster than 5 Hz, they suggested a possible solution. If the distance from any portion of the fibrillating heart to a pacing electrode can be reduced to 3 cm or less, then it is possible that the entire tissue could be entrained by pacing. This would require multiple electrodes placed all over the heart. Each electrode would entrain a small region and all together the electrodes would entrain the whole heart, thus allowing it to return to its normal rhythm.

1.3.3 Far-field pacing

In contrast to ATP, where pulses are delivered locally from an electrode in contact with tissue, far-field pacing (AFP) consists of a sequence of electrical pulses from far-field

[3]Heart rate adaptation is expressed in the well-known action potential duration (APD) and conduction velocity (CV) restitution curves, which plot APD and CV against the preceding diastolic interval (DI). See Fox *et al*[46] or Koller *et al.* [47] or Gelzer *et al.* [48] for more details on APD and CV restitution and how these can lead to fibrillation.

electrodes (plates or grids). When a voltage difference is applied between the far-field electrodes, an electric field is generated that drives current through the heart, altering the membrane potentials as described above.

Defibrillation is a form of AFP where the sequence consists of only a single pulse. It is thought to operate at the level of individual cells, globally resetting all cells and essentially wiping out any existing reentrant wave activity. To successfully terminate fibrillation, a defibrillation shock requires a field strength of 4–6 V/cm, applied for 5–20 ms, during which a total energy of 100–360 J is deposited in the patient's chest (400–580 V, ~5–30 J when delivered via a catheter electrode placed inside the heart) [50]. Although these shocks do not appear to damage the heart[4], patients rate internal shocks with energies greater than 2 J as painful and greater than 3 J as intolerably painful [50]. Drug treatments are still far from being able to terminate arrhythmias in emergency settings. Thus, there is a clear need for new approaches to defibrillation that require pulse energies below 2 J.

Because we want to try low-energy AFP pulses, new mechanisms must come into play. Two possible mechanisms are described below: spiral wave unpinning and tissue synchronization.

Pinning and unpinning

Heterogeneities in the heart are an asset as far as induced wave emission and control are concerned, but they can also serve as pinning centers, adding to the difficulty of terminating fibrillation.

A far-field pulse depolarizes one side of an obstacle and where this depolarization exceeds the excitation threshold, an action potential is generated. Now if a spiral wave is rotating around the obstacle, most of the tissue around the obstacle is refractory save

[4]Walcott *et al*. reviewed the potential damage to the heart from defibrillation shocks and found that shock strengths used clinically are well below the threshold for damage [51].

for a small portion between the retreating waveback and the advancing wavefront. The unpinning mechanism requires that the depolarizing stimulus overlaps the waveback so as to generate a single wave(a single topological charge remains on the obstacle while its partner travels outward along the retreating waveback). The newly generated wave travels along the obstacle boundary in the opposite direction to the pinned spiral. When the two wavefronts meet on the boundary they annnihilate and the spiral has been unpinned. The width of the window in which unpinning is possible is called the "unpinning window" [52, 53].

Successful unpinning of a spiral wave via a single, phase-synchronized far-field pulse was demonstrated by Ripplinger *et al*. in isolated rabbit right ventricular tissue [54]. A single-pulse approach is suitable for unpinning a single spiral wave (characteristic of VT). It is not suitable in the presence of multiple pinned spiral waves because the spirals are generally not phase-synchronized.

In order to catch each spiral in its "unpinning window" (UW) [52, 53], a sequence of pulses can be applied at different phases. Li *et al*. showed that multiple pulses can indeed unpin a single spiral wave in post-myocardial infarction rabbit hearts [55]. The mechanism ought to be straightforward: if the UW is a quarter of the period T_{PS} of a pinned spiral, then a series of four pulses applied every quarter period ($T_{pacing} = T_{PS}/4$) should unpin the spiral. However, this result incorrectly assumes that pulses that do not fall in the UW have no effect on the spiral wave itself. A more detailed and systematic investigation of the unpinning mechanism of multiple far-field pulses is required; this is currently the subject of research by Anna Behrend (MPIDS, Göttingen, Germany).

Synchronization

Fenton *et al*. showed that a sequence of far-field pulses, properly timed, can terminate atrial arrhythmias (tachycardia, flutter and fibrillation) with only 13% of the pulse

energy required for standard defibrillation in in-vitro canine atrium preparations [56]. Together with this team, we have reproduced this result in live (anesthetized) dogs, using our LabView control algorithms to terminate induced atrial fibrillation (AF). We found that AFP reduced the pulse energy by 84% compared to standard defibrillation [57].

What pacing periods might work? To effect a transition from chaotic to periodic dynamic (VT/VF to normal rhythm), the external perturbations must coherently nudge the system in the right direction. Because of the chaotic dynamics, the perturbations cannot be spaced much further apart than the typical period when the system is chaotic. The dominant period of the arrhythmia (a.k.a. the strongest signal in the Fourier spectrum) is usually taken as a representative period. Thus, we are looking for a pacing period not much longer than the dominant period of the arrhythmia. For fast arrhythmias, this places an upper bound of 300 ms on the pacing period.

The lower bound on the pacing period is found in prior work by Sweeney *et al.*, who investigated the effectiveness of high frequency (100 Hz–20 kHz) rectangular, monophasic pulse trains with 5, 10 or 20 ms duration for terminating VF. They found no energy gain compared to a standard defibrillation pulse (single *continuous* rectangular pulse with same total duration) [58]. Thus, there is a window of pacing periods between normal physiological rates (300 ms) and 10 ms in which we should look for a possible reduction in pulse energy.

1.3.4 Real-time feedback control

Real-time feedback control is a very promising avenue for treating cardiac arrhythmias. Today's implantable cardioverter-defibrillators (ICD) use real-time monitoring algorithms to determine when a defibrillating shock is necessary. We want to extend the use of real-time control to far-field pacing.

To this end, we designed and implemented feedback algorithms on the basis of which the frequency of the arrhythmia could be measured and AFP applied accordingly. Our first efforts in this direction were to compute and display a real-time Fast Fourier Transform (FFT), manually identify a dominant frequency and then set the AFP period accordingly. This of course implies a delay on the order of 10 seconds between measuring the dominant frequency and applying the intervention. Although the FFT was computed on a 1-second time window, fluctuations in the dominant frequency forced the user to mentally average the FFT until a dominant frequency emerged. Evidently, this strategy did not work as well for arrhythmias without a clear dominant frequency or where the dominant frequency fluctuated rapidly. This first generation system, described in 2.3.1, was used for the AFP canine experiments reported in 5.1. The second generation system, described in 2.4.1, added several new features, including automated VF induction, dominant period measurement, AFP pulse sequence generation, synchronized camera and power amplifier triggering, and data-logging.

1.3.5 Thesis outline

This thesis is organized as follows. Chapter 2 presents the equipment and methods used in this work, including two optical mapping setups, two far-field pacing setups, and associated algorithms. Chapter 3 explains the theory of wave emission from heterogeneities and presents the activation model we developed. Chapter 4 presents measurements of far-field pulse activation dynamics and analyses using the activation model. Chapter 5 presents the results of in-vitro experiments on termination of arrhythmias using far-field pacing (AFP). Conclusions and future experiments are in chapter 6.

CHAPTER 2

METHODS

Two major techniques exist for probing the membrane potential of cardiac cells in tissue preparations. The first and oldest technique is to probe the heart with electrodes. These can be made very small and highly sensitive with the use of good amplifiers. However, they are not very convenient when mapping the whole heart surface and they suffer from a "blind time" when even moderate amplitude pulses are applied to the heart. The second technique consists of injecting the heart with a fast (¡1 ms response time) voltage-sensitive dye and using wide-field optics to image the electrical activity. This has the advantage of providing high resolution measurements across a large field of view. In the last 20 years, this has become the method of choice for experiments on large cardiac tissue preparations. In this chapter, we describe the particular experimental equipment and methods used in this thesis.

2.1 Voltage-sensitive dyes

Di-4-ANEPPS is made up of two lipid tails that give the dye an affinity for the cell membrane (a hydrophobic bilayer) and a charged head that contains the fluorescent and voltage-sensitive moeities [59, 60, 61]. Loew *et al.* reported that di-4-ANEPPS shows the largest fractional change (10% per 100 mV) of any of the styryl dyes they tested [61]. Di-4-ANEPPS's electrochromic response is a linear shift in the excitation and emission peaks for voltage changes not larger than ~100 mV. Using a short- or long-pass filter, the peak shift is resolved as a change in fluorescence intensity.

Fluhler *et al.* [60] were the first to characterize the fast potentiometric styryl dye di-4-ANEPPS using hemispherical lipid bilayers as the substrate. They found an 8% change in relative fluorescence at the emission spectrum crossover point (610 nm) per 100 mV change in membrane potential using 544 nm excitation light. A more detailed

investigation of its properties in four different preparations, lipid vesicles, red blood cells, squid giant axon and guinea pig heart, found that the dye shows a consistent sensitivity of 5–10% fractional change in fluorescence [61]. Its response time to changes in membrane potential was on the order of one millisecond. Di-4-ANEPPS's excitation and fluorescence spectra in lipid vesicles are shown in figure 2.1.

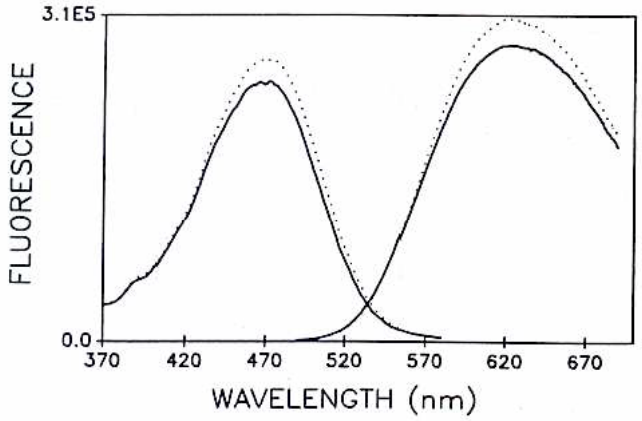

Figure 2.1: Excitation and emission fluorescence spectra of the voltage-sensitive dye di-4-ANEPPS. The spectra were obtained before (solid curves) and after (dotted curves) 120 mV hyperpolarization. Adapted from [61], with kind permission from Springer-Science+Business Media: The Journal of Membrane Biology, A Naphthyl Analog of the Aminostyryl Pyridinium Class of Potentiometric Membrane Dyes Shows Consistent Sensitivity in a Variety of Tissue, Cell, and Model Membrane Preparations, 130, 1992, p. 5, Loew *et al*., Fig. 3, and ©Springer-Verlag New York Inc. 1992.

2.2 Motion artifact removal

When the heart contracts, its image shifts in the frame of the camera, an effect called relative motion. In addition, changes in tissue density due to contraction can cause intensity variations that are not related to electrical activity. These motion-induced artifacts must be eliminated in order to resolve the optical action potentials: the changes in membrane-bound dye fluorescence caused by changes in the membrane potential.

The easiest way to do this is to prevent the heart's contraction altogether. Three main methods have been used in the past: immobilization of the heart against a hard transparent surface, perfusion with low-calcium Tyrode's solution ($[Ca^{+2}]$ = 62.5 μM instead of the normal 2 mM) or electromechanical uncoupling using blebbistatin, a selective myosin-II inhibitor [62], or 3,4-butanedione dioxime, also known as diacetyl monoxime or DAM.

Cell contraction is generated when myosin proteins bind thin actin filaments and move in a ratchet-like manner along the filament, pulling the ends of the cell towards each other. When the cell is at rest, however, another protein called tropomyosin covers the binding sites on the actin filament, preventing myosin from binding to the actin. Calcium released during the action potential binds to troponin, which allows the tropomyosin to move out of the way and unblock the binding sites for myosin. Lowering calcium concentration or blocking calcium channels prevents contraction by reducing peak intracellular calcium concentration. However calcium is intimately related to the electrical dynamics of cardiomyocytes [63].

We used a low-calcium Tyrode solution in the first 6 canine experiments ($[Ca^{2+}]$=62.5 μM instead of the normal 2.0 mM) or normal Tyrode containing DAM (10–40 μM). Blebbistatin was used for the last canine experiment (20 μM). In all rabbit heart experiments, we exclusively used blebbistatin (15 μM in 200 mL Tyrode, then recirculating normal Tyrode).

By targeting myosin, blebbistatin avoids the electrophysiological perturbations caused by DAM or low $[Ca^{+2}]_i$. Fedorov *et al.* [62] showed that applying 2–10 μM of blebbistatin to the Langendorf-perfused rabbit heart eliminated motion artifacts in optical maps without altering important electrophysiological properties such as action potential amplitude, action potential duration, and upstroke velocity (dV/dt_{max}), and without altering transient intracellular calcium activity.

2.3 Experimental Methods on Canines

2.3.1 Equipment

The experimental setup consisted of two systems: the imaging system, shown in figure 2.2, and the far-field pacing system, shown in figure 2.3.

Imaging system

The imaging system is similar in principle to those described in references [64, 65, 66, 67, 68]. In its most primitive form, it consists of a blue or green excitation light source, a red filter and a light sensor (such as a camera or a photodiode). The components of our optical mapping system are drawn schematically in figure 2.2 and are described below. Next to each description is the label used in the schematic figure.

Depending on the experiment, the cameras (2a & 2b) were either Photometrics Cascade 128+ EMCCD cameras (Roper Scientific, Inc.) or Phantom v7.1 high-resolution, high-speed cameras (Vision Research). The Cascade is a back-illuminated electron-multiplication charge-coupled device (EMCCD) with a 16-bit A/D converter and a quantum efficiency QE $\gtrsim$ 90 %. The Phantom uses a complementary metal oxide semiconductor (CMOS) sensor with a 12-bit A/D converter.

The resolution and speed of the Phantom (800 $\times$ 600 pixels, up to 8 kHz) easily surpass those of the Cascade (128 $\times$ 128 pixels, up to 511 Hz), but its lower light-sensitivity, smaller dynamic range (12-bit vs. 16-bit), and high data-rate[1] meant we could only use it for the far-field activation sequences, where high spatial and temporal resolution were critical and time between acquisitions was not a factor.

[1]The Phantom camera's high data acquisition rate translated into recording times of just a few seconds (5902 frames at 800$\times$600 pixels; 9100 frames at 640$\times$480 pixels) that took about 10 minutes to upload to the computer's hard drive. These time constraints made it unsuitable for experiments that required rapid turn-around times, such as the VF termination experiments.

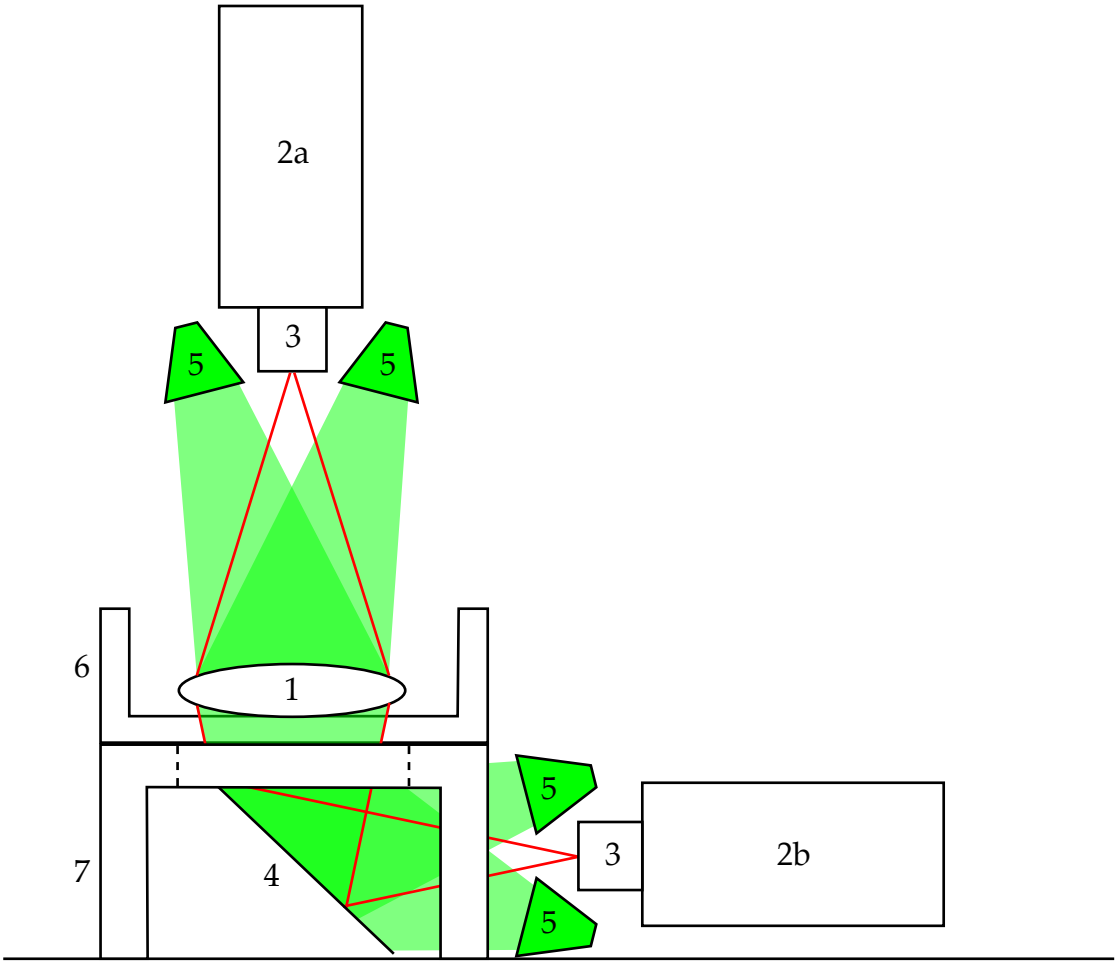

Figure 2.2: Schematic of the components that comprise the optical imaging system: (1) heart tissue preparation, (2) cameras, (3) lenses, (4) mirror, (5) LEDs, (6) tissue bath, (7) bath stand. Rays show approximate field of view of each camera. The optics and path length were the same for upper and lower cameras.

The Cascade cameras were operated using custom software written in C by Martin Ryan, an undergraduate research assistant, and the images stored in a custom-designed format (see Appendix). Typical runs acquired 5 to 30 thousand frames at 511 frames per second (fps) and 128 x 128 pixels. The system was capable of continuously acquiring data to disk.

The lenses (3) are C-mount, 50mm F/0.95 high-speed Navitar lenses[2] (Upstate Technical Equipment Co., Inc.) fitted with a threaded red filter (Hoya Red 25A). The red rays in figure 2.2 show the optical paths to each of the cameras.

A 10 cm hole was cut into the center of the bath stand (7) and a mirror (4), placed below the transparent perfusion bath (6) and angled at 45°, reflected the bottom surface of the tissue by 90° so that it could be imaged by the camera mounted on the table (2b).

A stable light source is important for cardiac optical imaging; fluctuations in illumination intensity can mask the sought-after signal. We first tested a 200 mW 532 nm battery-powered laser but the intrinsic noise was greater than the 2–3% fractional change in fluorescence intensity we measured from cellular action potentials. Therefore we elected to use high-intensity light-emitting diodes (Luxeon V Star, Conrad Electronics) powered by a stable DC power supply. We arranged a ring of LEDs around each optical path above and below the tissue preparation (5). The ring axes were centered on the optical paths of the cameras. Each ring contained five green (530 nm) and five cyan (505 nm) LEDs. Each LED drew 350 mA when running at maximum intensity.

Far-field pacing system

The far-field system is similar in principle to those described in references [69, 56]. It consists of a pair of far-field electrodes (grids or plates), a current source and control electronics. In our system, shown schematically in figure 2.3, we used a pair of 5×15 cm^2 stainless steel grid electrodes (2) with 1 cm spacing, 1 mm diameter wire,

[2] F/0.95 corresponds to a numerical aperture of $NA = 1/(2 \cdot F/\#) = 1/(2 \cdot 0.95) = 0.53$.

placed on either side of a rectangular perfusion bath (1) constructed out of plexiglass. The current source (3) was a bipolar power amplifier (BOP 100-4M, Kepco Electronics Inc.) with an analog ±10 V input and maximum 10× gain, giving a maximum output of ±100 V and ±4 A. The control system consisted of a function generator (4: 33220A 20 MHz Function/Arbitrary Waveform Generator, Agilent Technologies) controlled via a USB connection by a custom-designed LabView program running on a PC (6). A custom-built voltage doubler (4) was required because when using our LabView control software, the output of the function generator (4) was limited to ±5 V and we needed ±10 V as input to the Kepco in order to get its full output capacity. The field strength between the electrodes was measured using an oscilloscope (TDS 2024, Tektronix) connected to two silver wires[3] immersed in the bath and set about 1 cm apart.

2.3.2 Tissue preparation

We used standard methods for excising the heart, cannulating the coronary artery and perfusing it with Tyrode's solution [70]. For completeness, we give the details of our setup below.

The dogs were euthanized via injection of *Fatal-Plus* (Vortech Pharmaceuticals Ltd.), a humane euthanasia solution with sodium pentobarbital as the active ingredient. As soon as the animal was pronounced totally unconscious (showed no reflexes), the heart was excised via an incision along the 5^{th} intercostal space. The heart was immediately placed in cooled Tyrode solution for transport to the optical imaging laboratory. "The circumflex coronary artery or a branch of the right coronary artery was cannulated using polyethylene tubing. To avoid cutting the coronary vessels and creating vents for the perfusate, Tyrode solution was infused into the coronary artery, and the approximate area of perfusion was identified by blanching of the epicardial surface. A transmural

[3]The wires were Teflon-coated save for a 1 mm exposed section at the tip.

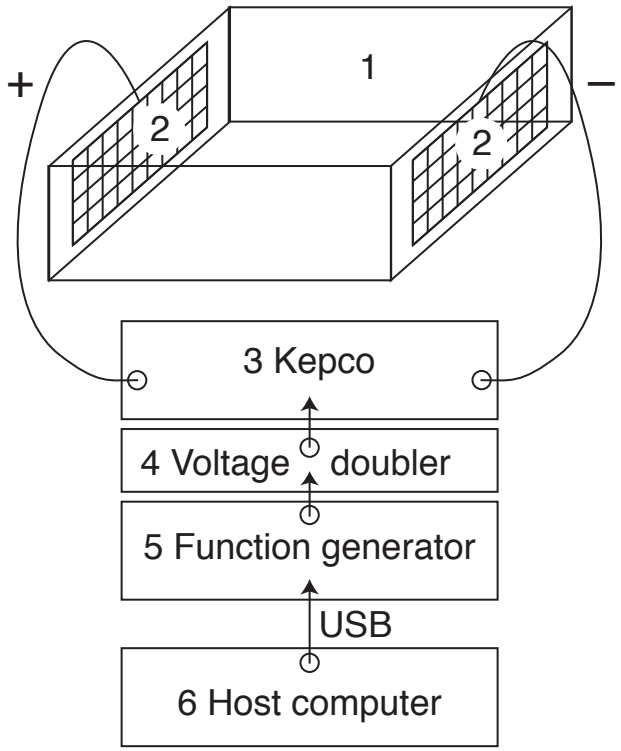

Figure 2.3: Schematic of the components that comprise the far-field pacing system: (1) tissue bath, (2) far-field electrodes, (3) power amplifier, (4) voltage doubler, (5) function generator, (6) host computer.

section of tissue 3 to 5 mm larger than the perfused area was then excised." [70] The tissue sample was approximately 8–10 cm across, with a thickness of 0.5–1 cm.

The perfusate was normal Tyrode solution bubbled with carbogen (95% O_2, 5% CO_2), delivered at a rate of 20 mL/min via a peristaltic pump (Harvard Appartus) and warmed to 37°C (see table 2.1 for the Tyrode recipe) as it flowed through a double-walled heated bubble trap. The tissue bath was filled with 37°C Tyrode solution. When placed in the bath between the field electrodes, the cannulated tissue preparation was submerged in 3–4 cm of Tyrode solution pumped through at a rate of 60 mL/min (this is called "superfusion" in the cardiological literature). A plexiglass plate was lowered onto the fluid surface (not touching the tissue) to prevent optical artifacts caused by surface waves.

Table 2.1: Tyrode recipe used in canine experiments.

Ingredient	Concentration (mM)
$MgCl_2$	0.5
NaH_2PO_4	0.9
$CaCl_2$	2.0
NaCl	137.0
$NaHCO_3$	24.0
KCl	4.0
Glucose	5.5

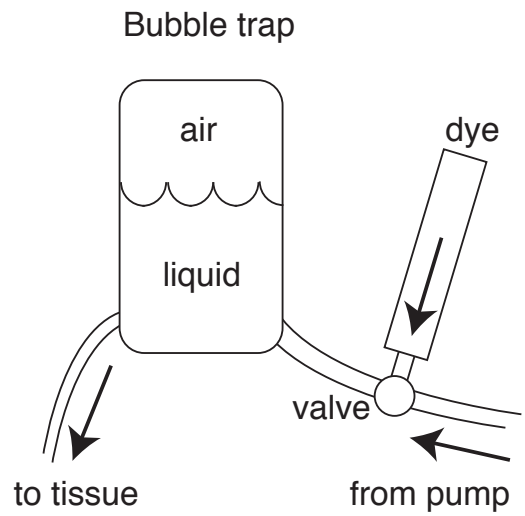

Figure 2.4: Sketch of bubble trap and perfusion line, with dye injection valve shown. The bubble trap is double-walled with distilled water at 37°Ccirculating through the inter-wall space to ensure that perfusate is at the proper temperature before entering the tissue.

The voltage-sensitive dye di-4-ANEPPS (Molecular Probes) was dissolved in Tyrode solution to a concentration of 10–20 μM and 10 mL of this solution were injected into the perfusion line behind the bubble trap, as shown in figure 2.4, both to warm the dye solution (which was kept at room temperature) and to prevent any bubbles from entering the tissue.[4] After waiting about five minutes for the dye to fully stain the tissue, the

[4]Air bubbles in the perfusion line that enter the heart via the coronary arteries act as plugs in the vessels that prevent perfusate from reaching downstream tissue. It is therefore imperative to monitor the status of the bubble trap to ensure it always contains fluid.

LEDs were turned on and the heart surface viewed through orange laser safety goggles.[5] The positions and angles of the LEDs were adjusted so as to maximize the light intensity incident on the region of interest. Using a power meter, we tried to achieve uniform illumination intensity over the field of view. During the experiments, the fluorescence intensity was continuously monitored for slow degradation due to photobleaching, internalization and washout. When the signal-to-noise ratio dropped to less than five[6], another 10 mL bolus of dye was administered.

The samples usually beat spontaneously at a rate of about 1 Hz. Nevertheless, we would pace the tissue with 2.5–3 mA, ~10 ms stimuli at cycle lengths of 300–500 ms from a stimulator and stimulus isolator (World Precision Instruments) via two silver-wire electrodes placed near the periphery of the tissue, so as not to obstruct the field of view. Every sample responded to the pacing stimuli.

Under these conditions, the tissue remains excitable for 6–8 hours. Once the heart is excised, it will inevitably die die and the perfusion setup only delays this process. Once the tissue had been prepared as described above, the cameras were brought online and the field of view and lens focus were adjusted. The Cascade acquisition parameters were set to gain index = 2, on-chip electron multiplication = 0, bin size = 1.

2.3.3 Protocols

Far-field activation maps

Quiescent (resting) tissue was stimulated with a sequence of far-field pulses at 500 ms intervals. Each pulse was 5 ms duration, rectangular and monophasic. The field strength sequences that were applied to each tissue preparation are given in table 2.2. The result-

[5]The safety goggles acted like red filters. Wearing them allowed us to see the regions of the sample that had taken up the dye. With good staining and illumination, it was possible to see the waves of electrical activity.

[6]The signal-to-noise ratio was defined as the amplitude of the optical action potential relative to the peak-to-peak noise amplitude during diastole.

ing epicardial and endocardial tissue activations were recorded at high resolution with Phantom cameras recording at 1000 frames per second (800×600 pixels).

Table 2.2: Pulse intervals were 500 ms except for the sequences marked with a (*) where they were 100 ms.

Date	Sequence No.	Field strength sequence (V/cm)									
2007-12-12	1	.07	.07	.21	.21	.34	.34	.47	.47	.60	.60
	2	.94	.94	1.3	1.3	1.9	1.9				
2007-12-11	1	.07	.07	.21	.21	.34	.34	.47	.47	.60	.60
	2	.07	.07	.21	.21	.34	.34	.47	.47	.60	.60
	3	.60	.60	.94	.94	1.3	1.3	1.9	1.9		
2007-12-10	1	.14	.14	.34	.34	.54	.54	.74	.74	.94	.94
	2	1.1	1.1	1.3	1.3	1.5	1.5	1.7	1.7	1.9	1.9
2007-12-07	1	.14	.34	.54	.74	.94	1.1	1.3	1.5	1.7	1.9
	2	.01	.07	.14	.21	.27					
2007-12-06	1	.14	.34	.54	.74	.94	1.1	1.3	1.5	1.7	1.9
2007-12-05	1	.14	.34	.54	.74	.94	1.1	1.3	1.5	1.7	1.9
2007-12-03	1	.01	.60	.27	1.3	.07	.14	.21	.34	.27	.94
2007-11-29	1	.07	.21	.34	.47	.60	.74	.87	1.0	1.1	1.3
	2*	1.3	1.3	1.3	1.3	1.3	1.3	1.3	1.3		
	3*	1.3	1.3	1.3	1.3	1.3	1.3	1.3	1.3		

The optical maps were spatially filtered with a 5-pixel boxcar kernel and temporally filtered with a 3-pt moving average kernel. The time series of each pixel was normalized to the range [0–1] and binarized with a 0.5 threshold. The activation time of each pixel was the time at which this binarized optical signal switched from 0 to 1.

Termination of VF

After inducing VF, we waited at least 10 seconds to rule out spontaneous termination and then we applied the following protocol. Far-field pacing (AFP) consisted of a series of 5, 8 or 10 identical monophasic rectangular pulses, of 5 ms duration. For each episode of induced VF, we would determine the threshold for successful termination via AFP by administering AFP with increasing voltage until VF was terminated. If we

reached 4 V/cm and VF had not been terminated, we would switch to single pulses (standard defibrillation) and increase the pulse strength until VF was terminated (up to the maximum field strength 6.6 V/cm). If the 6.6 V/cm limit (which was the limit of the Kepco power amplifier) was reached and VF still could not be terminated, then as a last resort we would turn off the perfusion pump until VF self-terminated from ischemia, then re-initiate perfusion.

2.4 Experimental Methods on Rabbits

2.4.1 Equipment

To carry out the whole heart experiments, we had to design and build a dedicated system with the following features: high-speed multiple data source acquisition, on-line analysis, on-line preview, automated pulse sequence generation, and camera synchronization. These features were implemented using the following components mounted in a 19" rack. A photograph of the setup is shown in figure 2.5.

1. Data Acquisition and Data Processing

   (a) (2x) PC computers running Windows XP

   - Intel Core 2 Quad 2.66 GHz (Q8400)
   - 8 GB RAM (Kingston PC800 DDR2)
   - (1x) high-speed hard drive (Seagate SAT500 BARRACUDA, 500 GB, 7200 rpm, S-ATA 2 connector, 16 MB Cache)
   - (5x) PCI 32 bit / 33 MHz slot

   (b) (1x) BIOPAC data acquisition and pacing system

   - (1x) 16-channel UIM100 recording module

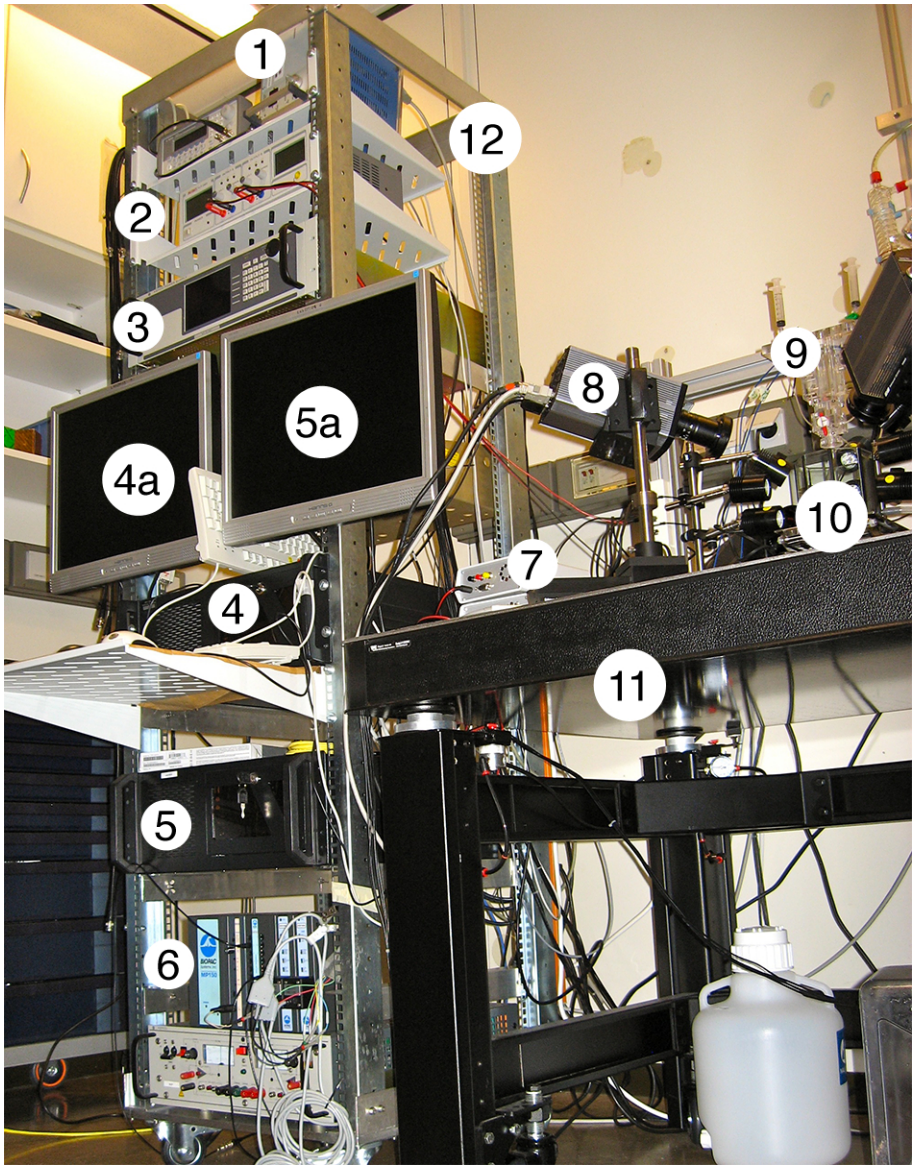

Figure 2.5: Photograph of the rack-mounted components that comprise the far-field pacing and optical imaging system: (1) custom-built temperature regulator, (2) VoltCraft DC power supply, (3) Luke 1 kW power amplifier, (4) electronics control computer and (4a) monitor, (5) camera control computer and (5a) monitor, (6) BIOPAC acquisition and stimulation system, (7) LED power supplies, (8) Cascade camera on 4-axis mount, (9) perfusion block, (10) jack-mounted perfusion bath, (11) optical table and (12) 19-inch rack.

Figure 2.6: Photograph of the BIOPAC MP150 acquisition with optional modules. From left to right: MP150 base module, STM100C stimulation module, UIM100C 16-channel universal input module, and two ECG100C electrocardiogram amplifier modules with MEC110C electrode coupling cables.

- (2x) ECG100C recording module
- (1x) STM100C stimulation module

(c) (2x) quadrupole monophasic action potential (MAP) electrode, for simultaneous sensing and pacing, with integrated guide-wire

(d) (1x) NIDAQ 6259 BNC (National Instruments)

(e) (1x) "Luke", a 1 kW bipolar power supply (max 100 V and 10 A; "High Power BOP 100-10MG", Kepco Inc.)

(f) (2x) stainless steel plate electrode (5×5 cm^2) in plastic mount (Hugo Sachs)

(g) (2x) silver wire electrode for E-field calibration

2. Illumination

   (a) (12x) 5W LED (532 nm, Conrad Electronics)

   (b) (2x) stable DC power supply

      - (1x) custom power supply
      - (1x) VoltCraft power supply (2x 10V/4A outputs)

   (c) (4x) LED power distribution unit (can power up to 4 LEDs in parallel)

3. Imaging

   (a) (2x) Cascade 128+ EMCCD cameras on rail-mounted rotating bracket mount (2 linear and 2 rotational degrees of freedom)

      - (1x) 17mm f/0.95 lens
      - (1x) 25mm f/0.95 lens

   (b) (2x) red filters

4. Perfusion and heating

   (a) (1x) Hugo-Sachs 5M retrograde Langendorf perfusion system

   (b) (1x) custom-made perfusion bath with heating foil glued to base

   (c) (1x) custom temperature regulator connected to a heating foil fixed to the bottom of the perfusion bath and water-proof temperature probe

Perfusion system

We adapted a Hugo-Sachs Isolated Heart Size 5 (IH-5) system by separating its components and mounting them on a custom frame. The heated perfusion bath was a custom-built octagonal container with a resistive heating foil glued beneath the floor.

The schematic drawing is given in figure 2.7. The size was chosen such that the electrical resistance through the Tyrode bath between the 5×5 cm^2 field electrodes, when placed on opposite walls, would allow the output current and voltage from Luke (the nickname given to the 1 kW power amplifier, item 1e on page 42 above) to be maximized simultaneously.

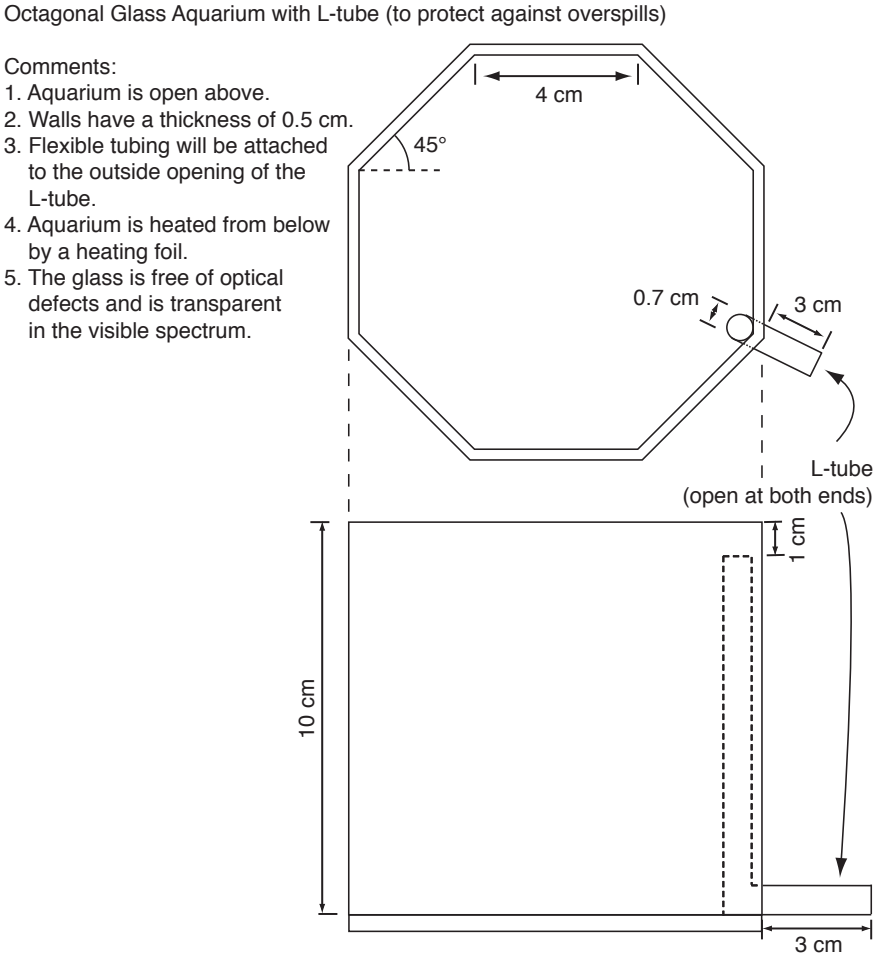

Figure 2.7: Heated bath design.

Imaging system

The imaging setup for the whole heart experiments is similar to the setup used for the canine ventricle experiments, described in section 2.3.1, therefore we will only highlight

the major changes between the two systems. Component descriptions will refer to the labels given in figure 2.8.

The system, shown in figure 2.8, was designed to allow for panoramic optical mapping of a whole heart, similar to the systems described in references [71, 72, 73]. Our system allows up to four cameras to be mounted around the heart, each on a 4-axis mount (two linear axes and two rotational axes). We used two cameras to image the left and right ventricles. The cameras (1 and 2) were fitted with a 17-mm f/0.95 (on 1) and a 25-mm f/0.95 lens (on 2). Brass spacer rings (1–2 mm wide) were inserted between the camera and the lens to increase the back focal distance and reduce the working distance to about 15 cm. A shorter working distance allowed us to use a smaller field of view without sacrificing focus, increasing our spatial resolution of the heart (3) at the cost of a shallower depth of focus. Four sets of three 5-Watt 532 nm LEDs (4) in custom holders with built-in focusing lenses, heat sinks and power cables were arranged around the heart to fully illuminate it.

Camera software

Simultaneous and synchronized high-speed recording from multiple Cascade cameras required custom software. Johannes Schröder-Schetelig, a master's student, wrote the *MultiRec* software, a C++ program that can control and record from multiple Cascade cameras. A screenshot of the excellent user interface he designed is shown in figure 2.9. The *MultiRec* software includes a live preview mode and detailed control over the camera's settings. During simultaneous acquisition, data from all cameras is streamed to disk in a single file to reduce overhead and prevent bottlenecks in writing to disk. This allowed us to routinely record up to 3 minutes of full-frame (128×128 pixels), continuous optical mapping data from two Cascades at 500 frames per second.

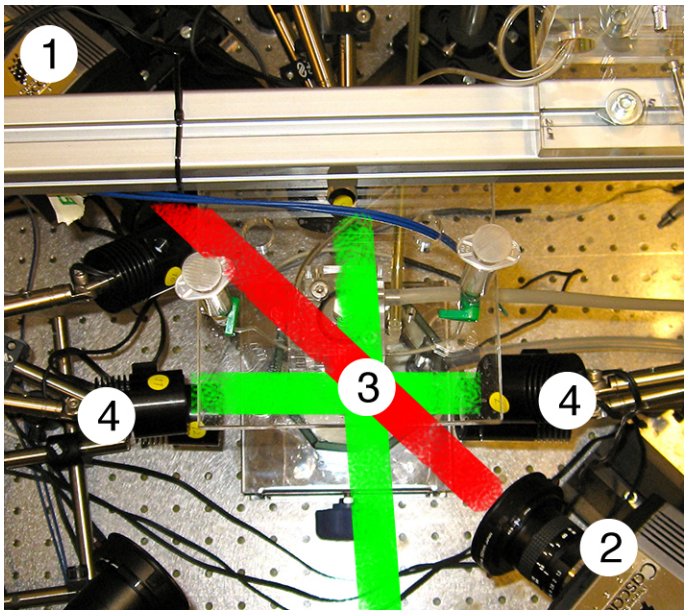

Figure 2.8: **Whole heart imaging setup.** Photograph of the experimental setup, showing the principal components: (1) Cascade camera #1, (2) Cascade camera #2, (3) tissue preparation in its perfusion bath, (4)high-power 532 nm LEDs. Green rays show excitation light paths and red rays show fluorescent light paths.

BIOPAC AcqKnowledge software package setup

We set up the BIOPAC AcqKnowledge software to record 4 channels at 2 kHz: one channel for each monophasic action potential (MAP) electrode signal, one channel for the current output of Luke, and one channel for the camera trigger signals. Calculated channels monitored the activation rate from each MAP electrode. The setup is shown in figure 2.10.

LabView programs

To control and synchronize the various components of our experimental setup, we designed and programmed a set of custom LabView programs to perform the following functions:

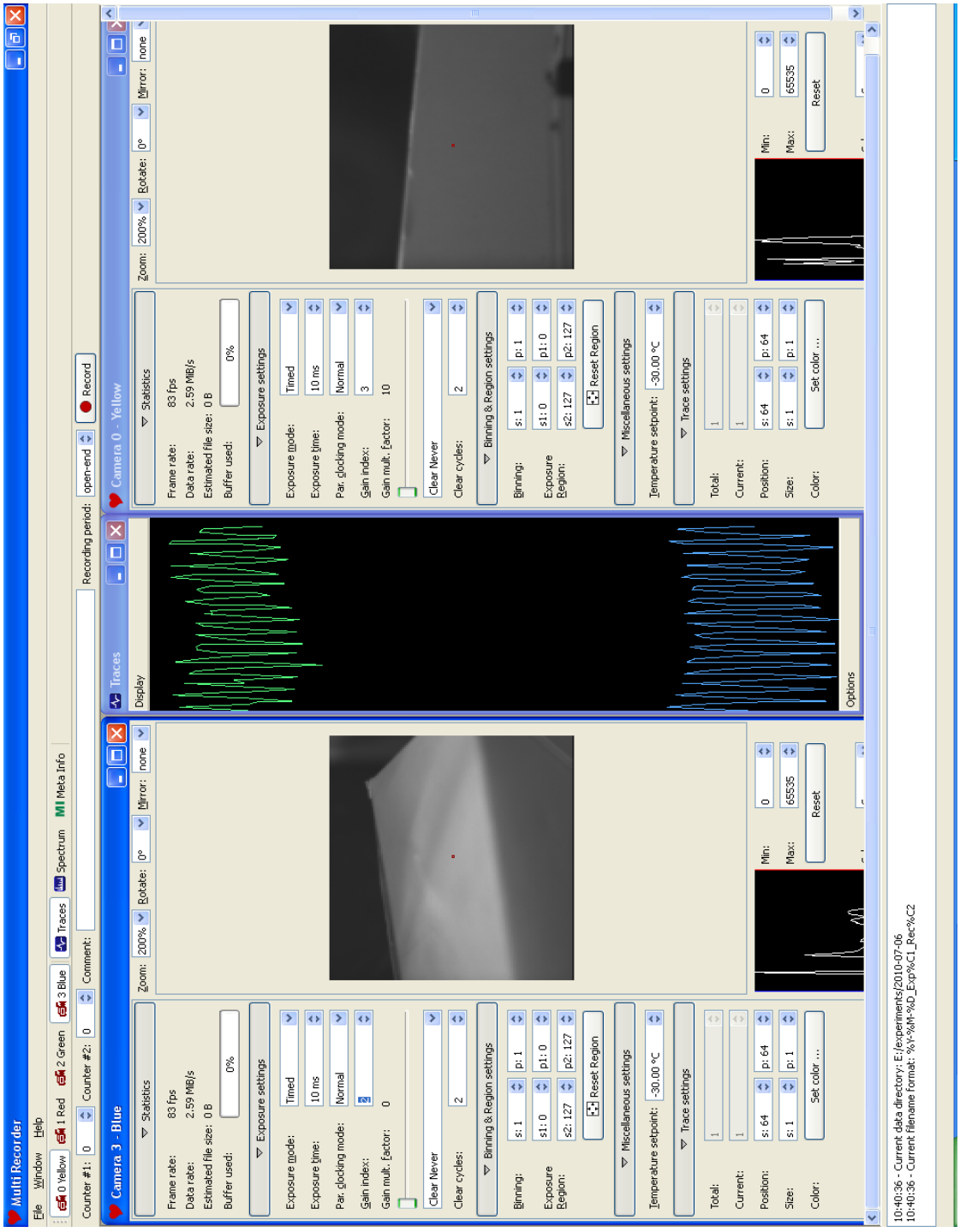

Figure 2.9: MultiRec camera software user interface.

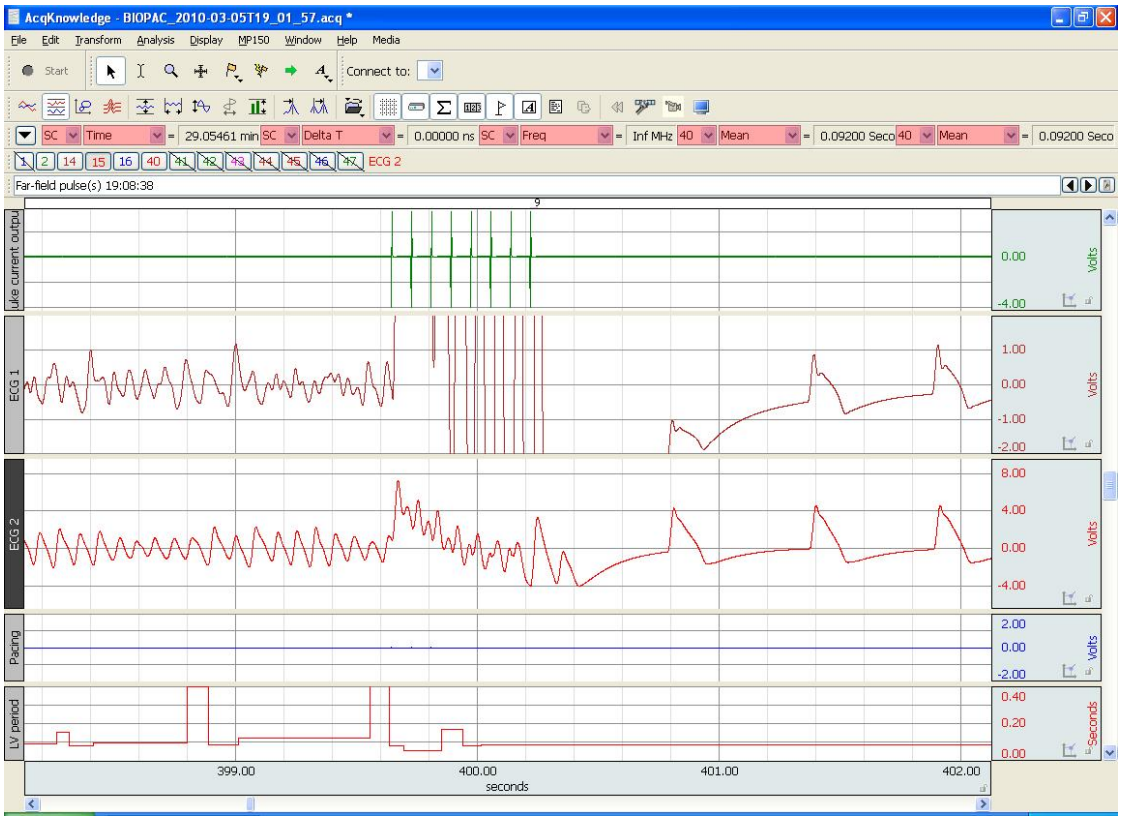

Figure 2.10: **AcqKnowledge software setup.** Example of AFP termination of ventricular fibrillation. From top to bottom: Luke current output (green) showing 8 pulses; monophasic action potential (MAP) signals (red, labeled ECG1 and ECG2) showing transition from VF to normal rhythm; pacing signal (blue) which is null after VF was induced; and calculated heart rate (red) based on ECG1 signal.

1. apply a sequence of far-field pulses for activation map measurements
2. induce VF via pace-down
3. measure dominant frequency in real-time
4. apply AFP with user-determined or automated frequency selection and user-defined parameters:
    - voltage
    - shape (monophasic vs. biphasic)

- polarity
- pulse duration
- number of pulses

5. apply defibrillation
6. synchronize cameras with external field pulses
7. automatically calibrate electric field

These LabView programs were run on a PC connected to the DAQ, a high-speed data-acquisition-and-digital/analog-signal-generation unit.

Contact monophasic action potential (MAP) signals [74] were acquired via the BIOPAC amplifier and acquisition unit and output to the DAQ for real-time analysis. LabView would read these data input streams in real-time, analyze the dominant frequency in a three-second window, generate a far-field pulse sequence (with the specified period ratio and field strength) and corresponding camera trigger sequence, then instruct the DAQ to simultaneously and synchronously output the pulse sequence to Luke and the camera trigger sequence to the cameras. This tight synchronization of the field pulses and camera triggers was necessary in order to accurately measure the activation time following each pulse.

This second generation system also incorporated an automated and more accurate period detection algorithm for faster and more accurate control. LabView's built-in frequency detection "virtual instrument"[7] (VI) takes a frequency range (set to 1–30 Hz) as a parameter and searches for a dominant frequency within this range. Based on real-time input from one of the BIOPAC ECG acquisition modules[8] (relayed through the

[7]Virtual Instruments or VIs are programs or subroutines in LabView.

[8]The input signal to the LabView VI could come from any source that outputs a voltage with amplitude not exceeding 10 V. The signal itself could be, for example, an MAP signal, an ECG signal or an optical mapping signal.

DAQ), the VI gave a scalar quantity as output: the dominant frequency. The automatically detected frequency was inverted to give a period $T_{dominant}$ which was then fed into our custom AFP sequence generation VI. Our sequence generation VI calculated the AFP period T_{AFP} as the product of the dominant period it received as input and a user-specified period ratio χ of order 1: $T_{AFP} = \chi \cdot T_{dominant}$. The AFP sequence and accompanying camera trigger sequence were then output from separate channels on the DAQ to Luke and to the Cascade cameras, respectively.

The entire operation began the moment the user clicked "Go" in the wrapper program. The LabView program would take a few seconds to measure the dominant period then immediately applied the AFP sequence. This second generation system reduced the measurement and control delay and increased the accuracy of the frequency measurement.

2.4.2 Tissue preparation

The hearts of New Zealand White rabbits (female, 2.5–4 kg) were excised under general anesthesia (Thiopental) after injecting Heparin (1000 I.U.) to prevent blood clot formation. After removing excess tissue (fat and lung tissue), the aorta was isolated and cannulated on a Langendorf perfusion system, shown in figure 2.11. Tyrode's solution (see table 2.3), pre-warmed to 37°C, was recirculated through the heart at a rate of 30 ml/min. The outflow of the bath was passed through a fine filter before being recirculated. The aortic pressure was set to 80 mmHg. These parameters ensured that the heart was maintained near its normal physiological condition.

Inducing sustained fibrillation

It has already been shown that sustained fibrillation requires a critical mass of susceptible substrate tissue [25]. Smaller mammal hearts, such as those of rabbits, guinea pigs,

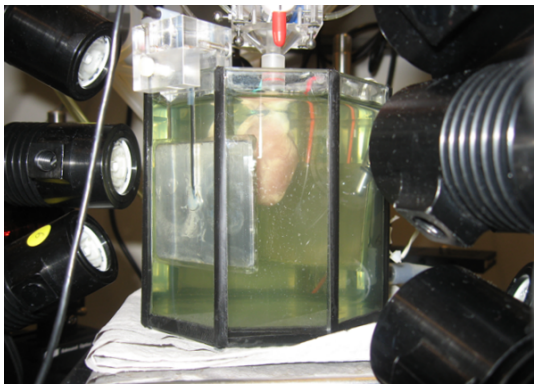

Figure 2.11: Heated perfusion bath containing cannulated heart. One of the field electrodes is visible in the foreground of the bath.

Table 2.3: Tyrode recipe used in rabbit experiments.

Ingredient	Weight (g) required per liter of Tyrode	Final concentration (mM)
NaCl	6.72	115
KCl	0.3504	4.7
$MgCl_2(6H_2O)$	0.142	0.7
$CaCl_2$	0.22	2
$NaH_2PO_4(H_2O)$	0.06	0.5
$NaHCO_{a3}$	2.35	28
Glucose	3.6	20
Albumin	0.04	0.02
Adenosine	0.04	0.02

mice and rats, are often used in cardiological studies but must be modified in some way in order to induce sustained fibrillation. Ischemia, the restriction of perfusate flow, is a widely-used model for make the cardiac tissue susceptible to fibrillation in rabbit hearts. It is easy to apply in the in-vitro setting: the perfusion pump speed is simply lowered.

We used a protocol of 5–7 minutes low perfusion (3 ml/min) followed by 3 minutes reperfusion (30 ml/min). The aortic pressure was kept at 80 mmHg throughout. During the 2-3 minutes following the ischemia-to-reperfusion transition, we used a rapid pace-down protocol to actually induce fibrillation. This consisted of a series of 25 bipo-

lar current pulses (100–150 mA) delivered with decreasing cycle lengths, from 250 to 100 ms. The pacing protocol was interrupted as soon as fibrillation was induced. Pacing pulses were delivered through the stimulating channels of one of the quadrupolar MAP electrodes placed inside the left or right ventricle, near the apex of the heart.

Microscopic Computerized Tomography Imaging

We used a GE Healthcare microCT scanner with a resolution of 40 microns to obtain whole scans of the rabbit hearts. Computerized tomography uses a series of X-ray projections to reconstruct tissue structure. Because of the low contrast of soft tissues, we injected a liquid contrast agent containing barium sulfate into the coronary arteries at the end of every experiment. After thresholding the data, we obtain images like those shown in 1.4 on page 7.

2.4.3 Protocols

Far-field activation maps

We recorded the electrical responses of the quiescent tissue to external electric field pulses in the Langendorf rabbit preparations. Each pulse was rectangular, symmetric biphasic, with total duration 4 ms (2 ms up and 2 ms down). The protocol consisted of an unbroken pulse sequence, 10 at each field strength, with a fixed interval T =350–500 ms between pulses. Thus the total activation sequence protocol took $36 \cdot 10 \cdot T$ =126–180 seconds. The sequence of field strengths was as follows: 0.1 to 3 V/cm in steps of 0.1 V/cm and from 3 to 6 V/cm in steps of 0.5 V/cm, for a total of 36 distinct field strengths.

The optical maps were spatially filtered with a 5-pixel boxcar kernel and temporally filtered with a 3-pt moving average kernel. The time series of each pixel was normalized to $[0, 1]$. The activation time $T_{x,y}$ of each pixel (x, y) was the first time after the pulse at

which the 4-frame (8 ms) difference was a minimum:

$$T_{x,y} = \text{argmin}_{t \in \mathbb{N}_0} \left(v_{x,y}(t + 8 \text{ ms}) - v_{x,y}(t) \right) \tag{2.1}$$

where $v_{x,y}(t)$ is the optical signal from a pixel at (x, y).

Termination of VF

After inducing VF, we waited at least 30 seconds to rule out spontaneous termination. Far-field pacing (AFP) consisted of a sequence of 8 identical 4 ms symmetric biphasic pulses (2 ms up and 2 ms down). The standard defibrillation was a single pulse with the same parameters as the AFP pulses. Biphasic shocks prevented chemical layer build-up on the electrodes by running the same voltage forwards and backwards for equal time in quick succession. These chemical layers passivate the electrodes, increasing their electrical resistance and reducing the field strength seen by the heart.

For each episode of induced VF, we determined the threshold for successful termination via AFP by administering AFP sequences 3 times at one field amplitude, then incrementing the amplitude by 0.65 or 1.3 V/cm. If the 7 V/cm limit was reached, we switched to standard defibrillation pulses and increased the pulse strength up to 13 V/cm or until VF was terminated. The 13 V/cm limit (the limit of Luke's output voltage) was only reached once. In that case, we turned off the perfusion pump to create acute global ischemia until VF self-terminated, then we re-initiated perfusion.

Electric field calibration

The electric field was calibrated after the experiments, once the heart had been removed from the bath but while the bath was still filled with Tyrode solution. Two silver wire electrodes were placed 1 cm apart in the bath (a special plexiglass holder was built to ensure correct separation). A sequence of 4 ms biphasic pulses (identical to the ones used

for AFP and defibrillation) with amplitude 1–20 V was applied and the resulting potential difference at the electrodes was recorded by the DAQ. We extracted the calibration parameters by fitting a first order polynomial to the recorded potential differences as a function of the applied voltages.

CHAPTER 3

ACTIVATION MODEL OF CARDIAC TISSUE

One of the great challenges in cardiac electrophysiology has been to understand the mechanism of defibrillation [75]. Although this still remains an open question, significant advances have been made in understanding the effects of passing an external current through cardiac tissue. The primary effect we are interested in is cell membrane polarization. Using the bidomain model, two mechanisms of polarization have so far been identified: one due to unequal anisotropy ratios in the intra- and extracellular spaces, and another due to changes in conductivity. The first mechanism requires only that the conductivity tensor be anisotropic while the second mechanism requires only that it be inhomogeneous. We will briefly review these two mechanisms, then focus on the second as the basis for our model of tissue activation and for our experimental results.

A great number of theoretical and experimental investigations into the effects of an electric current focused on explaining standard defibrillation. Researchers identified mechanisms by which currents induce changes in V_m [1, 2, 76, 56, 77, 78]. Some of these results are summarized in a review by Roth and Krassowska [34]. Initial investigations focused on virtual electrodes induced by current redistribution due to fiber orientation. In the bidomain model, differences in intra- and extracellular anisotropy ratios create virtual electrodes when current is passed through the system. According to Wikswo, "point injection of either anodal or cathodal current into resting cardiac tissue produces simultaneously virtual cathodes and anodes that are the result of differences in the anisotropy of the electrical conductivity of the intracellular and extracellular spaces of the cardiac syncytium." [65]

The role of larger tissue inhomogeneities in initiating action potential waves was noted later by, among others, Roth and Krassowska [34] and by Trayanova *et al*. [7]. Large inhomogeneities allow an external field to polarize cells deep within the tissue, far

beyond a few space constants λ from the surface. When the polarization exceeded the excitation threshold of the cell, this phenomenon was given the name of wave emission from heterogeneities (WEH).

3.1 Wave Emission from Conductivity Heterogeneities

The mechanism underlying the phenomenon of wave emission from heterogeneities (WEH) is explained by bidomain theory [2]. In the presence of an electric field, any heterogeneity in intracellular electrical conductivity $\nabla\sigma_i \neq 0$ causes a redistribution of intracellular and extracellular currents, as sketched in panels 3.1(a) and 3.1(b). Changes in intracellular electrical conductivity may be due to differences in gap junction density (perhaps due to disease) or to anatomical inhomogeneities such as blood vessels, changing fiber orientation, intercellular clefts or fibrotic tissue [79, 80]. Regardless of the cause, the resultant change in the membrane potential of cells near the heterogeneity forms a so-called virtual electrode[1], as shown in figure 3.1 [36].

The physics of WEH can be understood by considering a very simple case, that of an infinite homogeneous, isotropic medium with a spherical obstacle of radius R, centered at the origin, in which the intracellular conductivity is nil: $\sigma_i(r < R) = 0$. The extracellular space is *everywhere* homogeneous and isotropic: it contains *no* obstacle ($\tilde{\sigma}_e$ is constant). We seek a steady-state solution when a uniform electric field $\mathbf{E} = E \cdot \hat{x}$ is applied. The relevant differential equation is a Helmholtz equation that can be solved by separation of variables in spherical coordinates:

$$\nabla^2 e - \frac{e}{\lambda^2} = 0 \tag{3.1}$$

The boundary conditions are $e(\mathbf{x}) \to 0$ as $|\mathbf{x}| \to \infty$ and $(\nabla e + \mathbf{E}) \cdot \hat{n} = 0$ at $|\mathbf{x}| = R$ ($\hat{n}$ is the unit normal to the boundary of the obstacle). The symmetries of the problem suggest

[1] When the virtual electrode occurs within the heart wall, it is sometimes called an intramural virtual electrode (IVE).

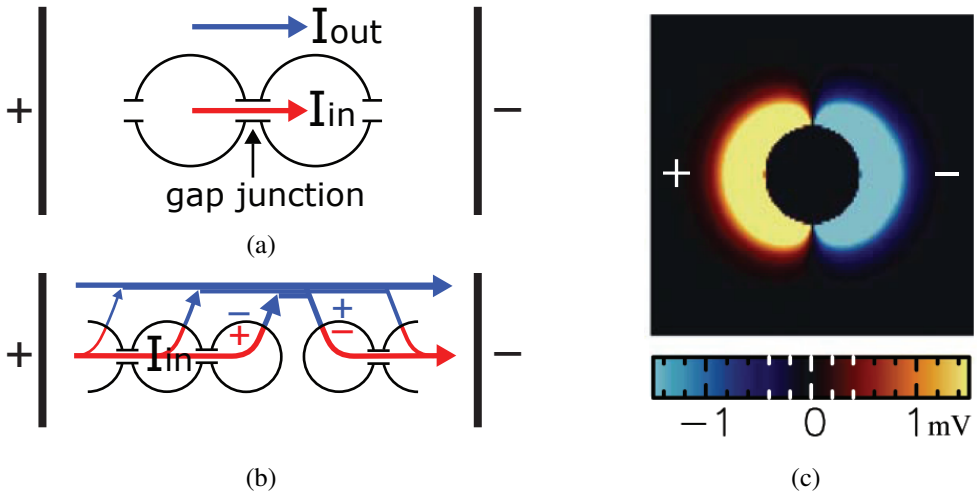

Figure 3.1: **Tissue polarization around an obstacle.**
(a) Schematic of the bidomain model with intra- and extracellular currents I_{in} and I_{out}, respectively.
(b) Induction of virtual electrodes around an anatomical obstacle. A change in the membrane potential is induced when I_{in} cannot exit the cell via gap junctions to another cell but instead has to cross the cell membrane.
(c) The homogeneous, isotropic tissue is depolarized on the side facing the positive electrode (cathode) and hyperpolarized on the side facing the negative electrode (anode). The obstacle is 6 mm in diameter, the electric field E = 0.2 V/cm, anisotropy ratio = 1. Figure adapted from [81].

a solution of the form $e(\mathbf{x}) = e(r)\cos(\theta)$ (valid in 2 and 3 dimensions). Substituting into equation 3.1 yields the differential equation:

$$\frac{d^2e}{dr^2} + \frac{(d-1)}{r}\frac{de}{dr} - \left(\frac{1}{\lambda^2} + \frac{(d-1)}{r^2}\right)e = 0. \tag{3.2}$$

In two dimensions ($d = 2$), this is the well-known modified Bessel equation whose solutions are the modified Bessel functions, and in three dimensions ($d = 3$), the solution can be found in terms of elementary functions [private communication from A. Pumir]. The solutions to equation 3.2 in 2 and 3 dimensions are thus

$$e_{2d}(r,\theta) = -\frac{K_1(r/\lambda)}{K_1'(R/\lambda)}\,E\lambda\cos(\theta) \tag{3.3a}$$

$$e_{3d}(r,\theta) = E\lambda\, e^{-(r-R)/\lambda}\left(\frac{\frac{\lambda}{r}+\frac{\lambda^2}{r^2}}{\frac{\lambda}{R}+2\frac{\lambda^2}{R^2}+2\frac{\lambda^3}{R^3}}\right)\cos(\theta), \tag{3.3b}$$

where K_1 is a modified Bessel function of the second kind and $K_1'(x) = \frac{dK_1(x)}{dx}$. Equation 3.3a is plotted in figure 3.1(c).

The maximum depolarization e_{Max} occurs on the boundary of the obstacle ($r = R$, $\theta = 0$). It is given by the following equations:

$$e_{Max,2d} = -E\lambda\left(\frac{K_1(\alpha)}{K_1'(\alpha)}\right) \tag{3.4}$$

$$e_{Max,3d} = E\lambda\left(\frac{\alpha + \alpha^2}{2 + 2\alpha + \alpha^2}\right), \tag{3.5}$$

where $\alpha = R/\lambda$. This extends the results of the cell culture experiments by Fast *et al.* who found that e depends linearly on obstacle size for small two-dimensional obstacles [78]. The maximum depolarization e_{Max} increases with obstacle size R and asymptotes to E/λ for $R \gg \lambda$ in both 2 and 3 dimensions.

When the depolarization e_{Max} around an obstacle exceeds the excitation threshold e^*, the excited cells generate a propagating action potential wave. This is the mechanism by which virtual electrodes induce wave emission from heterogeneities (WEH). The key observation is that different size heterogeneities start emitting waves at different electric field strengths; small fields can only excite large obstacles while large fields can excite smaller obstacles as well. For a given field strength E, heterogeneities larger than $R_{min}(E)$ can be recruited as wave emitting sites (WES).

The electric field strength required to excite an action potential at a heterogeneity of radius R is:

$$E_{2d}(R, e^*, \lambda) = \frac{e^*}{\lambda}\left(-\frac{K_1'(\alpha)}{K_1(\alpha)}\right) \tag{3.6}$$

$$E_{3d}(R, e^*, \lambda) = \frac{e^*}{\lambda}\left(\frac{2 + 2\alpha + \alpha^2}{\alpha + \alpha^2}\right). \tag{3.7}$$

The terms in parentheses are always equal to or greater than 1, which implies that *no wave can be generated from* any *heterogeneity if* $E < \frac{e^*}{\lambda}$. We call $E^{th} = \frac{e^*}{\lambda}$ the field excitation threshold.

The 3-dimensional case is easy to invert, giving the minimum radius R_{min} recruited by a given electric field E:

$$R_{min,3d}(E, e^*, \lambda) = \frac{4\lambda}{\zeta - 2 + \sqrt{\zeta^2 + 4\zeta - 4}} \text{ mm}, \ \zeta = \frac{E\lambda}{e^*}. \tag{3.8}$$

The 2-dimensional case can only be inverted numerically. Both cases are plotted in figure 3.2. For $E \gg e^*/\lambda$ (i.e. $\zeta \gg 1$), $R_{min} \propto (E - E^*)^{-1}$ as shown in the inset to figure 3.2.

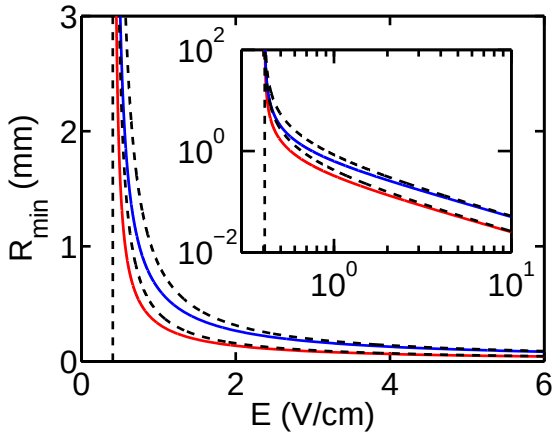

Figure 3.2: **Theoretical prediction of $R_{min}(E)$ in 2d and 3d.** Minimum heterogeneity radius recruited for wave emission in 2- and 3-dimensions (in red and blue, respectively) as a function of applied electric field strength E (ΔV = 25 mV, λ = 0.615 mm). The inset shows the same curves plotted on logarithmic axes. The limit $E \geq e^*/\lambda$ is the vertical dashed line and the dashed curves are the $1/(E - E^*)$ and $2/(E - E^*)$ asymptotes (for $R_{min,2d}$ and $R_{min,3d}$, respectively), plotted for $R < \lambda$. The higher the electric field strength, the smaller the obstacles that can be recruited. As E approaches $\Delta V/\lambda$ = 0.4 V/cm, the obstacle size grows arbitrarily large and wave emission from a heterogeneity becomes impossible.

To calculate values for $R_{min}(E)$ and $E(R_{min})$, we need experimental values for e^* and λ. Common values in the literature are 25 mV for the excitation threshold and 350–880 μm for the space constant in mammalian heart tissue [82, 83]. We use a mean value of 615 μm. Substituting e^* and λ in equations 3.6 and 3.7 yields a threshold field strength

$$E^{th} = \frac{e^*_m}{\lambda} = 0.41\text{V/cm} \tag{3.9}$$

which is in good agreement with experimental values. As further confirmation, we calculated the predicted defibrillation field strength. Defibrillation operates at or near the scale of individual cells, so we used a size on the order of a cell length, $R = 100\ \mu$m ($\alpha = 0.16$), which yielded

$$E^{defib} = 5\text{V/cm}, \tag{3.10}$$

again consistent with experimental values. Finally, the regime $R \lesssim \lambda$ in which $R_{min} \propto E^{-1}$ corresponds to field strengths

$$E_{2d}(\lambda) \gtrsim 0.69\ \text{V/cm} \tag{3.11a}$$

$$E_{3d}(\lambda) \gtrsim 1.0\ \text{V/cm} \tag{3.11b}$$

3.1.1 Assumptions and Limitations

In spite of the many assumptions inherent in this model of WEH, it correctly predicts several important experimental results: the field excitation threshold E^{th}, the defibrillation threshold E^{defib}, the linear relation between membrane polarization and obstacle size, and the inverse relation between field strength and minimum obstacle size from which a wave is emitted.

The theory assumed a purely resistive cell membrane, a homogeneous and isotropic excitable medium with a perfectly insulated intracellular inhomogeneity, and the problem was solved under steady-state conditions. A more exact solution using the full machinery of the bidomain model under more realistic conditions is the subject of ongoing research by several groups working with numerical simulations. Nevertheless, this simple derivation yields an intuitive understanding of the fundamental mechanism that already allows us to begin comparing structural tissue characteristics with the resulting activation dynamics in a quantitative manner.

3.2 Activation Model

In this section, we develop a quantitative description of the activation of cardiac tissue by multiple wave sources. We will apply this description to experimental data in the next chapter. We first present the concept of an activation map and of the activated fraction, and then proceed to the model itself in sections 3.2.2 and 3.2.3.

3.2.1 The activation map and the activated fraction

Activation maps $T(\mathbf{x})$ (sometimes called an "isochronal map") are a useful way of visualizing the propagation of action potential wavefronts across the tissue[2]. For completeness, although we do not make use of it in this thesis, we note that one can also construct a repolarization map which is similar to an activation map except that it captures the time to repolarization at every site. Thus, subtracting the activation map from the repolarization map would yield a map of action potential durations. For our purposes, we found it helpful to compress the information contained in the activation map into a scalar function of time which we called the *activated fraction*:

$$S(t) = \frac{1}{N} \sum_{(x,y)\in \mathrm{ROI}} \Theta(t - T(x,y)). \tag{3.12}$$

where $\Theta(x)$ is the Heaviside step function. The activated fraction $S(t)$ is just the cumulative fraction of activated pixels at time t. In experiments, the sum is performed over the N pixels contained in the region of interest (ROI).[3]

For longer recordings containing multiple activations, like those presented in chapter 5, $T(x, y)$ is not single-valued. An alternative definition of the activated fraction

[2]The concept of the activation map can be extended to arbitrarily many dimensions. The reader may find it useful at times to think in terms of a three-dimensional "map" T(x,y,z), but since our experiments consist of surface imaging only, we will restrict ourselves to two-dimensional maps in our discussion.

[3]In experiments, the ROI is the whole surface of the tissue from which an optical signal was recorded, and it covered between 50% and 90% of the total number of pixels in the camera's sensor.

allowed us to handle multiple activations:

$$S(t) = \frac{1}{N} \sum_{(x,y)\in \mathrm{ROI}} \Theta(V^* - V(x,y,t)) \tag{3.13}$$

where V^* is a threshold that we set at half the maximum action potential amplitude, $V^* = APA_{max}/2$. Equation 3.12 is thus a particular case of the more general equation 3.13, where the activation times $T(x,y)$ correspond to the times at which $V(x,y,t) = V^*$.

By construction, $S(t)$ is confined to the range $[0,1]$. Its derivative, $\dot{S}(t) = dS(t)/dt$, is just the distribution of activation times. The information contained in S and $\dot{S}$ can be further compressed into a set of characteristic times defined as follows[4]:

$$t_{median} \quad : \quad S(t_{median}) = 0.50 \tag{3.14a}$$

$$t_{min} \quad : \quad S(t_{min}) = 0 + \delta \tag{3.14b}$$

$$t_{max} \quad : \quad S(t_{max}) = 1 - \delta \tag{3.14c}$$

$$t_{range} \quad = \quad t_{max} - t_{min} \tag{3.14d}$$

$$t_{mean} \quad = \quad \langle \dot{S}(t) \rangle = \int_0^\infty t \cdot \dot{S}(t)\, dt \tag{3.14e}$$

$$\sigma^2 \quad = \quad \int_0^\infty (t - t_{mean})^2 \cdot \dot{S}(t)\, dt \tag{3.14f}$$

$$t_{peak} \quad = \quad \mathrm{argmax}_{t\in\mathbb{R}}\, \dot{S}(t) \tag{3.14g}$$

We illustrate the use of some of the above quantities and their relation to $S(t)$ in figure 3.3.

3.2.2 Model of wave emission from multiple sources

We assume a spatial distribution of wave emitting sources (WES) in an excitable medium, as indicated by red dots in figure 3.4. Waves spread radially outward from each source until they collide with another wave or with the boundary. Because this is an excitable

[4] In experiments, the minimum and maximum activation times t_{min} and t_{max} are highly sensitive to noise-induced outliers in the activation map, hence we introduce a small parameter $\delta = 0.01$ so as to avoid errors caused by occasional outliers.

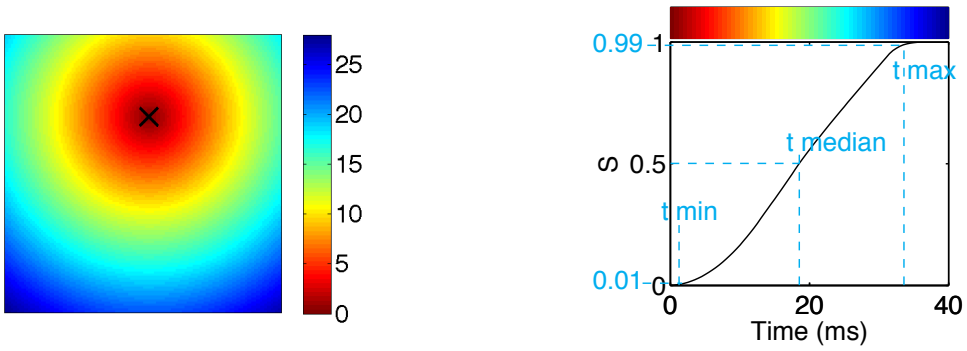

(a) (b)

Figure 3.3: **Example of activated fraction from an activation map.**
(a) Activation map in 2d with a single source indicated by an ×.
(b) Activated fraction $S(t)$ for the map in (a) and associated t_{min}, t_{median} and t_{max}.

medium, one can construct an activation map that captures the wavefront propagation dynamics.

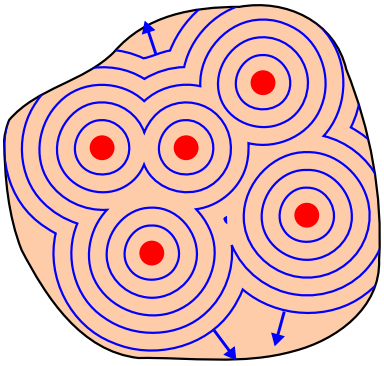

Figure 3.4: **Activation dynamics.** Isochrones showing waves propagating outward from 5 wave-emitting sources (WES). Because this is an excitable system, the waves do not interfere but simply annihilate on collision. This is seen by the merging of isochrones on contact. In 3 dimensions, the red sources would be located at different depths and the isochrones on the surface would be shifted as a consequence.

We model this process by filling the area A with N spherical waves whose radius is the maximum activation time scaled by the conduction velocity $r = v_c \cdot t_{max}$. We assume that these spheres fill the whole area and we ignore any overlaps. Each wave source fills

an area $A_1 = A/N$:

$$A_1 = \pi r^2. \tag{3.15}$$

A_1 is the inverse of the density of sources $\varrho_{2d} = N/A$,

$$\varrho_{2d} = \left(\pi(v_c \cdot t_{max})^2\right)^{-1}. \tag{3.16}$$

The same derivation in three dimensions yields

$$\varrho_{3d} = \left(\frac{4}{3}\pi(v_c \cdot t_{max})^3\right)^{-1}, \tag{3.17}$$

In general, one can show that the maximum activation time in d dimensions follows the scaling relations

$$t_{max} \propto \varrho^{-1/d} \tag{3.18a}$$

$$t_{max} \propto N^{-1/d} \tag{3.18b}$$

The first relation holds in general while the second relation holds as long as the volume is kept constant, as it is in our experiments.

An alternative derivation of the result in equations 3.18 begins by considering N randomly placed sources in a d-dimensional equilateral system of side length L. The density in d dimensions is $\varrho_d = N/L^d$. We define the mean nearest-neighbour distance $\langle r \rangle$ as the mean norm of all vectors joining nearest-neighbour sources (sources whose Voronoi cells share a face). It is easy to see that the nearest-neighbour distance scales with the source density as $\langle r \rangle \propto \varrho^{-1/d}$ in our d-dimensional cube. The ensemble average of the mean activation time t_{mean} (over many realizations of random source configurations) is directly proportional to $\langle r \rangle$: $\langle t_{mean} \rangle = \langle r \rangle / v_c$. Varying the number or the density of sources rescales $S(t)$ along the time axis, thus the mean activation time t_{mean} is proportional to t_{max}, so that $\langle r \rangle \propto \langle t_{max} \rangle$ and $t_{max} \propto N^{-1/d}$.

We tested this scaling relation in 2d by simulating activation maps produced by N randomly placed point "sources".[5] The activation map is constructed by computing the

[5]Using point sources implicitly assumes that even the largest obstacles recruited are smaller than the spatial resolution of the imaging system. This is not exactly true because the spatial resolution was about

minimum distance from each point in the map to its nearest wave source. In effect, we are simulating wave propagation as a sphere whose radius grows linearly in time.[6] The side length $L = 32$ mm and the conduction velocity $v_c = 0.5$ mm/ms were chosen to approximate experimental conditions.

An example of simulated 2d wave emission from multiple sources is shown in figure 3.5. In the upper panels are activation maps for different N. Source positions were fixed as new sources were added, which was important if we were to correctly reproduce the dynamics of WEH in cardiac tissue. New sources are marked with an $\times$ and the other sources with a $\bigcirc$. The lower panels show the activated fractions $S(t)$ for different N and the corresponding activation times t_{min}, t_{mean} and t_{max}.

Panel 3.5(g) shows how quickly the system surface was activated by the sources present. The initial phase of every curve grows quadratically with time as waves propagate outward from their sources. The growth rate slows down in the intermediate phase as the spherically expanding waves collide with one another. In the final phase, the activated fraction S approaches 1 and the growth rate decreases. The shape of the final phase depends strongly on the system shape and on wave source positions.

The results in panel 3.5(h) confirm the scaling equations 3.18. However, t_{max} does not scale exactly like $N^{-1/2}$ for $N \lesssim 10$ (or $\varrho_{2d} \lesssim 1$ cm^{-2}). This is because t_{max} is particularly sensitive to the particular configuration of sources. For example, a single source in a corner would have a t_{max} twice larger than a source in the center.

In figure 3.6, we simulated wave propagation in 3d. The activation maps shown in the figure are for the top surface of an L^3 cube with side length $L = 32$ mm. Panel 3.6(g) resembles the 2d case shown in 3.5(g) with some important differences, however. First, we notice that in the $N = 1$ case, the activated fraction $S = 0$ for some time

400 μm and some anatomical structures are larger than this. However, there are far fewer large structures than there are small ones (see figure 1.5), and thus fewer large (spatially-extended) wave sources, so this is not such a bad approximation.

[6] We ignore the effects of wave curvature on conduction velocity. One could perhaps include this via an eikonal equation, such as that given by Keener [84].

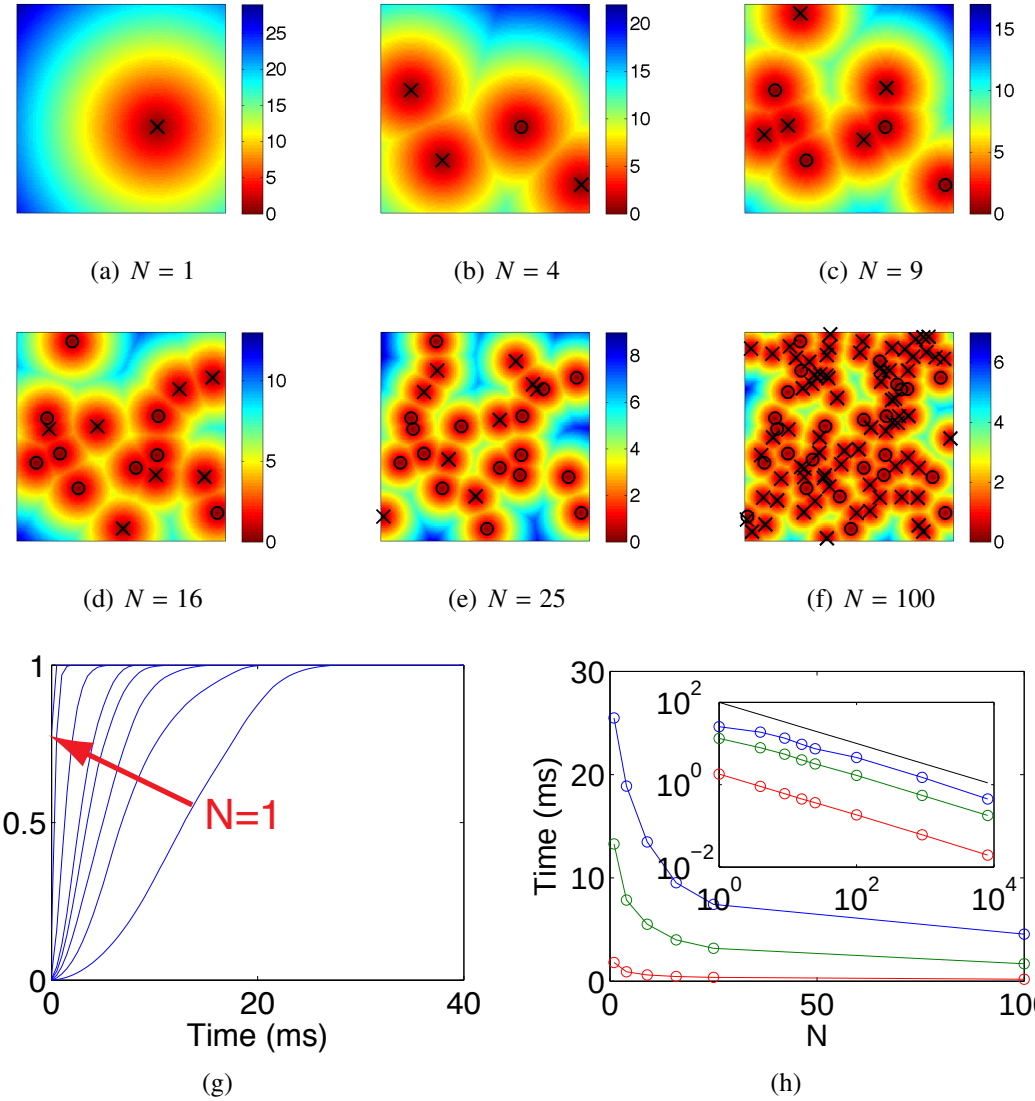

(a) $N = 1$ (b) $N = 4$ (c) $N = 9$

(d) $N = 16$ (e) $N = 25$ (f) $N = 100$

(g) (h)

Figure 3.5: **Simulated 2d activation maps.** (a-f) 2d activation maps in an area $L^2 = (32\text{ mm})^2$. New sources in each frame are marked with a $\times$ and "existing" sources with a $\bigcirc$.
(g) Activated fractions $S(t)$ for $N = 1, 4, 9, 16, 25, 100, 900$ and 8100 in the same simulation as shown in (a-f). From smallest to largest N, the curves are ordered right to left.
(h) Activation times t_{min} (red), t_{mean} (green) and t_{max} (blue) as functions of N. Inset shows the same data on logarithmic axes. (Black line has slope -1/2 to guide the eye.)

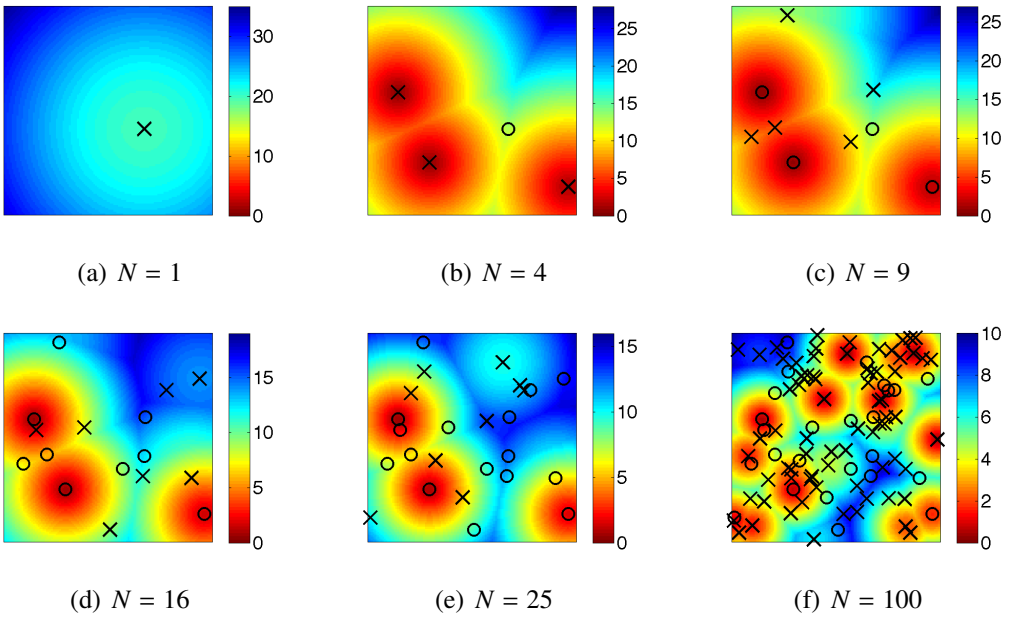

(a) $N = 1$ (b) $N = 4$ (c) $N = 9$

(d) $N = 16$ (e) $N = 25$ (f) $N = 100$

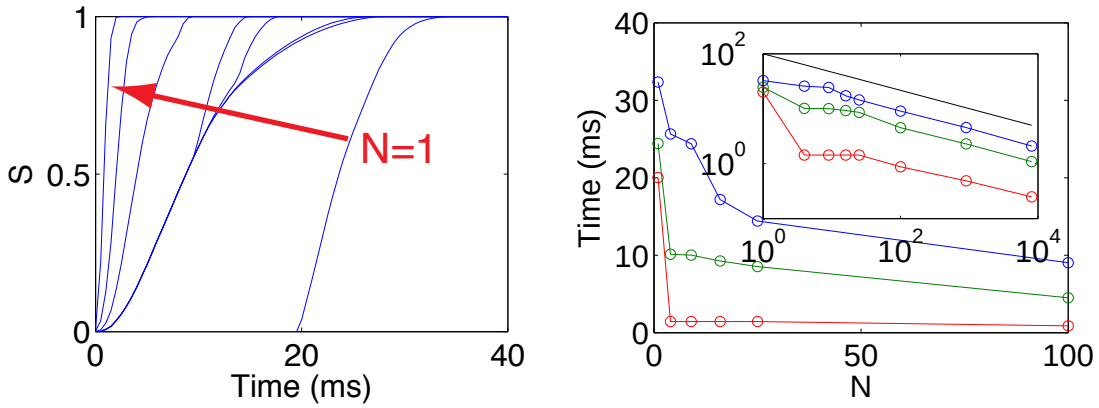

(g) (h)

Figure 3.6: **Simulated 3d activation maps.** (a-f) 3d activation maps in a volume L^2h with $L = 32$ mm and $h = 3$ mm (aspect ratio ≈ 0.1). New sources in each frame are marked with an $\times$ and "existing" sources with a $\bigcirc$. The activation time directly above each wave source n is determined by the depth of the source z_n, $t_n = z_n/v_c$.

(g) Activated fractions $S(t)$ for $N = 1, 4, 9, 16, 25, 100, 900$ and 8100 in the same simulation as shown in (a-f). From smallest to largest N, the curves are ordered right to left.

(h) Activation times t_{min} (red), t_{mean} (green) and t_{max} (blue) as functions of N. Inset shows same data on logarithmic axes. (Black line has slope -1/3 to guide the eye.)

after the simulation begins because it takes time for the wave to propagate from the source to the surface. As more sources are added, it becomes increasingly likely that at least one will be located near the surface, so the onset time of S moves to the left (it approaches zero). The initial phase no longer grows quadratically but is a sum of modified second-order functions: $S_{initial}(t) = \sum_{i=1}^{M} \pi[(v_c \cdot t)^2 - h_i^2]\Theta(v_c \cdot t - h_i)$, where i is an index over M surface area elements and the step function $\Theta(\cdot)$ implements the delay for the wave to reach the surface. (This formula is only valid when the expanding waves do not collide with each other or with a system boundary.) The intermediate phase looks mostly similar to the 2d case save for one observation: the curves for $N = 4, 9, 16, 25$ appear to build upon one another. This is due to the fact that sources # 2–4 are located close to the surface while sources # 5–25 are located further below and thus only "appear" after some finite time, where they contribute to increasing the activated fraction S. This effect disappears at higher N because there are sufficient additional sources in each step to ensure that some will be close to the surface where they can contribute to the initial phase. Thus, (assuming a convex-shape system) the intermediate phase reveals the presence of additional subsurface sources by upward bends in S (positive second derivatives). The convexity condition follows from the fact that a wavefront traveling through a concave system can sometimes become longer simply because of the boundary shapes, leading to a rise in dS/dt. Finally, the final phase does not appear to differ in the 3d case.

In panel (h), we already see that the random source configurations have an even greater influence in 3d than they did in 2d: all three measures t_{min}, t_{mean} and t_{max} deviate from the expected $-1/3$ exponent for $N \lesssim 16$ ($\varrho_{3d} \lesssim 0.5$ cm^{-3}). If we project the 3d sources onto a 2d plane, they would have a density $\varrho_{2d} = \varrho_{3d} \cdot L = (0.5 \text{ cm}^{-3})(3.2 \text{ cm} = 1.6 \text{ cm}^{-3}$, comparable with the density threshold found in the 2d example above.

In the next section, we simulate 100 realizations of randomized wave source configurations in order to extract the ensemble scaling relations, as well as to resolve the more difficult cases that occur when the system has a very large or very small aspect ratio, an important issue we have not yet addressed.

3.2.3 Surface dynamics in 3 dimensions

In our experiments, we could only measure the activation dynamics on the surface of 3-dimensional cardiac tissue. Observation of only part of the system introduces a new element in the scaling relation $t_{mean} \propto N^{-1/d}$ that modifies the exponent. For reasons that will become clear shortly, we rewrite this as

$$t_{mean} \propto \varrho_d^{-\gamma} = \left(\frac{N}{V_d}\right)^{-\gamma} \tag{3.19}$$

where $V_d = L^d$ is the volume of a system with sides of length L.

Let us consider the L^2 surface of a 3d volume $V = L \cdot L \cdot h$, where L is the length of the system along the x and y axes and h is the length along the z axis (the origin of the coordinate system is in the corner of the upper surface of the volume). The 3d activation "map" will scale as expected. However, depending on the aspect ratio h/L and on the density of sources ϱ, the *surface* activation dynamics can appear to scale like a 1d, 2d or 3d system, in the sense that the exponent γ in $t_{mean} \propto \varrho^{-\gamma}$ approaches 1, $1/2$ or $1/3$.

We might expect the regime $h/L \gg 1$ to have little or no relevance for the heart because the ventricle wall is only about $1/10$ as thick as it is wide. However, the presence of the interventricular septum (the wall that separates the left and right ventricles) in the whole heart introduces a "depth" on the same order as L; the distance waves have to travel to reach the epicardium from the septum is comparable to the distance they have to travel to travel across the epicardium, but the waves are only visible to us when they reach the epicardium.

The transition points N^* trace out a curve in the space of scaling exponents $\gamma = \gamma(\frac{h}{L}, N)$. The curve can be found by solving for the minimum number of sources required to create a cubic unit cell. This condition follows from the fact that a uniform packing of point sources in a volume is equivalent to filling the volume with identical boxes, each of volume L^2h/N. For large N, the boxes are cubes with side length $\sqrt[3]{L^2hN}$. However, for small N, its dimensions are constrained by the dimensions L and h of the volume. For $h/L < 1$, the minimum number of sources for which we can construct a cubic unit cell is given by $N_-^* = (L/h)^2$ or $\varrho_-^* = h^{-3}$. For $h/L > 1$, it is given by $N_+^* = h/L$ or $\varrho_+^* = L^{-3}$. These results suggest a universal relation whereby the transition point is given by the inverse cube of the shortest dimension of the system.

For aspect ratios $0 < h/L < 1$, there exists a transition point N_-^* that separates 2d-like from 3d-like scaling behaviour; 2d-like scaling appears for $N < N_-^*$ and 3d-like scaling for $N > N_-^*$, with a smooth transition between the two regimes. For aspect ratios $1 < h/L$, there is a transition point N_+^* that separates 1d-like from 3d-like scaling; 1d-like for $N < N_+^*$ and 3d-like for $N > N_+^*$. When the aspect ratio $h/L = 1$, the scaling is 3d-like for all values of N.

The curves $N^*(\frac{h}{L})$ are plotted in figure 3.7. In the upper regions ($N > N^*$), γ approaches $1/3$; in the lower left region ($N < N_-^*$, $\frac{h}{L} < 1$), it approaches $1/2$; and in the lower right region ($N < N_+^*$, $\frac{h}{L} > 1$), it approaches 1.

Finding a general analytic expression for the scaling exponent γ would require finding the average nearest-neighbour distance as a function of N in a system with aspect ratio h/L. This is the (difficult) problem of finding an optimal packing of unit cells of unusual shape. Therefore, we used a numerical approach to estimate the scaling exponents $\gamma(\frac{h}{L}, N)$.

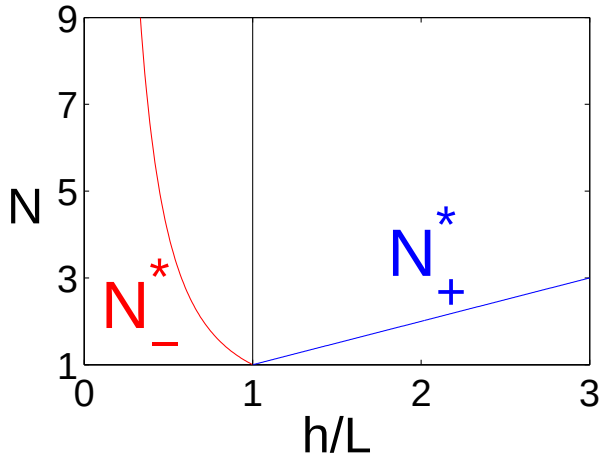

Figure 3.7: **Phase space of the scaling exponent γ in $t_{mean} \propto N^{-\gamma}$ as a function of aspect ratio h/L and number of sources N.** The branches N^* trace out the combinations of h/L and N for which the unit cell (see text) is a cube. The left branch N^*_- separates $\gamma \to 1/2$ (below) from $\gamma \to 1/3$ (above) and the right branch N^*_+ separates $\gamma \to 1$ (below) from $\gamma \to 1/3$ (above). The vertical black line at $h/L = 1$ corresponds to fully 3d system whose scaling exponent $\gamma = 1/3$, independent of N.

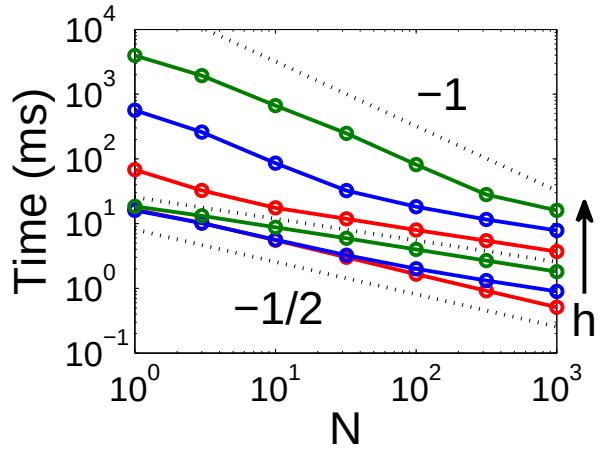

Figure 3.8: **Simulated mean activation time as a function of the number of sources for different aspect ratios h/L.** The mean activation time t_{mean} was computed as a function of N for 100 different random point source configurations. Here we plot the mean over the 100 realizations. The depths $h = 0, 0.2, 1.6, 12.8, 102.4$ and 819.2 cm correspond to the curves from the lowest to the highest (as indicated by the arrow on the right-hand side of the plot). $L = 3.2$ cm is held constant. The dashed lines to guide the eye have slopes $(-1/2, -1/3$ and $-1)$, from bottom to top, respectively.

In figure 3.8, we explore the relationship between aspect ratio h/L and number of sources N. As predicted, $t_{mean}(0, N)$ scaled like $N^{-1/2}$ in a purely 2d system ($h/L = 0$) and $t_{mean}(1, N)$ scaled like $N^{-1/3}$ in a purely 3d system ($h/L = 1$).

For the highest aspect ratios we simulated, $h/L = 32$ and $h/L = 256$, we found two scaling regimes with different transition points: $t_{mean}(32, N)$ scaled like $N^{-0.81}$ for $N \leq 32$ and like $N^{-0.41}$ for $N \geq 32$. Similarly, $t_{mean}(256, N)$ scaled like $N^{-0.87}$ for $N \leq 316$. There were not enough points to properly fit a scaling exponent for large N at this aspect ratio. The transition points $N^*_+(\frac{h}{L})$ lie between $N = 10$ and 32 and between $N = 100$ and 316 for $h/L = 32$ and 256, respectively. This is consistent with our prediction that the transition curve N^*_+ scales with h/L.

3.2.4 Relating activation dynamics to heart structure

With the results we have just obtained, we are now in a position to link measurements of activation dynamics with measurements of heart structure. In the previous sections, we have shown how activation time depends on the wave source density. Earlier in this chapter, we also presented a relation for the electric field required to trigger an AP from an obstacle of size R. Putting both these relations together allows us to compare the size distribution $p(R)$ with the activation times $t_{mean}(E)$. We use equation 3.8 to compare structure measurements with activation dynamics, but first a simple analytical derivation will help us develop some intuition about the relation between structure and dynamics.

The mean activation time $t_{mean} \propto \varrho^{-\gamma}$ and we define $t_{mean} \propto E^{-\beta}$. From the structure measurements in section 1.1.1, we know that the size distribution $p(R) \propto R^{-b}$. By simple integration,

$$\varrho(R_{min}) = \frac{1}{V} \int_{R_{min}}^{\infty} p(R) dR, \tag{3.20}$$

where $\varrho(R_{min})$ is understood to be the cumulative density of inhomogeneities of radius R_{min} or greater. Thus we have $\varrho \propto p^{1-b}$. Combining these relations between t_{mean}, ϱ and

E yields

$$E^{-\beta} \propto t_{mean} \propto \varrho^{-\gamma} \propto R_{min}^{-(1-b)\gamma} \tag{3.21}$$

$$E \propto R_{min}^{\frac{(1-b)\gamma}{\beta}} \tag{3.22}$$

In the regime $R_{min} \gtrsim \lambda$ (or $E \gtrsim E^{th}$), $E \propto R_{min}^{-1}$ (compare equation 3.8). Inserting this in equation 3.22 yields a relation between the scaling exponents for the activation dynamics (β) and the size distribution (b), mediated by the exponent for the aspect ratio, $\gamma(\frac{h}{L}, \varrho)$:

$$\beta = (b-1) \cdot \gamma\left(\frac{h}{L}, \varrho\right). \tag{3.23}$$

We see that the aspect ratio of the system introduces a continuous variable into the otherwise fixed relation between β and b, between activation dynamics and structure.

CHAPTER 4

WAVE EMISSION FROM HETEROGENEITIES

4.1 Background

Previous research, both theoretical and experimental, showed that conductivity heterogeneities of the tissue are polarized by an external electric field: theoretical investigations [1, 2, 81] and experiments on cardiomyocyte cell cultures [78] and porcine left ventricular wall preparations [85, 77] found that the induced change in membrane potential ΔV_m is proportional to the size of the heterogeneity R and to the strength of the electric field applied: $\Delta V_m \propto E \cdot R$.

The first experiments specifically on polarization around heterogeneities were carried out by Fast *et al.* [78] in monolayer cell cultures, with intercellular cleft lengths in the range 50–250 microns and electric fields E = 7.5–19.3 V/cm. They found a linear dependence between the polarization e and the obstacle size R. The maximum depolarization at a 250 μm-long intercellular cleft was 80 mV (160 mV) for a field strength E = 8.5 V/cm (18.0 V/cm), 2–3 times larger than the excitation threshold of a cell.

Later, Sharifov *et al.* [77, 85] and Zemlin *et al.* [76] imaged the electrical response of cardiac tissue to an external electric field pulse, intramurally via a cut surface, which gave them access to the intramural dynamics [77, 85] and on the surface via the epicardium and the endocardium [76].

Sharifov *et al.* tested electric field strengths from 1–48 V/cm while Zemlin *et al.* focused on the near-threshold regime (E between 0.4 and 3.3 V/cm). Both groups found that intramural virtual electrodes (IVE)—virtual electrodes situated within the bulk of ventricular tissue—contribute to faster activation of the myocardial tissue at field strengths lower than the defibrillation threshold ($E < 6$ V/cm).

We hypothesized that the cardiovasculature is the primary source of IVE at near-threshold field strengths. Since direct access to intramural activity is still not possible, we looked for indirect measures that might confirm or reject this hypothesis. We found two types of measures that are robust in the low and intermediate field strength regimes, respectively. The first is a direct count of breakthrough sites on the imaged surface. The second is the distribution of activation times. The results for each are presented in sections 4.3.2 and 4.3.7, respectively.

In this chapter, we extend the work of Sharifov, Zemlin and coworkers by quantifying the activation dynamics in whole rabbit hearts and in excised right ventricle preparations from canines. We compare these to the activation model presented in the previous chapter, and suggest a link between dynamics and the cardiovasculature.

4.2 Introduction to Experimental Results

We carried out experiments on two kinds of preparations: (1) the perfused whole rabbit heart, and (2) the excised and perfused outer wall of the canine right ventricle.

To orient ourselves, we begin with examples of activation map data we obtained and analyses thereof. Figures 4.1, 4.2, 4.3 and 4.4 show the activation dynamics measured in one of each of the following preparations: canine endocardium, canine epicardium, rabbit left ventricle (LV) and rabbit right ventricle (RV). Field strengths E=0.1–2 V/cm were studied in the canine preparations and E=0.1–6 V/cm in the rabbit hearts. The figures all follow the same pattern, which we describe here to avoid needless repetition:

(a,c) Activation map at low and moderate field strengths.

(b,d) Excited fraction $S(t)$ in black and its derivative in red for the maps shown in (a) & (c). The colorbar maps the time axis to the colorbar in (a) & (c).

(e) The surface $S(t, E)$. The contours below correspond to $t_{min}(E)$ (blue), $t_{median}(E)$ (green) and $t_{max}(E)$ (red).

(f) The curves $t_{min}(E)$ (blue, dot-dashed), $t_{median}(E)$ (green, solid) and $t_{max}(E)$ (red, dashed) plotted alone for clarity.

(g) The surface $\dot{S}(t, E)$. The contours below correspond to $t_{mean}(E)$ (red, solid) and $t_{peak}(E)$ (black, dashed).

(h) The curves $t_{mean}(E)$ (red, solid) and $t_{peak}(E)$ (black, dashed) plotted alone for clarity.

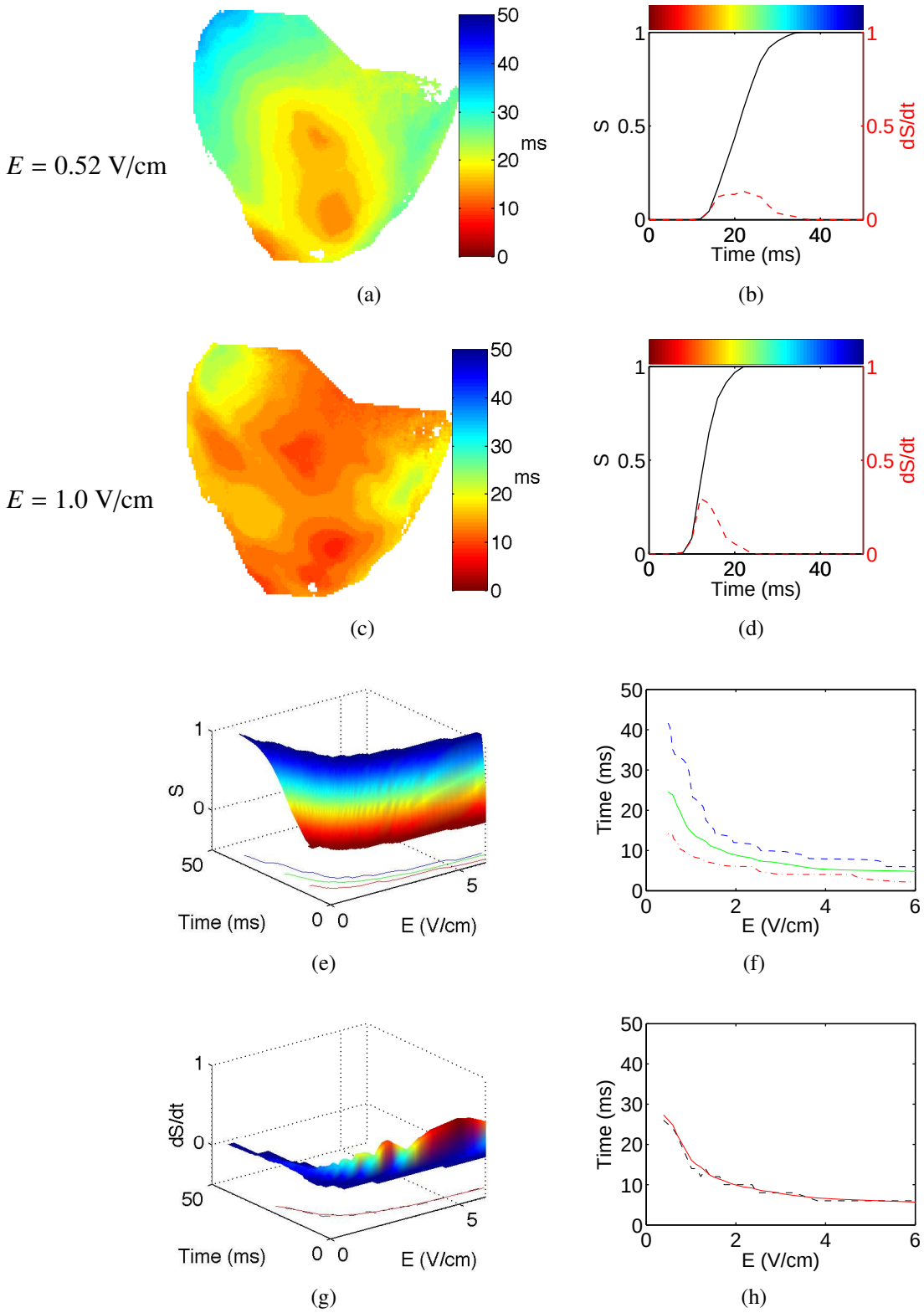

Figure 4.1: Activation dynamics on rabbit LV epicardium. See page 75 for description (same heart as in figure 4.2). Time bins are 2 ms.

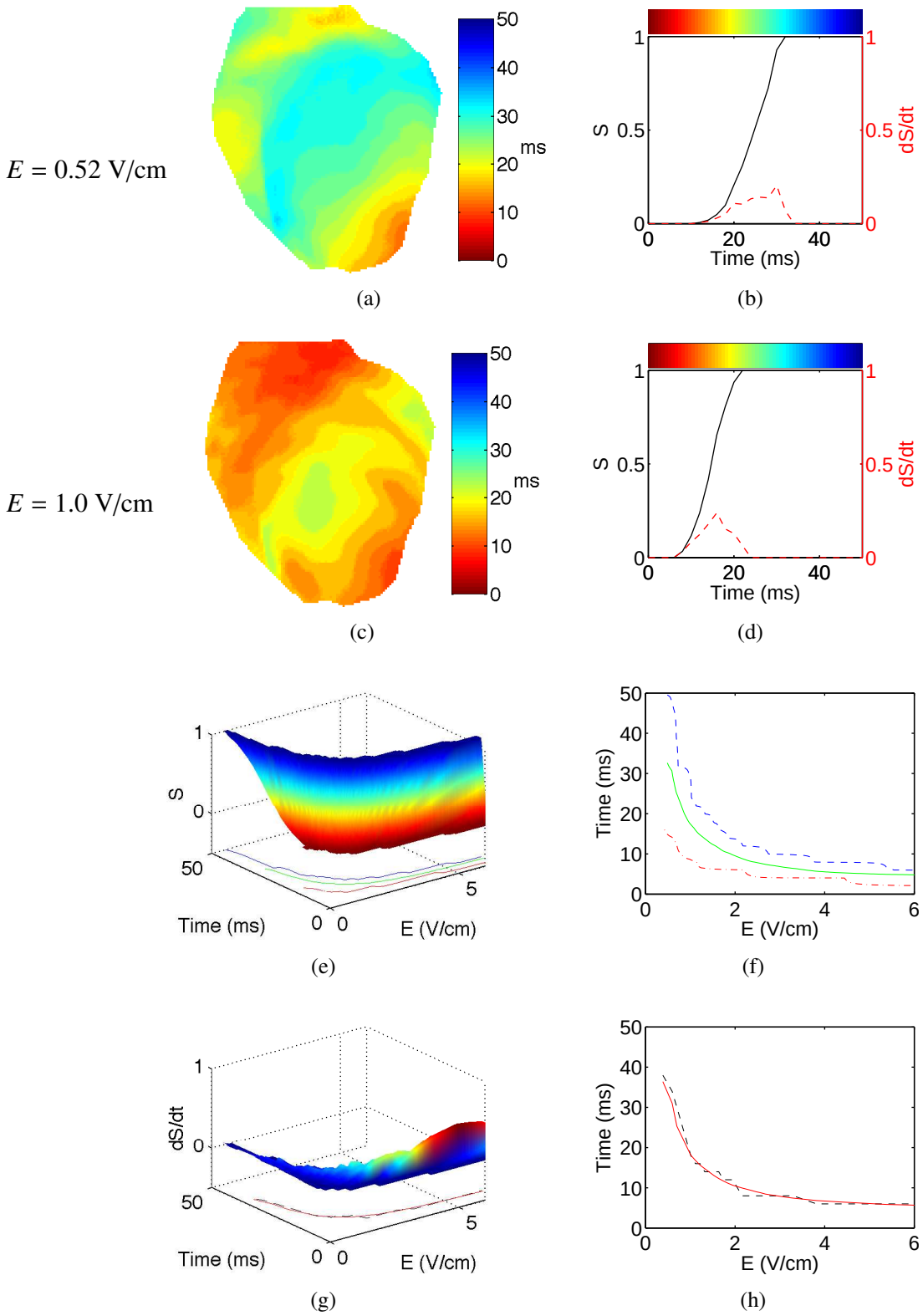

Figure 4.2: Activation dynamics on rabbit RV epicardium. See page 75 for description (same heart as in figure 4.1). Time bins are 2 ms.

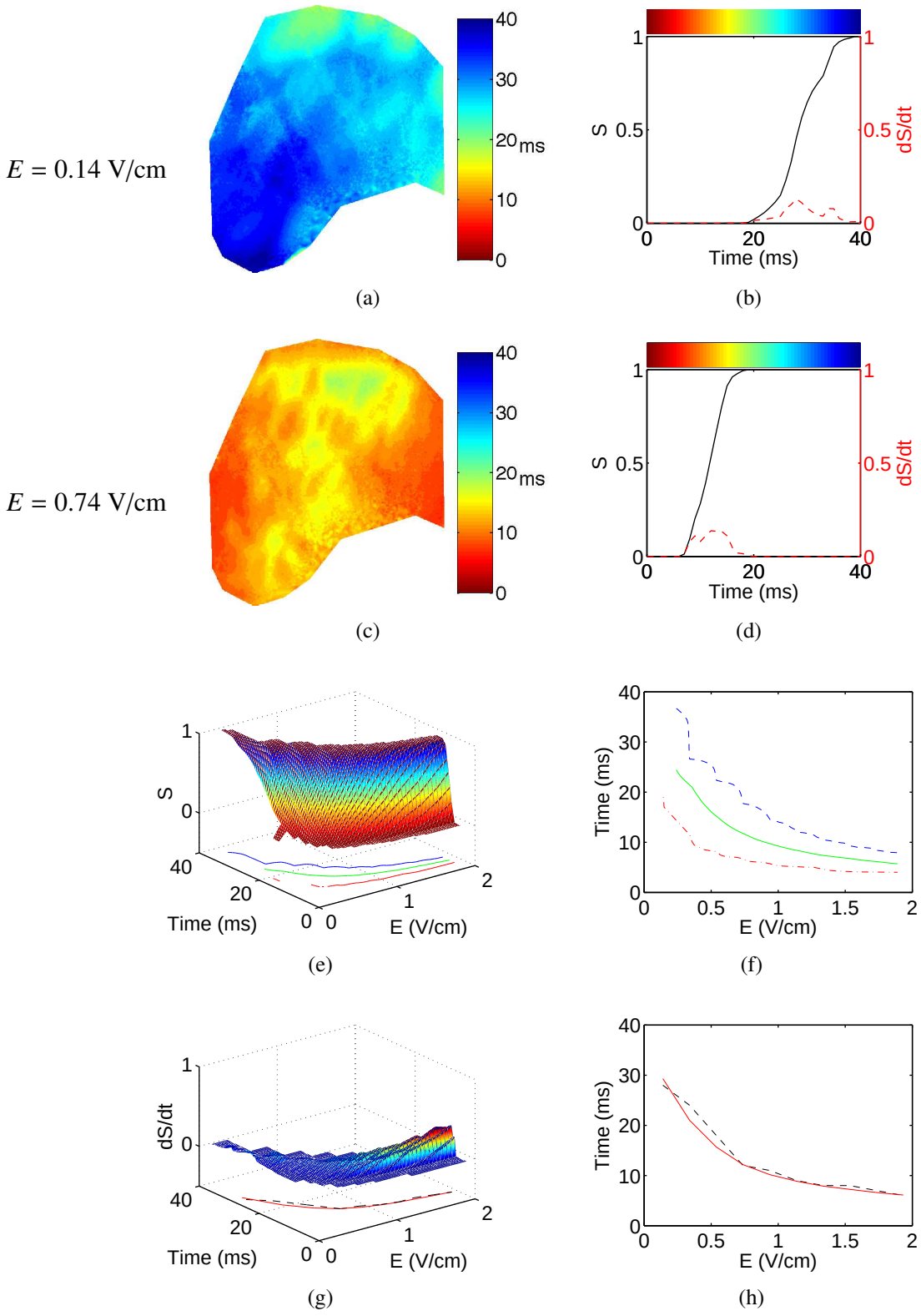

Figure 4.3: Activation dynamics on canine epicardium. See page 75 for description (same tissue as in figure 4.4). Time bins are 1 ms.

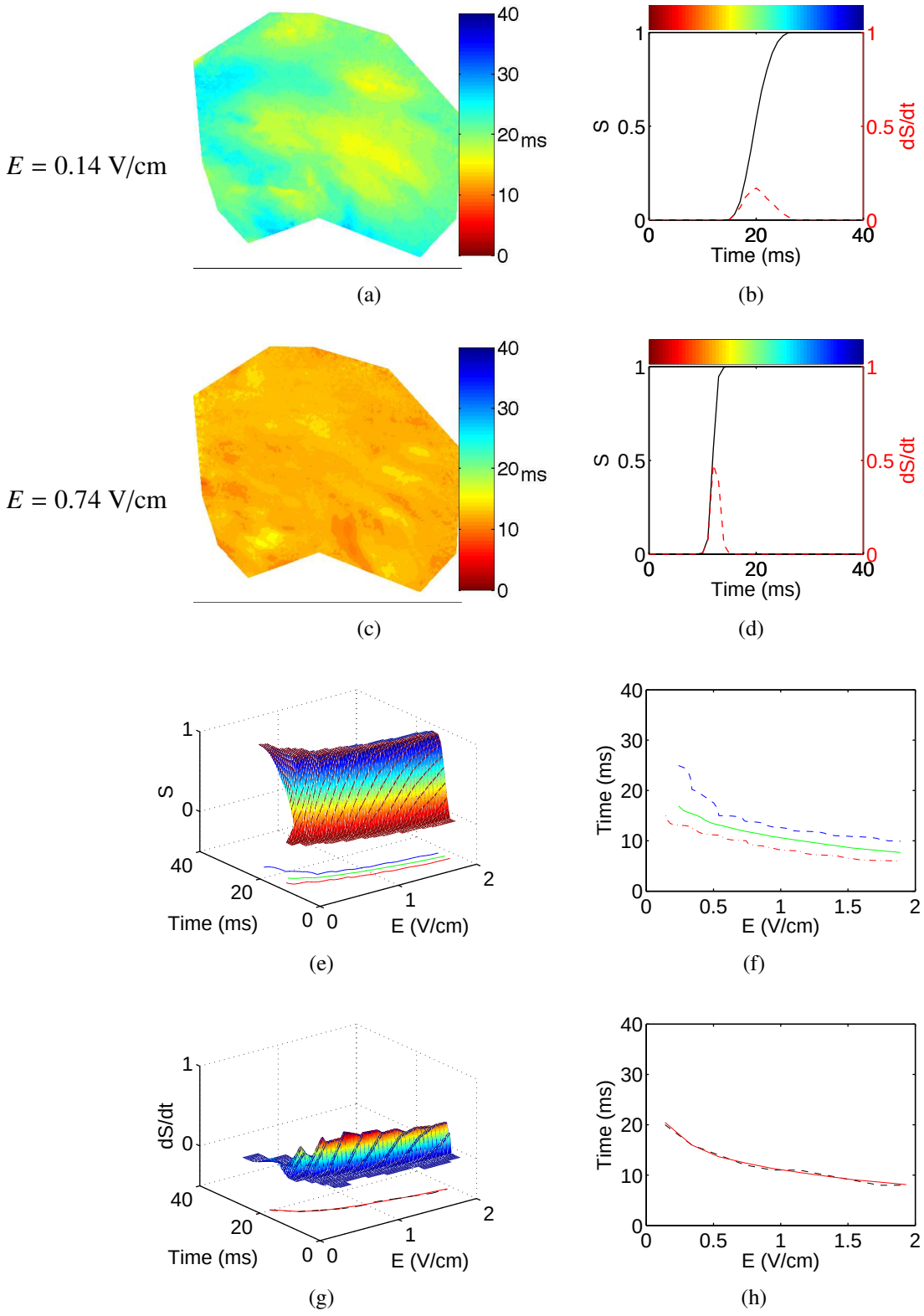

Figure 4.4: Activation dynamics on canine endocardium. See page 75 for description (same tissue as in figure 4.3). Time bins are 1 ms.

4.3 Quantifying Activation Dynamics

In the next sections, we report results on the reproducibility of activation maps, on the number of breakthrough sites, on endocardial and epicardial patterns, on activation time scaling and onset time, on the mechanisms of faster activation, and on linking dynamics with structure.

4.3.1 Reproducibility

First, we verified that the activation patterns produced by electric field pulses were reproducible. Figure 4.5 confirms that this is the case. Ten activation maps at 0.52 V/cm and ten at 1.0 V/cm were constructed for ten electrical pulses applied to the same rabbit heart. The maps are surprisingly similar. For each field strength, they have the same range of times (displayed as colour) and the same spatial pattern of activation. Such robust reproducibility is the first indication that the heart's electrical response to external field pulses is mediated by anatomical structures.

The activation patterns changed as the pulse strength was varied. The pattern at low field strength (see figures 4.1(a) and 4.2(a) – 0.52 V/cm) was characterized by one or two sources of excitation from which waves propagate across the whole field of view. At moderate field strength (see figures 4.1(d) and 4.2(d) – 1.04 V/cm), red-orange spots appeared against a field of green-blue, indicating the presence of additional activation sites.

Another feature we observed when comparing activation maps from small and large E was that the activation times became shorter when the field strength was increased, never longer. This same observation was seen in every heart we investigated, which is consistent with the hypothesis that for a given field strength, all structures of a given

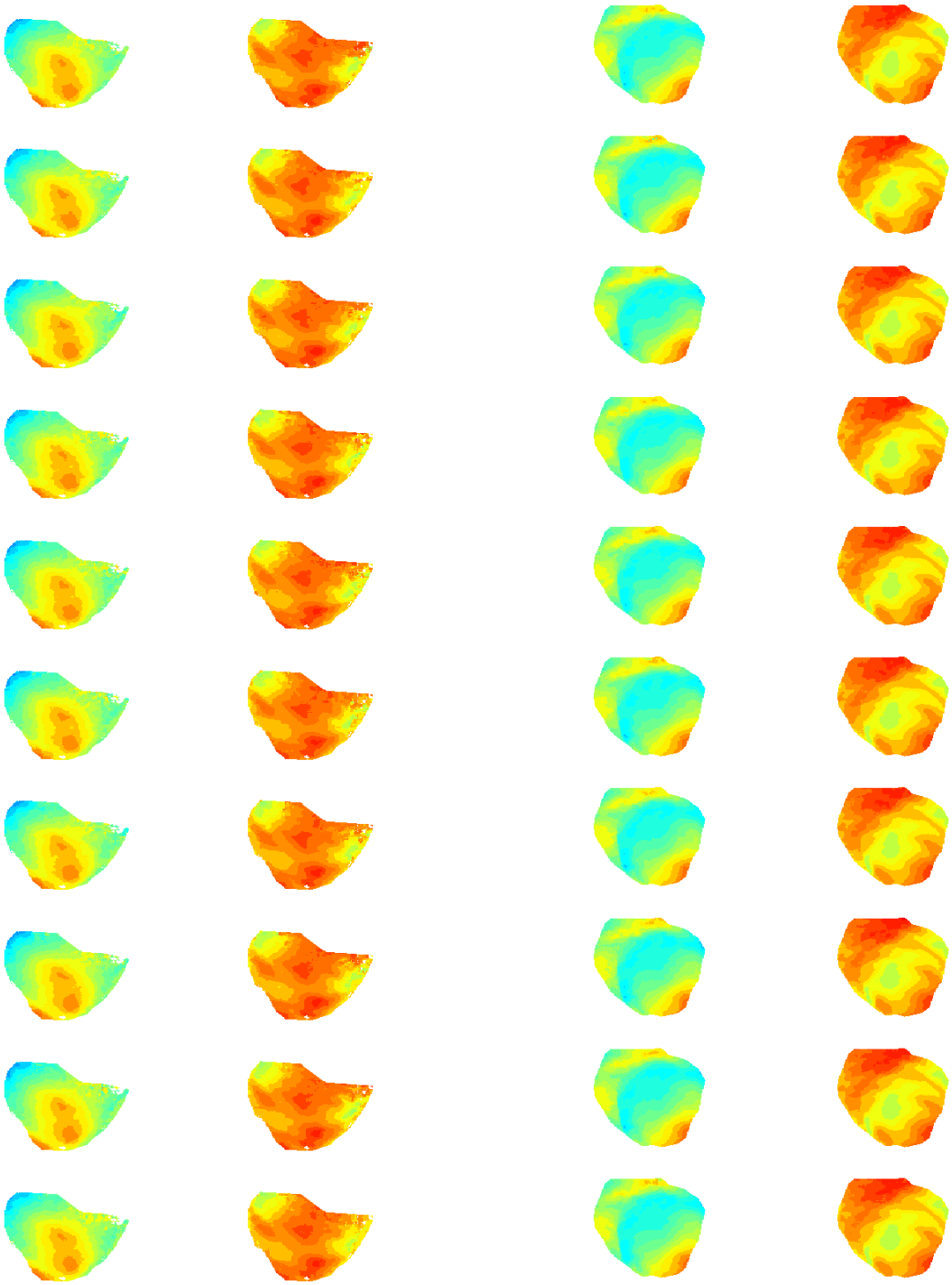

(a) 0.52 V/cm, LV (b) 1.0 V/cm, LV (c) 0.52 V/cm, RV (d) 1.0 V/cm, RV

Figure 4.5: **Reproducibility of activation patterns.** Activation maps from rabbit LV epicardium (a,b) and rabbit RV epicardium (c,d) from 10 consecutive pulses at two different field strengths. Red is early activation and blue is late. Pulse interval was 500 ms.

size or larger are recruited as wave-emitting sources. In other words, the recruitment of WES is cumulative: sources do not cease to act as WES when E is increased.

4.3.2 Number of activation sites

The activation dynamics on endocardium and epicardium were studied using canine ventricle preparations. Excised ventricles were essential for studying endocardial activation dynamics, hence the use of a partial heart. Canine hearts were used because they have large ventricle surfaces and are more than 5 mm thick. Examples of epicardial and endocardial measurements from one canine right ventricle preparation were shown in figures 4.3 and 4.4, respectively. Each figure showed one activation map at low field strength (0.14 V/cm) and one at medium field strength (0.74 V/cm).

Based on the theory developed in section 3.2, we expected to see activation waves appear on the surface of the tissue in response to an external electric field pulse wherever this pulse recruits a heterogeneity. In effect, the (x, y)-location of the heterogeneity is simply projected onto the tissue surface. Thus we attributed each wave we saw appear on the surface to an intramural virtual electrode (IVE). Since the heart contains heterogeneities of varying sizes, we also expected the number of recruited heterogeneities to grow as we increased E. These sites would appear as "breakthrough sites," local minima of the activation maps, which is the criterion we used to identify and count them.

The canine ventricle preparation is an ideal platform for observing surface breakthroughs from intramural virtual electrodes (IVE) because it has a large surface area ($\sim 8 \times 5\text{cm}^2$), with well-separated structures. Thus, we expected we would be able to resolve individual breakthrough sites if we focused on low field strengths ($E < 2$ V/cm). This expectation proved correct and we were able to measure the density of surface breakthrough sites on the epicardium and the endocardium of the right ventricle.

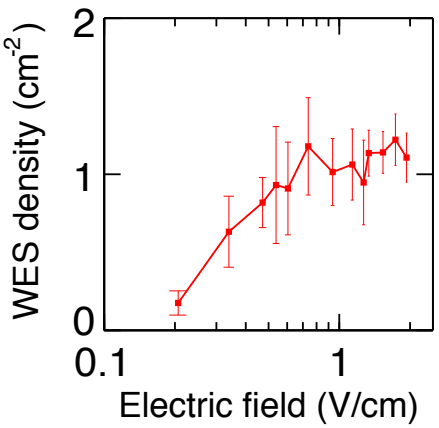

Figure 4.6: The density (number/area) of surface breakthrough sites in canine ventricle increases with electric field strength.

Figure 4.6 shows the density of breakthrough sites detected in response to single pulses applied to quiescent tissue. We found that wave emission started at 0.2–0.3 V/cm, depending on the tissue preparation. At this threshold E, the density of surface breakthrough sites was 0.17 ± 0.08 cm^{-2}, which corresponds to 6 sources in a 5×8 cm^2 ventricular preparation. The density then increased with electric field strength and appeared to reach a plateau around 1.1 cm^{-2} around $E = 1$ V/cm. This may have been due to the lower spatial resolution used for imaging the ventricles (spatial resolution was traded for a larger field of view).

4.3.3 Comparing endocardial and epicardial activation patterns

A new feature became apparent when we compared the canine activation maps from epicardium and endocardium at different field strengths: surface breakthrough sites on the epi- and endocardium seemed to appear in matching locations but at different times. Is there a connection between the breakthroughs we see on the epicardial surface and those on the endocardial surface? Unfortunately, the experiments were designed to focus on measuring activation maps on each surface independently, thus we could not

exactly match epicardial and endocardial activation patterns. We have begun planning for a series of dedicated experiments with high-accuracy camera registration so that endocardial and epicardial maps can be matched precisely. Still, our data offer a glimpse into the possible outcomes of these experiments.

If surface breakthroughs on epi- and endocardium have the same source, then the difference in times-to-breakthrough must be a function of differing path lengths to the endo- and epicardial surfaces. Three hypotheses then offer themselves:

(1) the source of the breakthroughs could be one and the same;

(2) the sub-epicardium structures could mirror sub-endocardium structures but with sizes scaled up or down, yielding different times-to-fire; or

(3) structures could be "mirrored," shallow[1], and at different depths, yielding different times-to-breakthrough.

Differences in time-to-fire cannot exceed the pulse duration of the electric field. Since the difference in breakthrough times in our data (7–9 ms) is longer than the pulse duration (5 ms), we can rule out the second hypothesis. We could rule it out even further if endo- and epicardial activation patterns match over a range of field strengths, which would leave us with hypotheses 1 and 3.

These we could test by comparing the times-to-breakthrough to the difference between them. Later times-to-breakthrough would indicate deeper sources. The time-to-breakthrough is bounded by the time needed for a wave to travel from one surface to the other: h/c_v where h is the thickness of the tissue. On the other hand, a short time-to-breakthrough would indicate a shallow source. Short times on both surfaces would imply that there are two distinct sources. The relevant condition to decide between hypotheses 1 and 3 is thus

$$v_c(t_{endo} + t_{epi}) \leq h, \tag{4.1}$$

[1]The shallowness condition is important because if the structures are mirrored and deep, then they are simply the same structure and we recover hypothesis #1.

which simply expresses in mathematical language that the combined depths of the sub-epicardium and sub-endocardium sources cannot exceed the thickness h of the tissue. If the breakthroughs were due to a single source (hypothesis 1), we could measure the distance from the depth midpoint by measuring the conduction velocity and then computing $\Delta z = \Delta t \cdot v_c/2$.

4.3.4 Activation time scaling

Following the definitions of $S(t)$ and of the activation times on page 62, we measured the activation times t_{min}, t_{max}, t_{mean} and σ as functions of E in each of our epicardial preparations. The averages and their standard deviation across experiments are plotted in figure 4.7.

Comparing the curves $t_{mean}(E)$ in figure 4.8(a) to the reference line (dashed, slope = -1), it is clear that $\beta < 1$ in all cases. Using the relation $\beta = (b-1) \cdot \gamma$ derived in section 3.2.4, we find that the predicted scaling exponent b of the heterogeneity size distribution $p(r)$ is bounded from above to give $b \leq 3$ or $b \leq 4$ if we assume a purely 2d or 3d system, respectively.

Figure 4.8(a) shows the mean activation time as a function of field strength. It decreases monotonically from a maximum of ~30 ms at low E to a minimum of ~6 ms at high E. The upper bound at low E is a consequence of the transition from no WES to some WES at around $E^{th} = 0.41$ V/cm. The lower bound at high E is consistent with defibrillation—synchronized activation from every microscopic region of tissue. It also follows from the finite time resolution of the imaging system, in this case 2 ± 2 ms. In the intermediate range—covering about a decade in E (~ 0.4 V/cm – 4 V/cm)—we find a scaling relation $t_{mean} \propto E^{-\beta}$ with $\beta = -0.52 \pm 0.04$ in the left ventricle and -0.57 ± 0.02 in the right ventricle.

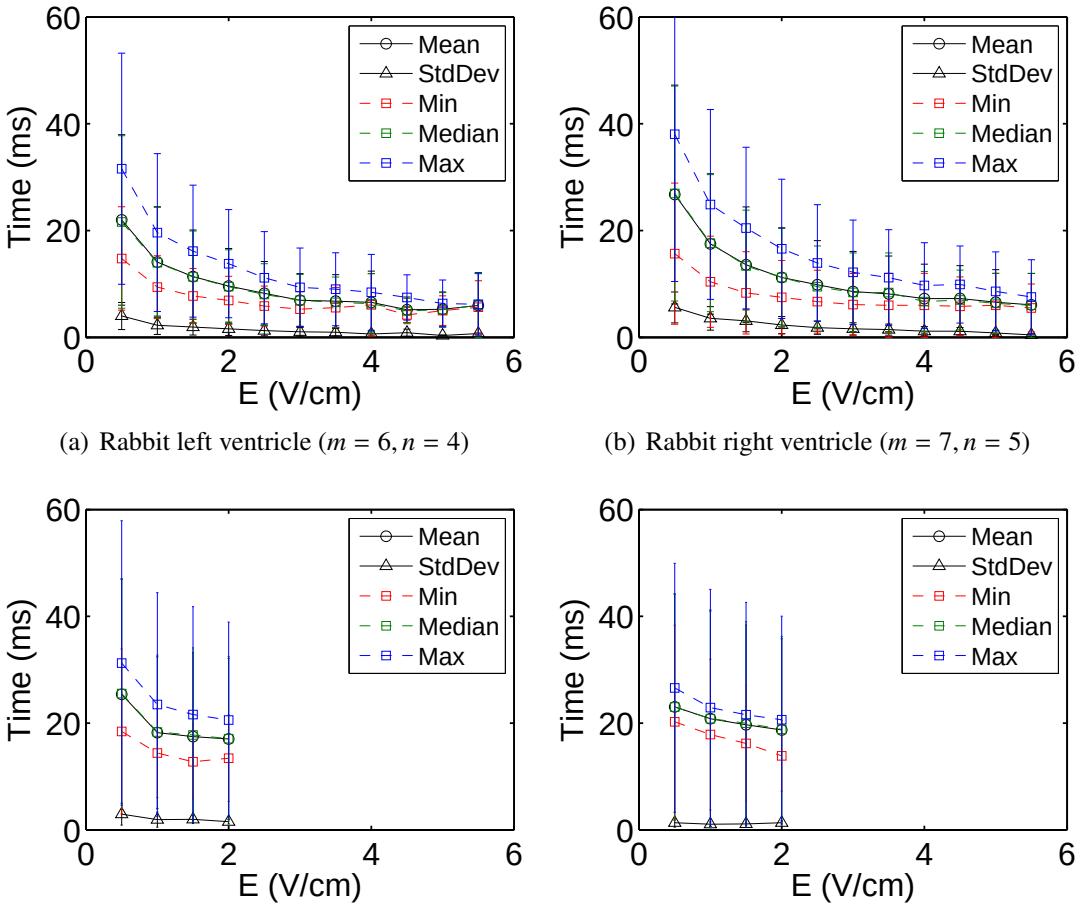

(a) Rabbit left ventricle ($m = 6, n = 4$)

(b) Rabbit right ventricle ($m = 7, n = 5$)

(c) Canine epicardium ($m = 4, n = 3$)

(d) Canine endocardium ($m = 4, n = 3$)

Figure 4.7: Activation times from (a,b) rabbit and (c,d) canine experiments. Panel captions give the number of measurements m and the number of preparations n.

As shown in figure 4.9, t_{mean} is nearly identical to t_{median}, which demonstrates that the activation time distribution $S(t)$ is symmetric about its mean. This finding is significant because it tells us that the distribution of activation sites, and hence of heterogeneities, is homogeneous.

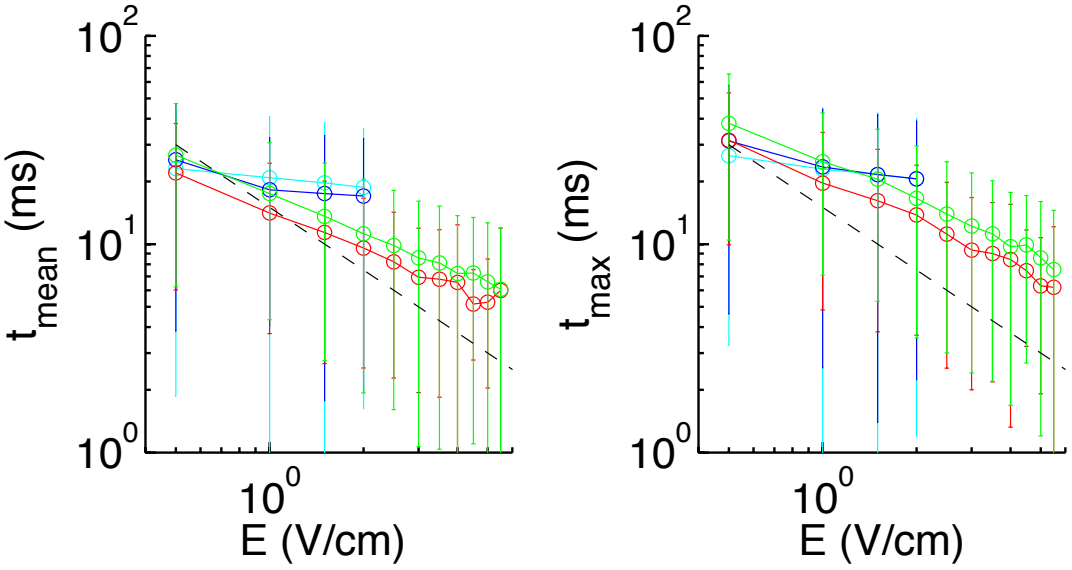

(a) Mean time vs. E.

(b) Maximum time vs. E.

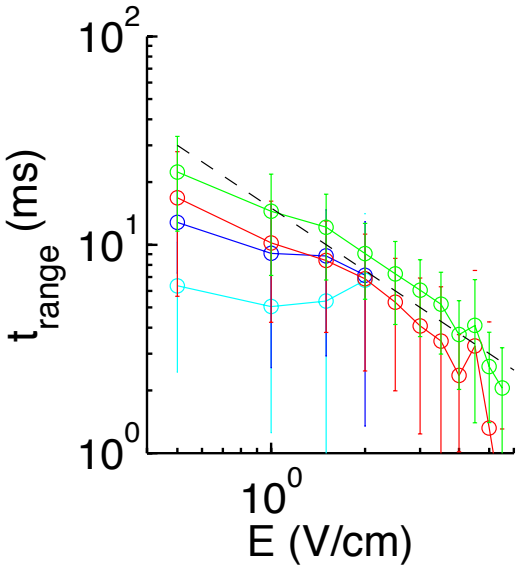

(c) Time range vs. E.

Figure 4.8: Activation times vs. electric field strength E for canine endocardium (cyan), canine epicardium (blue), rabbit LV (red) and rabbit RV (green). Data are from figures 4.3, 4.4, 4.1 and 4.2, respectively. Error bars are the standard error of the mean. The dashed line has slope -1 to guide the eye.

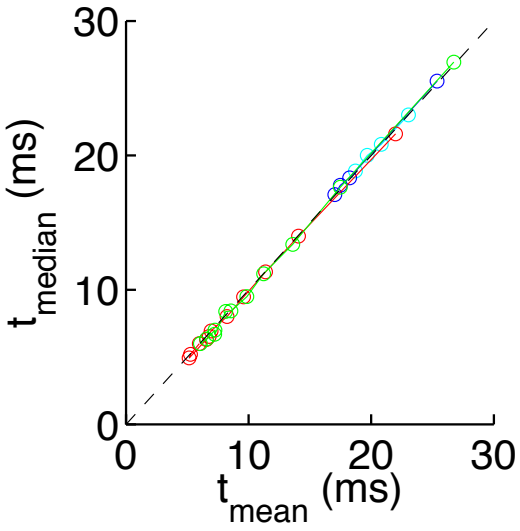

Figure 4.9: Comparison of median and mean activation times, parameterized by E, for canine endocardium (cyan), canine epicardium (blue), rabbit LV (red) and rabbit RV (green). Data plotted are from figure 4.7. A dashed line with slope 1 is drawn to guide the eye in comparing abscissa and ordinate.

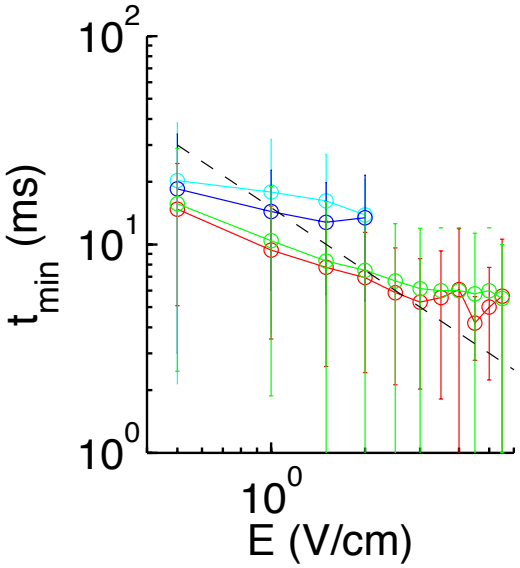

Figure 4.10: Minimum activation time vs. electric field strength E for canine endocardium (cyan), canine epicardium (blue), rabbit LV (red) and rabbit RV (green). Data are from figures 4.1, 4.2, 4.3 and 4.4, respectively. Error bars are the standard error of the mean. The dashed line has slope -1 to guide the eye.

4.3.5 Onset time

Figure 4.10 shows the time between the electric field pulse and the first optical action potential in the ROI, which we defined as the onset time t_{min}. In rabbit hearts, the time to the first surface action potential at the threshold field strength ($E = 0.3$ V/cm) was in the range 22–26 milliseconds, 5–6 times longer than the pulse itself. Such a long onset time clearly could not be due to delayed wave emission, else it should have been visible within the 4 ms duration time of the pulse. Therefore, assuming this delay was due to the finite time required for the action potential to propagate towards the epicardium, we can estimate the distance the wave must have travelled to be $v_c/t = (0.05\ \text{cm/ms}) \cdot (24\ \text{ms}) = 1.2$ cm. The walls of the rabbit heart are no more than 5 mm thick, so we cannot explain this delay by proposing that the excitation occurred on the endocardium and travelled outwards towards the epicardium. The only structure that is more than 1 cm from the epicardium is the ventricular septum (the heart muscle wall that separates the right and left ventricles, and through which bundle branches conduct action potentials from the atria to the apex of the heart). The activation patterns at low field strengths (see figures 4.1 and 4.2) looked remarkably similar to the normal activation patterns during sinus rhythm. This suggests that the atrioventricular node and/or the bundle branch conduction system may be involved. These structures are not particularly large so we would not expect them to be recruited first. However, if their excitation threshold ΔV_m were lower than for other ventricular cardiomyocytes, then they would be recruited at lower E. The length of the septum L_{septum} from base to apex is 3 cm and the conduction velocity in specialized conduction fibers v_c^{spec} is approximately 1.5 m/s, three times that of regular cardiomyocytes [83]. The expected delay between the onset of the electric field pulse and the first visible epicardial action potential is thus

$$\frac{L_{septum}}{v_c^{spec}} \approx \frac{30\ \text{mm}}{1.5\ \text{mm/ms}} = 20\ \text{ms}, \tag{4.2}$$

consistent with our measurements of t_{min} plotted in figure 4.10.

The theory of wave emission from heterogeneities was only developed for heterogeneities within excitable tissue but a similar effect should hold at tissue boundaries wherever the surface normal vector has a component in the direction of the electric field. Thus structures such as the trabecular muscle fibers on the endocardium may also be activated at low fields due to their large size (greater than 1 mm in radius). Supposing activation to have occurred from the large trabeculae near the apex, how long before this activation would reach the endocardium?

The thickness of the ventricle wall near the apex in rabbits is approximately 3 mm. The transmural wave propagation velocity is no more than half the velocity along muscle fibers. Thus, we take $v_c^{transmural} = 0.25$ m/s. Together, these values give an expected delay of

$$\frac{L_{transmural}}{v_c^{transmural}} \approx \frac{3 \text{ mm}}{0.25 \text{ mm/ms}} = 4 \text{ ms}, \tag{4.3}$$

which is much smaller than required to explain the results in figure 4.10.

4.3.6 Two mechanisms for faster excitation

We also studied the fraction of the tissue surface activated after each pulse as a function of time (or, equivalently, the distribution of activation times). In figures 4.3 and 4.4, we plotted the normalized distribution of activation times $\dot{S}(t)$ and its integral $S(t)$ for field strengths $E = 0.5$–2 V/cm. At low field strengths, the activated tissue fraction $S(t)$ is a broad and low distribution that gradually narrows and becomes more peaked as E increases. This is quantitatively captured by σ, the second moment of $\dot{S}$, shown in figure 4.7, which is seen to decrease as E increases. The gradual decrease in σ with increasing E points to a continuous distribution of heterogeneity sizes (as opposed to a discontinuous, step-like distribution).

We have already established that t_{max} decreases with increasing E. However this still leaves open the question of *how* the activated fraction $S(t)$ changes as E increases.

Specifically, how does t_{min} change with increasing E? Bearing in mind what we have established so far about the dependence of $S(t)$ on E, we find that S can change in one of two ways: (1) it can shift leftwards towards shorter activation times while keeping its shape, such that t_{min}, t_{mean} and t_{max} decrease together while t_{range} and σ remain constant, as E increases, or (2) it can stretch upwards, rising more steeply, such that t_{min} remains constant while t_{max}, t_{range} and σ decrease and t_{mean} decreases at half the rate of t_{max}.

The first hypothesis—that S and $\dot{S}$ translate uniformly to shorter times—would imply that the number of sources N (or the density ϱ) remains constant as E increases but these sources are activated earlier or closer to the surface (the latter would imply that the wave sources cannot be of anatomical origin). The second hypothesis—that $\dot{S}$ becomes narrower and more peaked and that S scales down in time—would imply that the number of sources N increases with increasing pulse strength E.

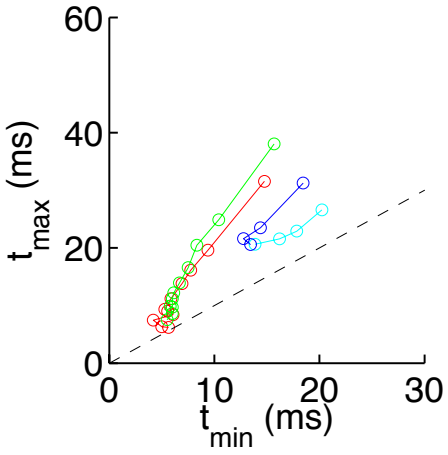

Figure 4.11: Comparison of t_{max} and t_{min}, parameterized by E, for canine endocardium (cyan), canine epicardium (blue), rabbit LV (red) and rabbit RV (green). A dashed line with slope 1 is drawn to guide the eye.

These two hypotheses are easily distinguished by comparing the behaviour of $t_{max}(E)$ with that of $t_{min}(E)$. If $t_{max}(E)$ and $t_{min}(E)$ decrease at the same rate, then we would have to conclude that N remains constant with increasing E; otherwise, we would conclude that the number of sources N is a function of E. We plotted t_{max} against t_{min} in figure 4.11.

Comparing their relationship to the reference line with slope 1, we can conclude that N is indeed a function of E: increasing field strength recruits additional wave sources in cardiac tissue. Furthermore, the rabbit heart data presented in figures 4.8 clearly favour the second hypothesis. The canine data are, unfortunately, ambiguous.

4.3.7 Linking dynamics with structure

As mentioned in chapter 3, it is not currently possible to access the electrical wave dynamics inside bulk heart tissue. The more sites are activated by the electric field pulse, the shorter the distance each activation wave travels before it encounters another wave. Therefore, we expect the activation times to decrease as the electric field pulse strength is increased.

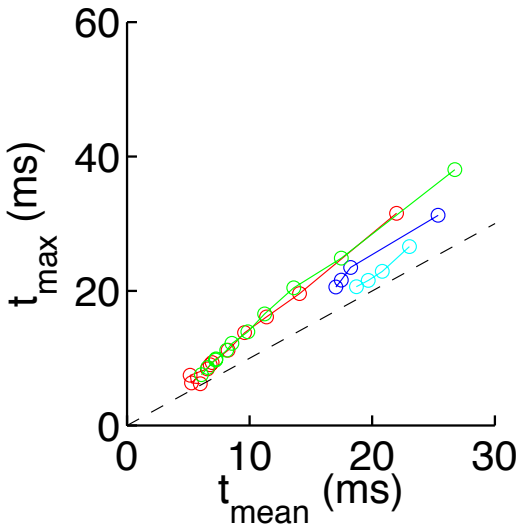

Figure 4.12: Comparison of t_{max} and t_{mean}, parameterized by E, for canine endocardium (cyan), canine epicardium (blue), rabbit LV (red) and rabbit RV (green). A dashed line with slope 1 is drawn to guide the eye.

We had stated in section 3.2.2 that $t_{max} \propto t_{mean}$. Figure 4.12 confirms that this is indeed the case, with the exception of one data point from the canine endocardium. We are thus confident in our use of t_{mean}, which is less sensitive to outliers, instead of t_{max} for

linking structure and dynamics. Table 4.1 gives the scaling exponents β extracted from a linear least-squares fit to $\log_{10}(t_{mean})$ vs. $\log_{10}(E)$ in the 4 preparations we studied, as well as the size distribution exponent b measured from microCT scans. Together, they give an estimate of the aspect ratio exponent γ, which is the inverse of the effective dimension of the system d. The rabbit preparations have $\gamma \approx 0.6$, which puts them in the regime between a 1d and a 3d system, with a transition point N_+^* that depends on the density of sources.

The relatively flat scaling of canine activation time t_{mean} gives wildly wrong estimates of the aspect ratio exponent, which should lie in the range $1/3$ to 1. There is no good explanation for this, because we have already seen that the number of breakthrough sites in the canine ventricle grows with field strength. The experiments should be repeated with measurements taken at higher field strengths.

Table 4.1: Aspect ratio exponent γ estimated from measurements of the activation time scaling exponent β ($t_{mean} \propto E^{-\beta}$) and from the size distribution scaling exponent ($p \propto R^{-b}$).

Tissue Preparation			β	b	$\gamma = \beta(b-1)$	$d = 1/\gamma$
Rabbit	LV	epi	0.52 ± 0.04	2.13	0.59	1.7
	RV	epi	0.57 ± 0.02		0.64	1.6
Canine	RV	epi	0.17 ± 0.06	1.80	0.14	7.4
	RV	endo	0.148 ± 0.004		0.118	8.47

Combining equation 3.8, which relates E to R, with the heterogeneity size distribution $\varrho(R)$ from figure 1.5, we computed the size distribution of heterogeneities $p(E)$ as a function of E, which we plot in figure 4.13(a). Integrating this distribution gives a density $\varrho_{optical}$ which we plot alongside the density measured from microCT scans, $\varrho_{structure}$ in figure 4.13(b). Because the structure measurements are only relative quantities, there is a free multiplicative factor that we adjusted so that the curves would overlap. The fact that the curves agree over much of the range suggests that the inhomogeneities picked

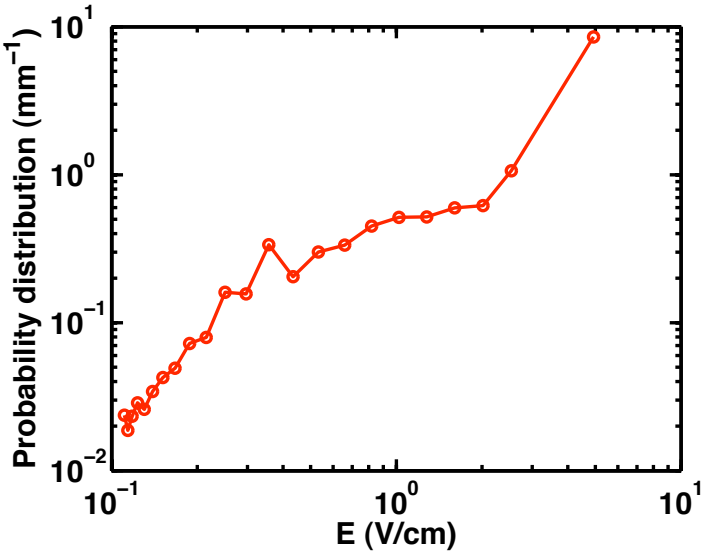

(a)

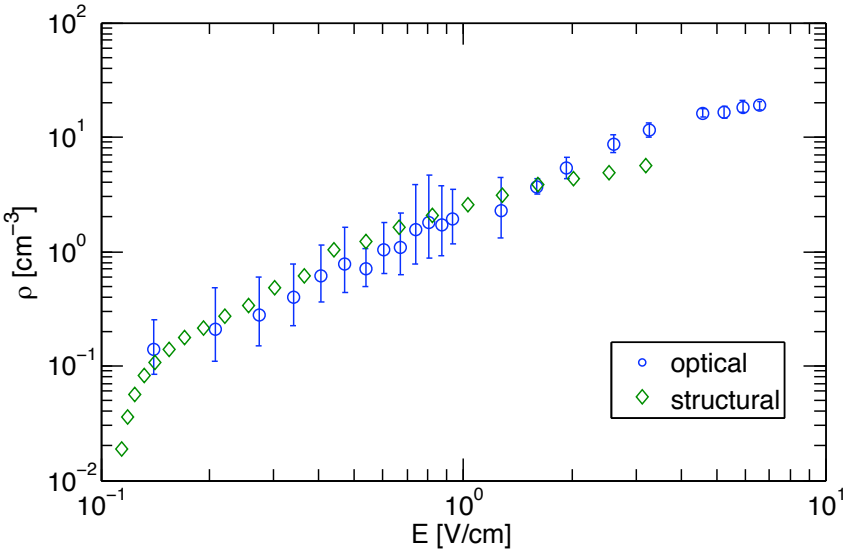

(b)

Figure 4.13: **Heterogeneity and WES density as functions of field strength.**
(a) Probability density $p(E)$ obtained by combining rabbit size distribution $p(R)$ (see figure 1.5) with equation 3.8.
(b) WES density $\varrho(E)$ (blue) from activation maps and (green) from a combination of WEH theory and structure measurements. Error bars are the standard deviation of the mean.

up by the microCT scan, when combined with our simple theoretical model, are enough to explain the measured activation dynamics.

4.4 Application

In the last two chapters, we have gained a more quantitative understanding of the activation dynamics of the heart in response to an external electric field pulse. We wanted to use this understanding to test the proposal made by Pumir *et al.* [2] in 2007 that a pulsed electric field could be used to terminate cardiac chaos with significantly lower pulse energies than are used today for standard defibrillation. Based in part on our unpublished results and methods, Fenton *et al.* [56] have already shown that a pulsed electric field could terminate atrial arrhythmias and gave it the name "Far-Field Anti-Fibrillation Pacing". In the next chapter, we investigate the effectiveness of AFP in terminating ventricular arrhythmias.

CHAPTER 5

TERMINATION OF ARRHYTHMIA

In the closing paragraph of the previous chapter, we noted that wave emission from heterogeneities might open the way to controlling chaos in excitable media. In the context of terminating cardiac arrhythmias, this hypothesis was first tested in computer models and in cardiac cell culture preparations by Pumir *et al.* in 2007 [2]. They wrote that "... wave emission from heterogeneities (WEH) opens a way for a multisite pacing that was not possible with conventional methods" and that "only experiments with real hearts can precisely determine the gains in energy." [2] As mentioned in the introductory chapter of this thesis, Fenton *et al*. [56] later tested multisite pacing in canine atria preparations and found an 87% reduction in the pulse energy required to terminate atrial fibrillation compared to standard defibrillation.

In this chapter, we investigate the gains in energy of WEH as a means of multisite pacing for the termination of cardiac arrhythmias. Our approach was to compare the effectiveness of single "defibrillation" pulses against a sequence of "Far-Field Pacing" (AFP) pulses. AFP is similar to anti-tachycardia pacing (ATP) except that instead of a single pacing electrode, it uses far-field electrodes to deliver a homogeneous external current to the whole tissue. We compared the efficacy of AFP and standard defibrillation in terminating VF in two experimental preparations: canine right ventricles and whole rabbit hearts. Details on the methods, equipment and protocols can be found in chapter 2.

Figure 5.1: **Example of successful termination of ventricular fibrillation (8 Hz) in canine RV.**

(a) Optical maps during ventricular fibrillation (VF), Far Field Pacing (AFP) and normal rhythm (NR). Areas with optical signals 40–100% of the maximum action potential amplitude (APA) are colored red-yellow-white.
(upper box) Complex spatio-temporal wave propagation (fibrillation) on endocardial and epicardial surfaces preceding control by 8 low-energy pulses (AFP).
(lower box) Selected AFP pulses (1.6 V/cm, 113 ms period, 5 ms duration) and subsequent normal rhythm (NR) on endocardial and epicardial surfaces. Panels labeled "pulse N" were taken 30 ms after the N^{th} AFP pulse.

(b,c) The fraction of excited (b) endocardial and (c) epicardial tissue as a function of time. $S(t)$ is plotted above and its derivative dS/dt below. Red tick marks indicate the times at which AFP pulses were delivered. Fibrillation hovered around $S = 0.36 \pm 0.16$ (mean and standard deviation) while AFP pulses consistently excited most of the tissue, $S > 0.7$, until total capture on both epi- and endocardium was accomplished.

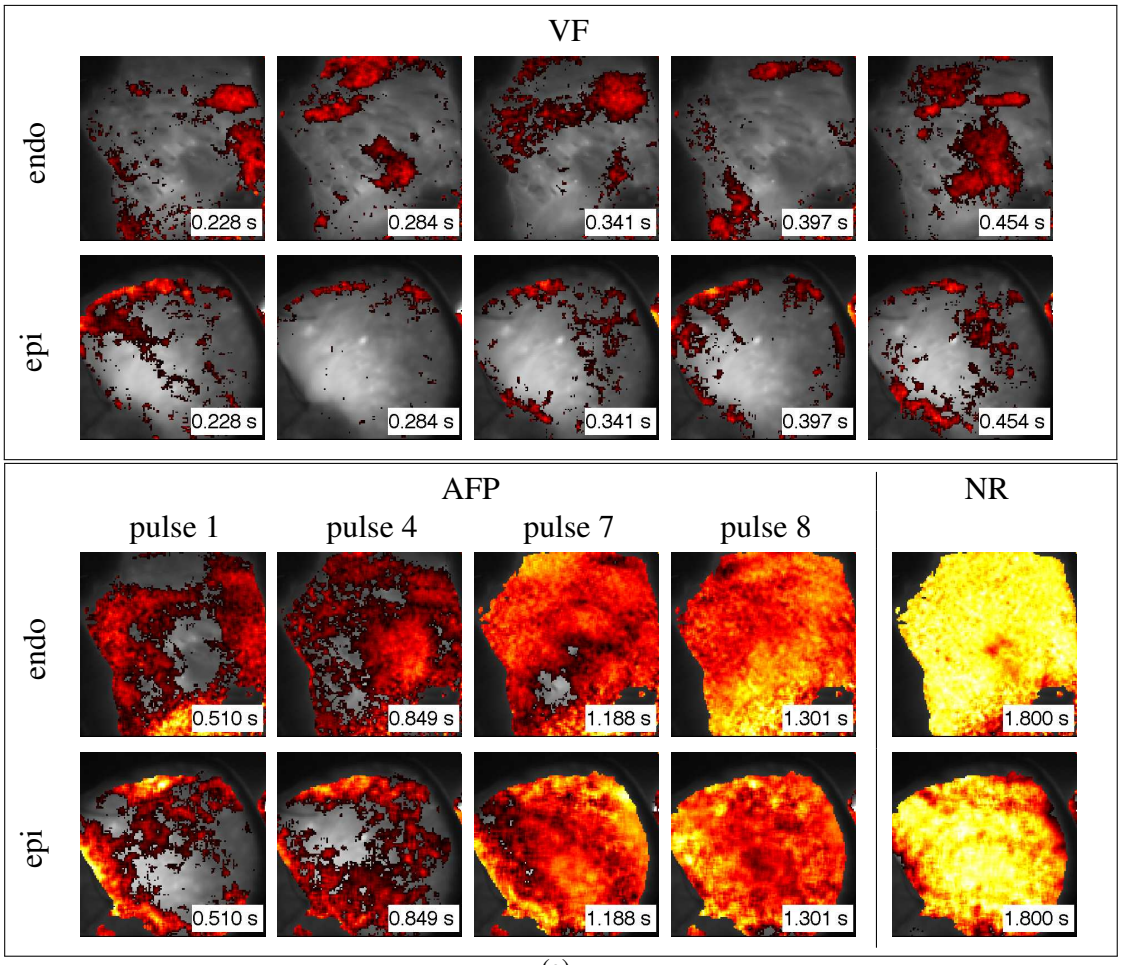

(a)

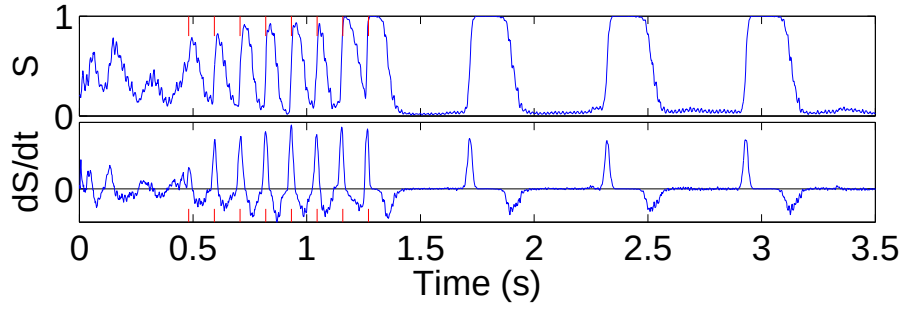

(b) Fraction of excited endocardial tissue.

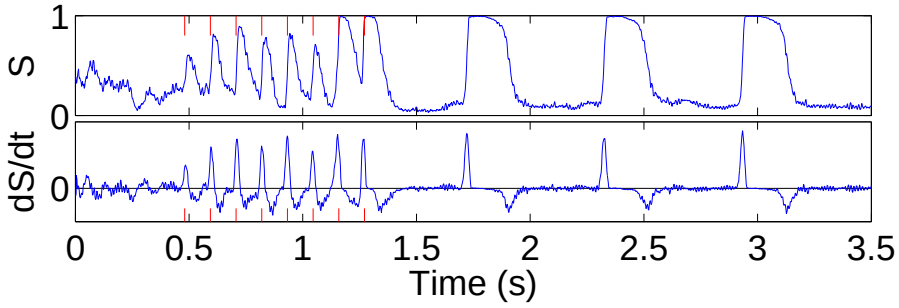

(c) Fraction of excited epicardial tissue.

5.1 AFP results in canine ventricle preparations

5.1.1 Successful termination of VF

An example of successful termination of VF in the canine right ventricle is shown in figure 5.1. Fast sustained arrhythmia (with dominant frequency 8 Hz) was induced in an arterially cannulated and perfused canine right ventricle preparation.[1] Ten seconds after inducing VF (to ensure the arrhythmia was sustained), AFP was applied with a period 10% shorter than the dominant VF period. The dominant period was selected as the peak of the real-time power spectrum (over a one-second window) of a single pixel's optical signal. The pulse energy was 25% of the standard defibrillation pulse energy for this preparation (see figure 5.2).

Figure 5.1(a) shows how AFP terminated an episode of VF. The dominant period of the arrhythmia was 125 ms. Eight rectangular, monophasic, 5 ms duration far-field pulses with $E = 1.6$ V/cm were applied with period 113 ms (10% shorter than the dominant period).

The fibrillatory activation pattern visible in the upper set of images of panel (a) gives way to increasingly synchronized activation patterns during AFP.[2] This synchronization is evidenced by the large areas of yellow/red activated tissue seen in the first four panels of the lower set of images (labeled "pulse 1", "pulse 4", "pulse 7" and "pulse 8"). AFP here resulted in termination of VF and return to a normal rhythm (NR) with frequency 1 Hz, shown in the last image of panel (a). The fact that the tissue is nearly uniformly yellow in the last panel (1.8 secs) may seem unusual for the plane wave propagation pattern expected during normal rhythm. The wavelength of the action potential is $\lambda = v_c \cdot \text{APD} \approx (0.5 \text{ m/s}) \cdot (0.3 \text{ s}) = 15\text{cm}$. This is twice as long as the size of the

[1] See section 2.3 on page 32 for more details on the experimental methods.

[2] Note that fibrillatory activity is not well seen in the epicardial images because the signal-to-noise ratio in these recordings was lower than in the endocardial recordings and the amplitude of optical action potentials during fibrillation is about one-third of the amplitude during normal sinus rhythm.

tissue preparation, 8 cm, so that one expects the entire tissue to be activated at the same time. Panels 5.1(b) and 5.1(c) quantify these qualitative observations. The data shown in figure 5.1(a) suggested that the fraction of excited tissue grew substantially during AFP. We quantified this observation by computing the excited tissue fraction $S(t)$,[3] which was just the fraction of surface with optical signal greater than half the maximum amplitude at time t. The results are plotted in the top rows of panels 5.1(b) and 5.1(c).

Observation 1. The data suggest that the first pulse alone would not have been sufficient to terminate the arrhythmia: the tissue is not completely excited nor completely refractory, indicating that the fibrillatory activity would continue without further intervention. The unsuccessful example (see figure 5.3) is consistent with this interpretation.

Observation 2. The fact that $S_{endo} = 0.36 \pm 0.16$ during fibrillation implies that fibrillatory wave activity occupies between a fifth and a half of the tissue surface at any time. This suggests that a substantial portion of the tissue is in its resting state. The amount of excited tissue following each AFP pulse is clearly larger than during fibrillation, indicating successful recruitment of wave sources with each pulse. The epicardium showed a non-monotonic increase in $S_{epi,Max}$ following each pulse.

Observation 3. In looking at the activation maps, we observed that successive pulses seemed to excite increasingly larger tissue areas. This was true for the endocardium but not for the epicardium. The mechanism of tissue recruitment is not as straightforward as it appeared (apply more pulses, synchronize more tissue). They also reveal that the minima of S following each pulse fell below the range seen during VF. This is consistent with a mechanism of increasing synchronization of tissue and concomitant reduction in the fraction of fibrillating tissue.

[3]This definition of $S(t)$ is identical to the one given in the previous chapter, although it is expressed differently.

Observation 4. The derivative of the activated fraction, dS/dt, (plotted in panels 5.1(b) and 5.1(c)) characterizes the speed at which tissue is activated.[4] S_{endo} changed slowly ($|dS/dt| < 0.05$) during VF but spiked during AFP, reaching successively larger maxima with each pulse. Thus not only do AFP pulses excite larger tissue areas, they do so with increasing speed. One might be tempted to conclude that this increase in activation speed corresponded to a larger number of WES following each pulse. However we must be careful with interpretation.

We do not expect either the number or the size of anatomical structures to change with E, thus how can the number of WES change? A far-field pulse should only be able to elicit an action potential in non-refractory tissue. Thus an apparent increase in N at constant E could imply a lower fraction of refractory tissue when the pulse was delivered.

Increased recovery from refractoriness indirectly leads to more wave sources even though field strength remains constant: if wave sources that were previously refractory are now excitable, they show up as "new" wave sources. The role of refractoriness and recovery from refractoriness is consistent with the observation that peaks of S are followed by troughs, reflecting the fact that excited tissue must first return to its resting state before it can be re-excited.

Observation 5. Activation was stronger on the endocardium, suggesting that wave-emitting structures were concentrated there. The endocardial surface is covered with a web of large (1–10 mm) muscle bundles whereas the epicardium is smooth. It is thus natural that we would see more activation on the endocardium than on the epicardium at lower E.

[4] If S is the area of activated tissue "islands", dS/dt is the length of the island shorelines.

Taken together, these 5 observations are more consistent with a synchronization mechanism characterized by gradual filling of the excitable gap[5]. Under this hypothesis, each AFP pulse has a chance of terminating the arrhythmia by recruiting a critical mass of tissue, which we estimate at over 90%. This is consistent with previous studies that showed that sustained fibrillation requires a critical mass of tissue [25]. The mechanism of AFP is perhaps as follows: by recruiting tissue and rendering it refractory, AFP deprives fibrillation of the tissue mass it requires to sustain itself.

5.1.2 Standard defibrillation

We want to compare the mechanism of VF termination via AFP to that of termination via standard defibrillation. Figure 5.2 shows an example of the latter. The tissue preparation is identical to the one shown in the previous section, and the respective episodes of VF were induced and terminated less than 10 minutes apart.[6]

The defibrillation pulse strength in this example was 3.8 V/cm, 2.4 times higher than for the AFP example of the previous section. At this field strength, only one pulse was needed to excite the entire tissue. There is some indication that the timing of the pulse may have been fortuitous: $S(t) = 0.8$ just before the pulse was delivered. Thus, the pulse only had to excite the remaining 20% of the tissue to achieve complete synchronization.

5.1.3 Unsuccessful termination of VF

To better understand what is necessary for successful termination of VF via AFP, we also examined an example of unsuccessful termination (figure 5.3). This termination attempt, during the same episode of fibrillation, on the same preparation, was made 22

[5]The *excitable gap* is the portion of tissue that has recovered from refractoriness and has not yet been excited. Advancing wavefronts reach a critical threshold if the excitable gap shrinks to zero: if the waves propagate any faster, they will encounter conduction block against the waveback in front of them.

[6]See footnote 2 on page 100.

Figure 5.2: **Example of successful defibrillation in canine RV.**

(a) Optical maps during ventricular fibrillation (VF), Far Field Pacing (AFP) and normal rhythm (NR). Areas with optical signals 40–100% of the maximum action potential amplitude (APA) are colored red-yellow-white.
(upper box) Complex spatio-temporal wave propagation (fibrillation) on the endocardial surface preceding control by a single standard defibrillation pulse. The epicardial activity is not shown because it adds no new information.
(lower box) Defibrillation pulse (3.8 V/cm, rectangular, monophasic, 5 ms duration) and subsequent normal rhythm (NR). Panel labeled "Defib" was taken 30 ms after the defibrillation pulse.

(b) The fraction of excited endocardial tissue as a function of time. $S(t)$ is plotted above and its derivative dS/dt below. Red tick mark indicates the time at which the defibrillation pulse was delivered. Fibrillation hovered around $S = 0.36 \pm 0.16$ (mean and standard deviation).

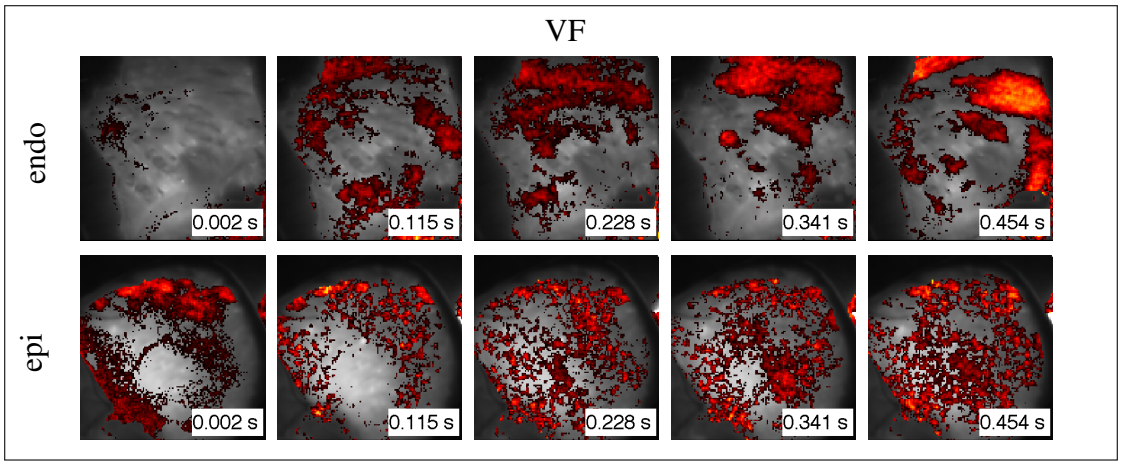

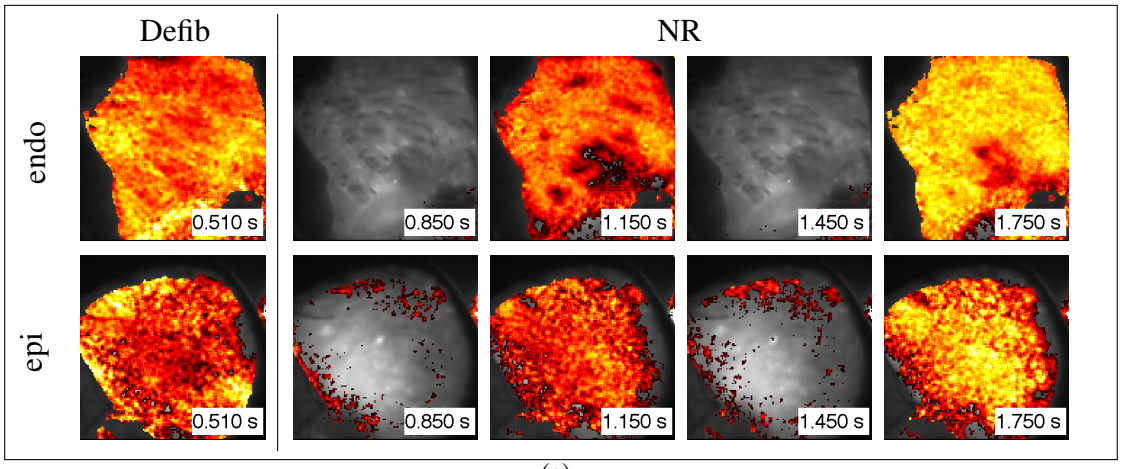

(a)

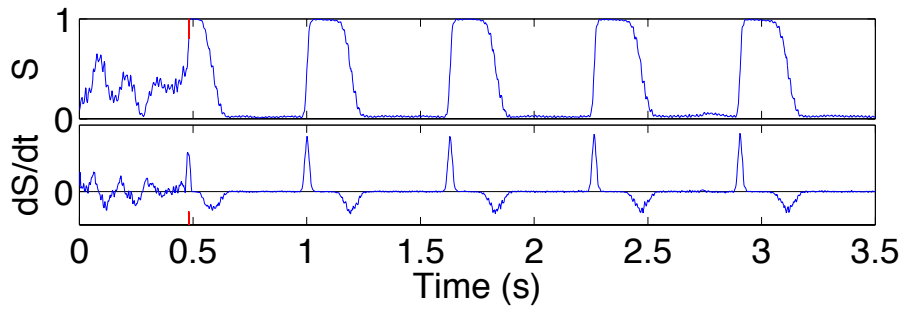

(b) Fraction of excited endocardial tissue.

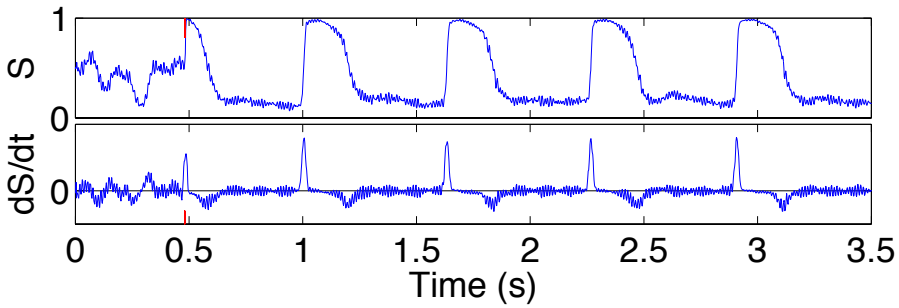

(c) Fraction of excited epicardial tissue.

seconds before the case discussed in section 5.1.1.[7] All parameters were identical (field strength, pacing period, number of pulses, pulse duration). The dominant period was also 8 Hz.

During the experiment, the two cases appeared similar in every measurable respect, yet the outcomes were very different: one remained in spatiotemporal chaos while the other successfully made the transition to the global resting state. This raises two hypotheses: either termination of fibrillation via AFP is inherently probabilistic or, which is more likely, it depends on parameters we have not yet identified.

Can we identify what distinguished these two cases from one another so as to explain their different outcomes? Consider the activated fraction $S(t)$: S_{endo} looked similar in both the successful and unsuccessful cases, but S_{epi} remained below 0.8 in the unsuccessful case whereas it reached 1 in the successful case (compare panels 5.1(b) and 5.3(b)). Thus it appears that the AFP sequence failed to recruit enough of the epicardial tissue to terminate VF.

5.1.4 Energy reduction via AFP in canine experiments

In total, we terminated 38 episodes of VF in 7 canine ventricle preparations. Of these 38 episodes, 28 were terminated via AFP and 10 via standard single pulse defibrillation. For each preparation, we computed the ratio of the average defibrillation pulse energy and the average AFP pulse energy. The results are shown in figure 5.4. On average, AFP reduced the pulse energy by a factor of 5 and in some cases by a factor of more than 50. While the pulse energy was reduced by 80%, the total energy used to terminate VF was not decreased relative to standard single pulse defibrillation due to the 5–10 pulses needed at the lower energies.

[7] See footnote 2 on page 100.

Figure 5.3: **Example of unsuccessful termination of ventricular fibrillation (8 Hz) in canine RV.**

(a) Optical maps during ventricular fibrillation (VF), Far Field Pacing (AFP) and normal rhythm (NR). Areas with optical signals 35–100% of the maximum action potential amplitude (APA) are colored red-yellow-white (absence of yellow and white indicates that action potentials were less than 60% of maximum APA).
(upper box) Complex spatio-temporal wave propagation (fibrillation) on endocardial and epicardial surfaces preceding 8 low-energy pulses (AFP).
(lower box) Selected AFP pulses (1.6 V/cm, 113 ms period, 5 ms duration) and subsequent fibrillation. Panels labeled "pulse N" were taken 30 ms after the N^{th} AFP pulse.

(b,c) The fraction of excited (b) endocardial and (c) epicardial tissue. $S(t)$ is plotted above and its derivative dS/dt below. Red tick marks indicate the times at which AFP pulses were delivered. Fibrillation hovered around $S_{endo} = 0.32 \pm 0.13$ (mean and standard deviation) while AFP pulses consistently excited most of the tissue, $S_{endo} > 0.7$. dS/dt shows that the AFP pulses excited large areas of tissue faster than during VF (compare AFP pulses), yet this was not sufficient.

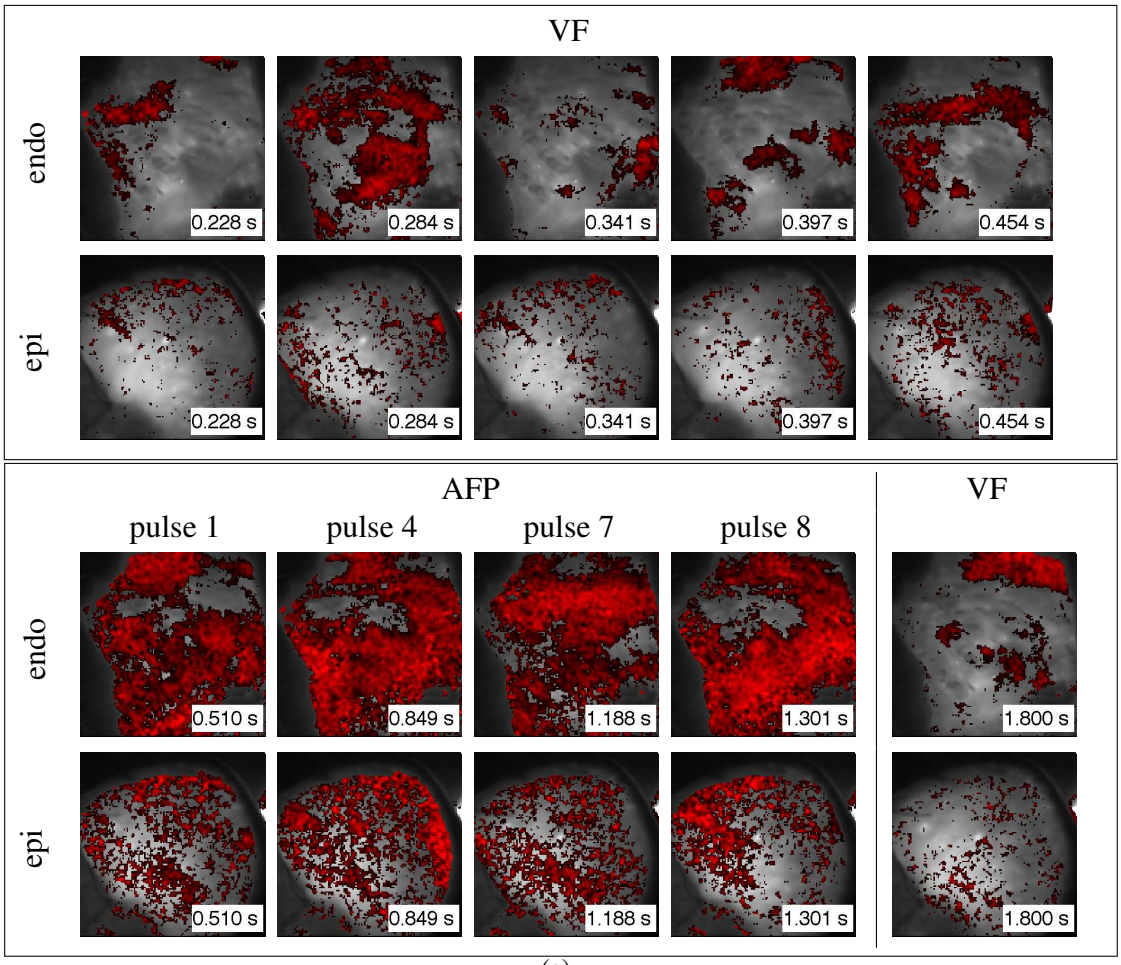

(a)

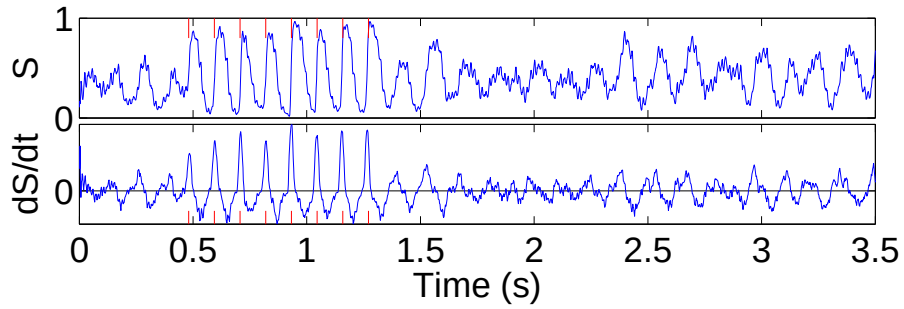

(b) Fraction of excited endocardial tissue.

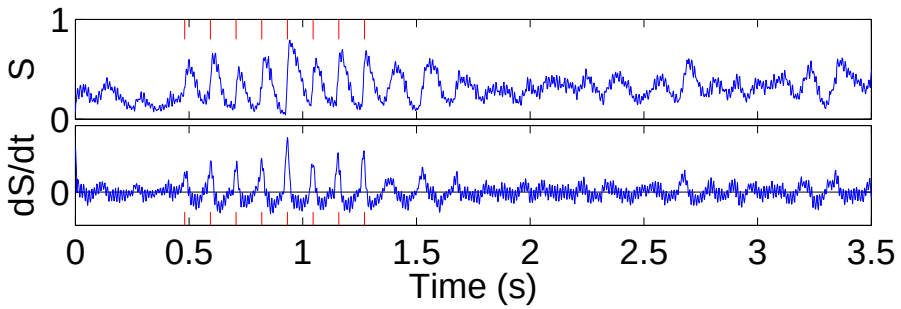

(c) Fraction of excited epicardial tissue.

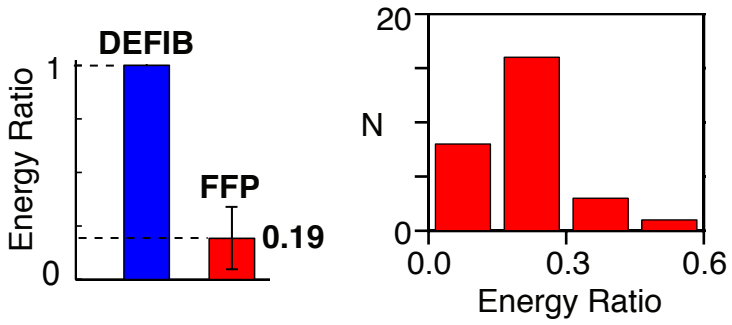

(a) (b)

Figure 5.4: **Statistics of AFP vs. defibrillation in canines.**
(a) Comparison of AFP and standard defibrillation pulse energy needed to terminate ventricular arrhythmias in n = 28 experiments (7 preparations). Vertical axis: pulse energy normalized by the mean of the experimentally-measured standard defibrillation pulse energy. The average pulse energy needed for AFP to terminate arrhythmias was 5.3 times less than the defibrillation energy (p=0.05).
(b) Histogram of the pulse energy of successful AFP interventions (bin width = 0.15) for the same experiments as shown in (a).

5.2 AFP results in whole rabbit hearts

An example of successful termination of VF in the rabbit heart is shown in figure 5.5. Fast sustained arrhythmia (with dominant frequency 13 Hz) was induced in a Langendorf-perfused whole rabbit heart preparation.[8] Thirty seconds after inducing VF (to ensure the arrhythmia was sustained), AFP was applied with a period 10% shorter than the dominant VF period. The dominant period was computed from the highest-powered frequency in the real-time power spectrum (over a 3-second window) of an MAP signal from quadrupolar MAP catheter-style electrodes positioned against the endocardium, near the apex of the heart.

Figure 5.5(a) shows how AFP terminated an episode of VF. The dominant period of the arrhythmia was 110 ms. Eight rectangular, biphasic, 4 ms duration far-field pulses with $E = 5.2$ V/cm were applied with period 70 ms (10% shorter than the dominant period).

In comparison to termination in the canine preparations, the fibrillatory activation pattern visible in the upper set of images of 5.5(a) does not appear to change substantially during AFP (both on the left and right ventricular epicardium). Nevertheless, AFP resulted in termination of VF within a second of the last pulse and return to a normal rhythm (NR) with frequency 1 Hz, shown in the last image of . Panels 5.5(b) and 5.5(c) quantify these qualitative observations. The data shown in figure 5.5(a) suggested that the fraction of excited tissue remained mostly unchanged during AFP. To better understand the sequence of events, we again computed the excited tissue fraction $S(t)$ and plotted it in the top rows of panels 5.5(b) and 5.5(c).

Observation 1. The AFP pulses are not as clearly visible here as they were in figure 5.1, for example, yet the dynamics of S during the far-field pulses (3 to 3.49 s)

[8] See section 2.4 on page 40 for more details on the experimental methods.

Figure 5.5: **Example of successful termination of ventricular fibrillation (13 Hz) in a rabbit heart.**

(a) Optical maps during ventricular fibrillation (VF), Far Field Pacing (AFP) and normal rhythm (NR). Areas with optical signals 40–100% of the maximum action potential amplitude (APA) are colored red-yellow-white. (upper box) Complex spatio-temporal wave propagation (fibrillation) on the LV and the RV preceding control by 8 low-energy pulses (AFP). (lower box) Selected AFP pulses (5.2 V/cm, rectangular, biphasic, 70 ms period, 4 ms duration) and subsequent normal rhythm (NR) on the LV and the RV. Panels labeled "pulse N" were taken 30 ms after the N^{th} AFP pulse.

(b,c) The fraction of excited (b) LV and (c) RV tissue as a function of time. $S(t)$ is plotted above and its derivative dS/dt below. Red tick marks indicate the times at which AFP pulses were delivered.

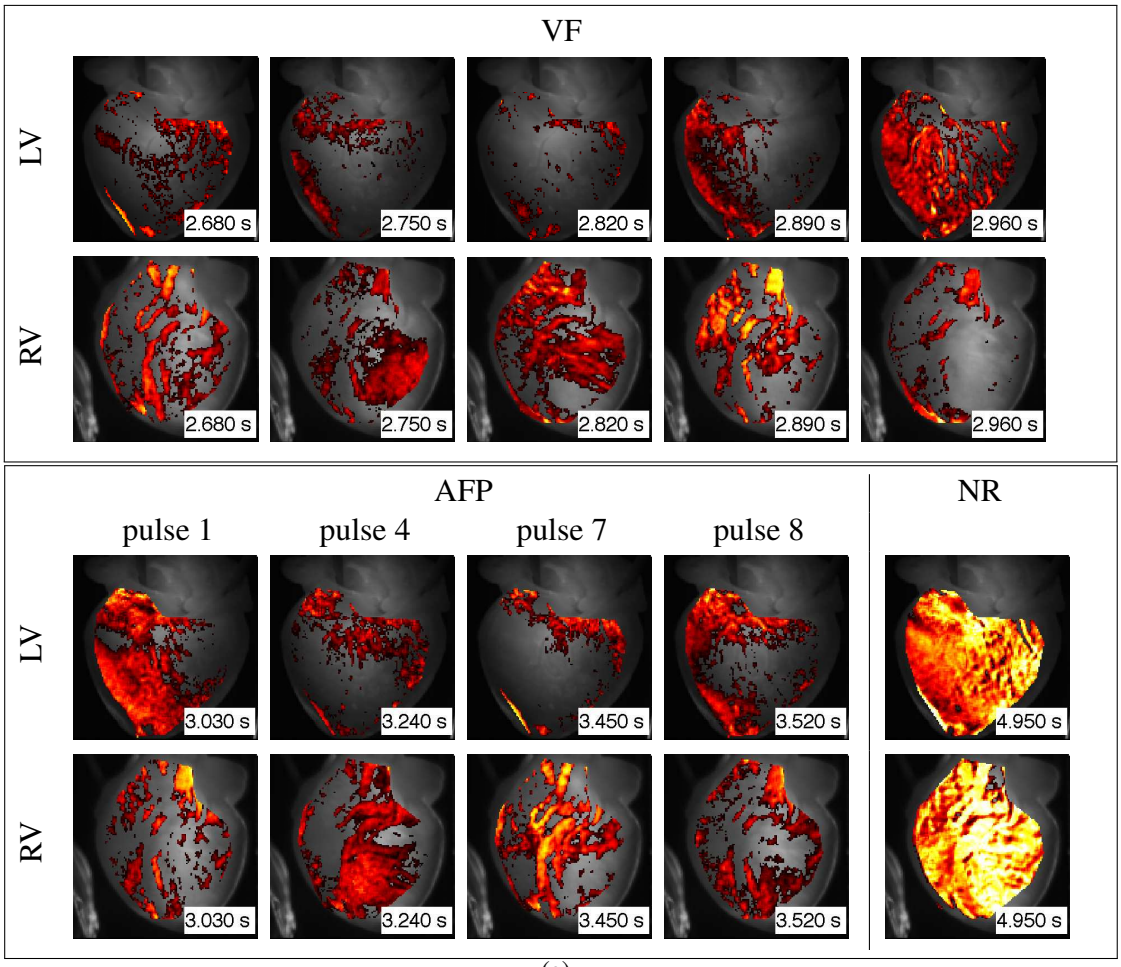

(a)

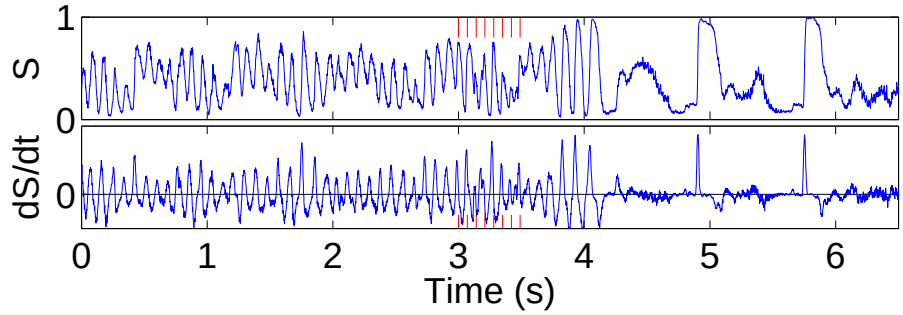

(b) Fraction of excited LV tissue.

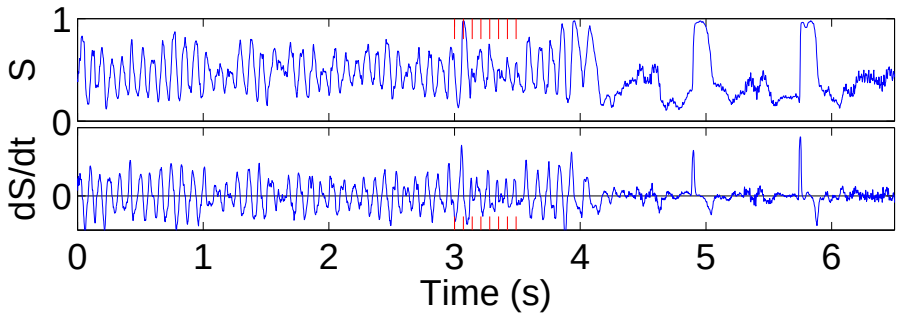

(c) Fraction of excited RV tissue.

seems significantly different from what it was prior to the pulses (before 3 s). This effect is seen both on the LV and on the RV, suggesting that—at this field strength at least—far-field pulses affect the entire heart.

Observation 2. Just as in the canine case, the transition to a normal rhythm is characterized by an increase of the fraction of excited tissue from ~ 0.5 to one over several cycles. This is seen both on the LV *and* on the RV, suggesting that, regardless of species, termination of VF requires complete tissue synchronization.

We induced a total of 80 episodes of fibrillation in 6 rabbit hearts, following the protocol described in 2.4. For each heart, we attempted to terminate VF from far-field electrodes with a standard single defibrillation pulse and with 8-pulse AFP sequences, incrementing the field strength every 1–3 attempts, until the fibrillation was terminated.

Success rate was computed in two ways. First, termination attempt were classified individually as successful or unsuccessful and binned by field strength and number of pulses. This result is plotted in figure 5.7(a). The curve shown a nearly monotonic increase in success rate with increasing field strength for both defibrillation and AFP. This is consistent with previously established results for defibrillation and with a mechanism of increasing recruitment of wave-emitting sources.

Second, success or failure in terminating VF was counted once for each distinct field strength attempted.[9] This provides a complementary picture of the "terminability" of VF as a function of field strength, as shown in figure 5.7(b).

With the exception of one successful defibrillation event at 2.5 V/cm (not shown), termination of VF by defibrillation or AFP was only possible above 5 V/cm. Success rate increased gradually with field strength up to about 9 V/cm and then rose more quickly to nearly 100 % around 11 V/cm. What is striking in these figures is that a

[9]Recall the protocol whereby up to 3 attempts are made at a given field strength, progressively increasing the amplitude until VF is terminated.

Figure 5.6: **Example of successful standard defibrillation of ventricular fibrillation (14 Hz) in a rabbit heart.**

(a) Optical maps during ventricular fibrillation (VF), Far Field Pacing (AFP) and normal rhythm (NR). Areas with optical signals 40–100% of the maximum action potential amplitude (APA) are colored red-yellow-white. (upper box) Complex spatio-temporal wave propagation (fibrillation) on the LV and the RV preceding control by a standard defibrillation pulse.
(lower box) Defibrillation pulse (9.1 V/cm, rectangular, biphasic, 4 ms duration) and subsequent normal rhythm (NR) on the LV and the RV. Panel labeled "Defib" was taken 30 ms after the defibrillation pulse.

(b,c) The fraction of excited (b) LV and (c) RV tissue as a function of time. $S(t)$ is plotted above and its derivative dS/dt below. Red tick marks indicate the time at which the defibrillation pulse was delivered.

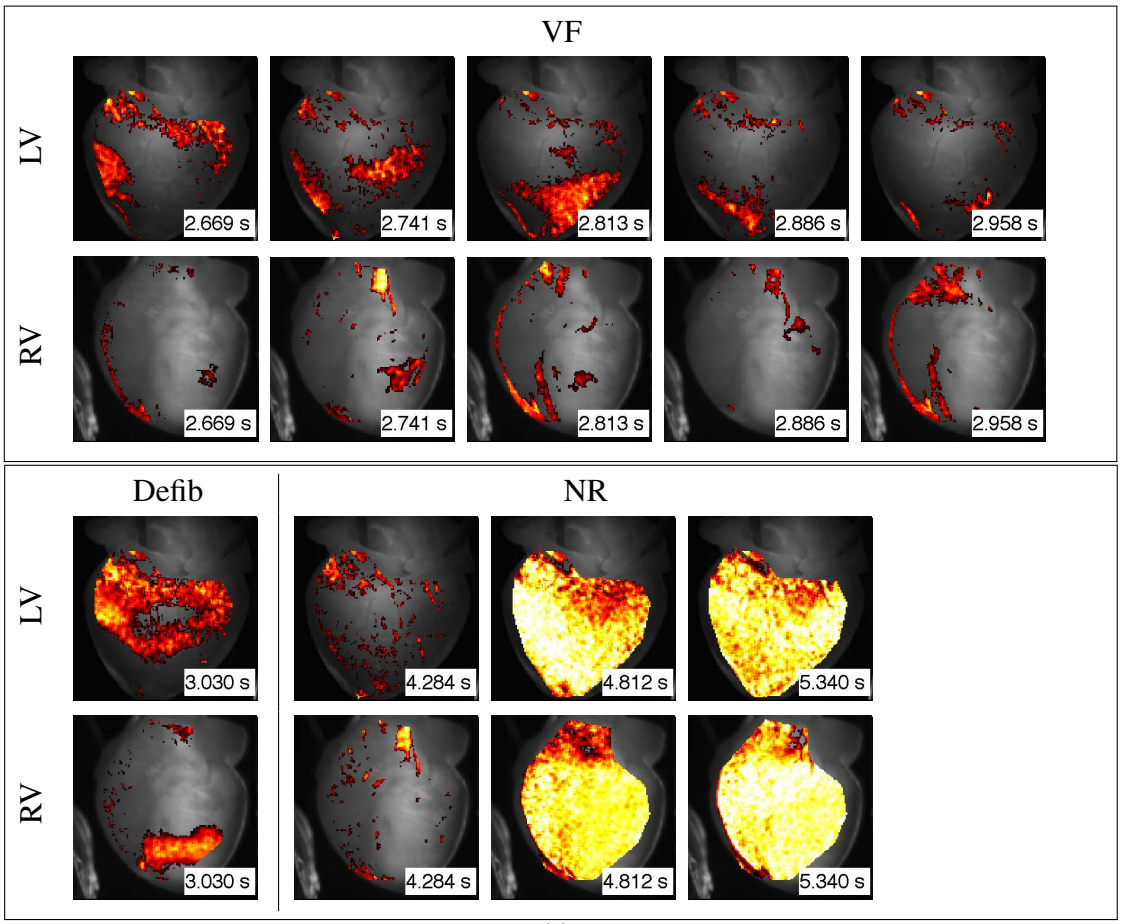

(a)

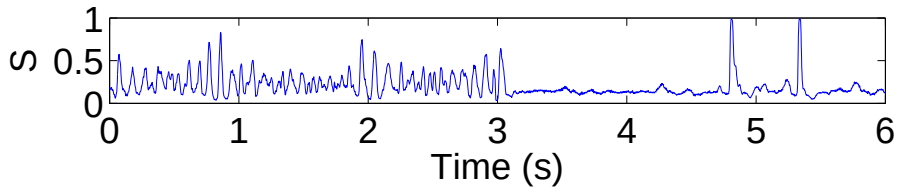

(b) Wavefront fraction of excited LV tissue.

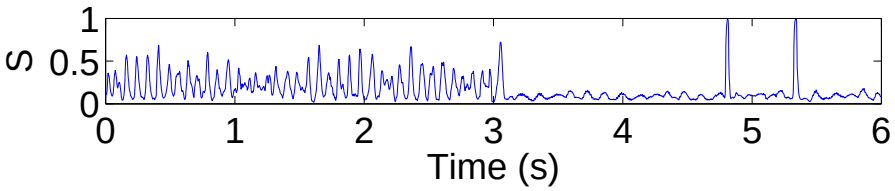

(c) Wavefront fraction of excited RV tissue.

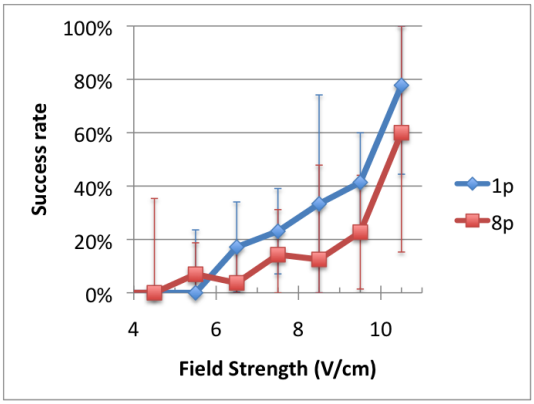

(a) Percentage of successful VF termination attemps vs. pulse field strength (bin width = 1 V/cm).

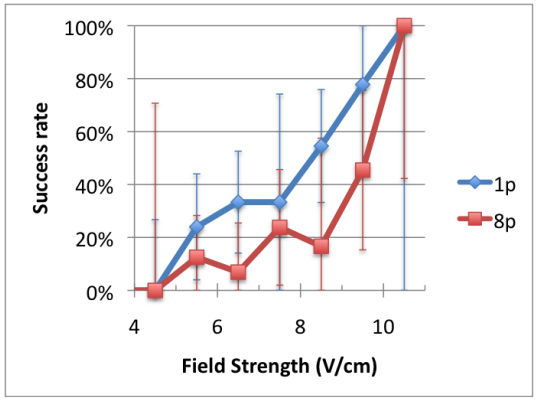

(b) Percentage of VF episodes successfully terminated vs. pulse field strength (bin width = 1 V/cm).

Figure 5.7: Success rates for standard defibrillation and for AFP pulses (in blue and red, respectively). All pulses were biphasic and 4 ms duration.

single pulse was more successful than AFP *at all field strenghts*. This result contradicts the hypothesis that AFP would reduce the pulse amplitude required to terminate VF. It is also contrary to the results obtained in canine preparations (see figure 5.4).

One might be tempted to explain this by claiming that larger field strengths are required to recruit comparable structures in the rabbit heart than in the canine heart. This would appear logical since the rabbit heart is smaller than the canine heart and all matching anatomical structures, such as trabeculae and major coronary arteries are likewise smaller. This would explain the higher field strengths needed to terminate fibrillation in rabbit hearts. However, our experiments on activation dynamics (see previous chapter) clearly showed the same gradual decrease in activation time in both canine and rabbit preparations (see figure 4.9), compatible with the recruitment of an increasing number of wave-emitting sources at *all* field strengths. This observation suggests with the small structure hypothesis, which we thus reject.

One might then hypothesize that the *sequence* of pulses first terminated and then re-induced fibrillation. The increased probability of termination with increasing field strength would have to be offset by an even larger increase in the probability of re-

inducing fibrillation. Were this the case, we expect we would have seen it also in the canine experiments. Since we did not see such an effect in the canine, this explanation seems unlikely.

5.3 Reduced Excitability during Ischemia

AFP in canine ventricle preparations showed an 81% reduction in pulse energy compared to standard defibrillation. However, we were surprised to discover that AFP was much less effective in rabbit hearts: the 8-pulse sequence was no more successful than a single pulse *at all energies*. Why might this be? In each experiment, both the heart tissue, and thus the anatomy, as well as the field strength were the same, so the potential WES were identical. It seems more likely, therefore, that the wave dynamics were somehow different.

Two plausible hypotheses are that (1) ischemia reduced the excitability of the rabbit hearts during fibrillation and (2) that ischemia gave rise to focal arrhythmias rather than reentrant arrhythmias.[10] Whereas AFP is suited to terminating reentrant arrhythmias, where the activity is sustained by rotating spiral waves, it is entirely ineffective against focal arrhythmias, which are sustained y abnormalities in automaticity[11] [86].

Ischemia is a disruption in blood flow which leads to oxygen deprivation in the affected areas. During ischemia, ATP (adenosine triphosphate), the cell's energy currency, cannot be produced in large enough quantities because without a fresh supply of oxygen only anaerobic metabolism is available. ATP-driven ion pumps in the cell membrane stop working as ATP stores are depleted and the ion gradients that they maintained—gradients necessary for normal electrophysiological function—begin to decay[87].

[10] These hypotheses will be tested in upcoming experiments (see section 6.3).

[11] Automaticity is a property of cells whereby they automatically generate action potentials at periodic intervals with no outside influence.

Global no-flow ischemia is known to produce a gradual rise in extracellular potassium concentration $[K^+]_o$ of 1 mM/min up to ≈15 mM in the first 10 minutes in perfused rabbit septum preparations [88, 89]. With the 5–7 minute ischemia protocol we used, the extracellular potassium concentration would thus have risen 2 to 3-fold to $[K^+]_o \approx$ 10–12 mM. Figure 3 of reference [88] shows that $[K^+]_o$ recovers to its normal value within 2–3 minutes of reperfusion from the same high $[K^+]_o$. Thus our protocol should have been sufficient to allow the heart to recover between ischemic episodes.

Ischemia is known to lower excitability and promote focal source arrhythmias [90]. Both of these effects play against AFP: lower excitability implies a larger ΔV_m, which means a larger field strength is required to recruit a WES. Focal source arrhythmias are sustained not by the pattern of activation itself (viz. spiral waves), as in reentrant arrhythmias, but by a pathology at the level of the cell. The mechanism of terminating VF that we are pursuing aims at eliminating spiral waves and is thus ineffective against focal arrhythmias.

In addition, ischemia lowers conduction velocity and action potential duration, thus shortening the wavelength of the action potential [91]. Shorter wavelengths mean a higher maximum density of spiral waves and thus more complex activity during VF. This is in fact why we used ischemia to begin with: to induce sustained fibrillation

CHAPTER 6

CONCLUSION

In chapters 3 and 4, we studied the physics of wave emission from heterogeneities in excitable media and investigated this phenomenon in cardiac tissue preparations. The high space resolution, time-resolved recordings of action potential wave dynamics revealed that induced wave emission in the canine heart starts with electric fields as low as 0.2 V/cm. We found that the number of conductivity heterogeneities (in both canine and rabbit hearts) recruited as wave sources in the heart can be adjusted by increasing or lowering the strength of the electric field, and that the number scales with strength of the applied electric field.

The activated fraction $S(t)$ reduced the information contained in the activation maps into a form easily amenable to modeling, which allowed us to distinguish between two mechanisms by which the activation times get shorter. In both canine and rabbit hearts, the reduction in the activation times occurs due to a narrowing of the distribution of activation times rather than a uniform shift to earlier times, except perhaps in the rabbit heart where, at very low field strengths, delayed activation may play a role. One of the proposed future avenues of research into the time-dependence of WEH would help answer this question.

The activated fraction $S(t)$ thus appears to have some explanatory and predictive power. Implementation of real-time monitoring of the fraction of excited tissue may help guide the selection of the number of AFP pulses and even of the pacing intervals: when the tissue is completely excited, AFP can be turned off and the whole tissue should return to its resting state, in which a normal rhythm can resume.

We hypothesized that the cardiovasculature observed in microCT scans of our tissue preparations are the anatomical structures recruited as wave emitting sites. With the help of scaling relations derived from our model of multisite activation of cardiac tissue,

we found that the activation dynamics in the rabbit heart predict a distribution of sizes that seems to match the cardiovasculature size distribution. Our simple activation model yielded an aspect ratio exponent $\gamma \approx 0.6$ in the rabbit heart, placing it between a 1d and a 3d system. This would seem strange, were it not for the corroboration of the onset time which we can only explain by invoking the presence of the ventricular septum. Our measurements of wave emission on the rabbit epicardium suggested that the septum may play an important role at low field strengths. We would like to pursue this further by excising the septum and directly measuring the activation dynamics on its surface.

To fully match structure and dynamics, it would also be better have not just the *relative* distribution of heterogeneity sizes but the absolute number of heterogeneities. This would provide the scale factor needed to match the density of sources expected from the activation model with the actual number of sources in the tissue.

In a broader context, we have also shown for the first time that fluorescence imaging of excitation waves in cardiac tissue can be used as an imaging technique for anatomical structure. Probing the tissue with electric field pulses of varying strengths allowed us to extract multi-scale anatomical information from the bulk of the tissue, in the form of the heterogeneity size distribution.

In chapter 5, we tested Far-Field Pacing (AFP) in canine ventricles and found an 81% reduction in pulse energy compared to single pulse defibrillation. With this pulse energy reduction, battery-powered implantable cardioverter-defibrillators (ICD) would not gain in longevity because of the multiple pulses required, but patients would benefit from reduced pain and discomfort. For this reason alone, we believe AFP is promising in terms of clinical application.

Our findings will be more valuable to the field of human medicine if we can identify clinically-available information equivalent to what can be obtained in the laboratory. To translate these ideas into clinically-relevant therapies, we have to identify quantities that

can be measured on a patient. The detailed information provided by optical mapping data is not available in the clinical setting. Therefore, equivalent measures will have to be found.

One such possibility is the QRS complex, the large deflection in a surface electrocardiogram (ECG) that corresponds to the depolarization of the ventricles. The shape and duration of the QRS complex may contain information similar to that revealed by the activated fraction $S(t)$. In response to a far-field pulse, a long QRS complex may indicate few sources while a shorter complex may indicate more. This may be one way to gauge the field strength required by individual patients in a clinical setting. Another possibility may be the local intracardiac electrogram, which has already been used to try to explain the success or failure of antitachycardia pacing [92]. The local intracardiac electrogram is recorded from catheter electrodes introduced into the patient's heart in order to monitor its activity in more detail.

In the next sections, we suggest future avenues of research that appear to us to be of most interest in light of our findings. All of them are in the planning stages already.

6.1 Activation model refinements

The activation model, in its simplicity, proved useful in predicting and interpreting the behaviour of the activation fraction and activation times in response to electric field pulses. To more accurately model multiple wave source activation, one could include anisotropic wave propagation and time-dependent activation of wave sources. The model of WEH assumed steady-state conditions: we need the spatially and temporally-resolved solution in order to account for delayed onset of activation. Another direction in which the model could be refined is to include more realistic heart geometries. We used rectangular geometries which are simple to simulate, but the heart surface is curved, and the endocardium is covered in anatomical features such as papillary muscles.

6.2 Time dependence of WES recruitment

One feature seen in the activation maps but which is not revealed by the activated fraction $S(t)$ is that a given WES, when triggered by a larger E, sometimes activated a larger area in the same time t after the pulse. Does this indicate that the individual source grows as E increases? The heterogeneity is not likely to grow substantially with E, but the size of the virtual electrode around it might (see figure 3.1 on page 57). According to the theory presented in section 3.1, the membrane depolarization e caused by the external current is a continuous scalar field around the heterogeneity. Its magnitude grows with E and decreases with distance r from the heterogeneity, as was shown in figure 3.1(c) on page 57. Thus a larger E extends the region of tissue where the induced depolarization exceeds the excitation threshold e^*. A larger initial WES would explain larger activated areas at later times. We could predict the area of tissue that is depolarized by an electric field E around a heterogeneity of size R by setting equations 3.3 equal to e^* and using R as the lower limit of integration. Then we would need an expression for the conduction velocity of an action potential from a small region of depolarized tisse. Perhaps the eikonal equation could be used here.

Additionally, in all our experiments we kept the pulse duration and waveform fixed: biphasic and 4 ms for rabbit heart experiments; monophasic and 5 ms in canine ventricle experiments. It would be of great benefit to measure the activation dynamics with different pulse durations and waveforms. These measurements could then be compared to predictions from numerical simulations of the time-dependence of WEH.

6.3 Reduced excitability

AFP was effective in terminating VF in canine ventricles but not in rabbit hearts. One hypothesis is that ischemia in the rabbit hearts reduced the tissue's excitability, increas-

ing the field strength required for WEH. However, this should also have increased the defibrillation threshold by the same factor, which was not the case. Thus, either the mechanism of defibrillation is less sensitive to excitability, or the wave dynamics during ischemia did not lend themselves to control from multiple sites. This may be the case if, as one article has suggested, ischemic VF is characterized by ectopic wave sources. Multisite pacing is useless in treating ectopic arrhythmias. To test this, we propose to create well-controlled ischemia-like conditions in canine ventricles and repeat the AF-P/defibrillation experiments. Also, we would carefully measure the dynamics of VF during ischemia for signatures of ectopic wave sources. One way to do this would be to look for breakthrough sites that recur at the same position during VF in the absence of any external current.

6.4 WEH as an imaging modality.

For low WES density simultaneous epi- and endocardial optical mapping may offer a way of mapping not only the (x, y)–location but also the z–depth of WES. These predictions could then be compared to bulk structure data to identify the structures that were recruited as WES by the electric field pulse.

Each pulse of electric field probes the structure of the tissue at a scale given by the electric field strength. The larger the field strength, the smaller the size of probed structures. By probing the tissue with far-field electrical pulses of varying strengths, we gain information about the positions and sizes of electrical heterogeneities inside the tissue.

The activation map may be thought of as an inverted landscape where the earliest times are peaks and the longest times are valleys. Every point (x, y) on the surface is eventually activated by a wave that emanated from a source. For each site, the activation

time tells us how far away the nearest source is located. Can this information be used to reconstruct the locations of the WES within the tissue?

The activation maps tell us more than just how long it takes for a wave to reach each point on the surface. Assuming linear wave propagation, the maps tell us how far away the nearest source lies from a point (x, y), namely $v_c \cdot T(x, y)$. From this perspective, the activation times "carve out" regions of tissue from which sources larger $r_{min}(E)$ are excluded. Thus the activation maps tell us where sources *are not*. The maps also tell us that there are no sources closer than the distance $v_c \cdot t_{activation}$ at that point.

The ability to resolve two sources separated by Δx at some depth z should be a function of two quantities: (a) the spatial resolution of the camera and (b) the time between successive exposures, scaled by the conduction velocity: $v_c \Delta t$.

BIBLIOGRAPHY

[1] A. Pumir and V. I. Krinsky, J. of Theor. Biol. **199**, 311 (1999).

[2] A. Pumir *et al.*, Phys. Rev. Lett. **99**, 208101 (2007).

[3] D. Shier, J. Butler, and R. Lewis, *Hole's Human Anatomy and Physiology, 8th ed.* (McGraw-Hill, Boston, 1999).

[4] I. R. Efimov, M. W. Kroll, and P. J. Tchou, *Cardiac Bioelectric Therapy: Mechanisms and Practical Implications* (Springer, New York, NY, 2008), p. 634.

[5] D. Hornung and S. Luther, BMT 2010 Proceedings 1 (2010).

[6] F. H. Fenton and A. Karma, Chaos **8**, 20 (1998).

[7] N. A. Trayanova, K. Skouibine, and F. Aguel, Chaos **8**, 221 (1998).

[8] M. Vaquero, D. Calvo, and J. Jalife, Heart Rhythm **5**, 872 (2008).

[9] F. X. Witkowski *et al.*, Nature **392**, 78 (1998).

[10] R. A. Gray, A. M. Pertsov, and J. Jalife, Nature **392**, 75 (1998).

[11] I. Aranson and L. Kramer, Rev. Mod. Phys. **74**, 99 (2002).

[12] E. Ben-Jacob, I. Cohen, and H. Levine, Adv Phys **49**, 395 (2000).

[13] E. Bodenschatz, W. Pesch, and G. Ahlers, Annu Rev Fluid Mech **32**, 709 (2000).

[14] S. Morris, E. Bodenschatz, D. Cannell, and G. Ahlers, Physica D **97**, 164 (1996).

[15] P. Coullet, L. Gil, and J. Lega, Phys. Rev. Lett. **62**, 1619 (1989).

[16] A. M. Zhabotinsky, Biofizika **9**, 306 (1964).

[17] B. P. Belousov, Collections of short papers on radiation medicine for 1958 (1959).

[18] B. J. Roth and J. P. Wikswo, IEEE Transactions on Biomedical Engineering **33**, 467 (1986).

[19] D. B. Geselowitz and W. T. Miller, Annals of Biomedical Engineering **11**, 191 (1983).

[20] V. S. Zykov, Biofizika **25**, 888 (1980).

[21] A. T. Winfree, *When Time Breaks Down: The Three-Dimensional Dynamics of Electrochemical Waves and Cardiac Arrhythmias* (Princeton University Press, Princeton, NJ, 1987).

[22] M. Cross and H. Greenside, *Pattern Formation and Dynamics in Nonequilibrium Systems* (Cambridge University Press, Cambridge, UK, 2009), p. 535.

[23] J. Keener and J. Sneyd, *Mathematical Physiology. 2 Vols.* (Springer, New York, NY, 2008), p. 1148.

[24] F. H. Fenton, E. M. Cherry, H. M. Hastings, and S. J. Evans, Chaos **12**, 852 (2002).

[25] D. P. Zipes *et al.*, Am J Cardiol **36**, 37 (1975).

[26] T. Shinbrot, C. Grebogi, E. Ott, and J. Yorke, Nature **363**, 411 (1993).

[27] E. Ott, C. Grebogi, and J. Yorke, Phys. Rev. Lett. **64**, 1196 (1990).

[28] D. J. Callans, Circulation **118**, 2488 (2008).

[29] S. J. Connolly, Am J Cardiol **84**, 90R (1999).

[30] D. S. Echt *et al.*, N Engl J Med **324**, 781 (1991).

[31] W. Krassowska and J. C. Neu, Biophys. J. **66**, 1768 (1994).

[32] E. A. Sobie, R. C. Susil, and L. Tung, Biophys. J. **73**, 1410 (1997).

[33] B. Roth and D. Beaudoin, Phys Rev E **67**, 051925 (2003).

[34] B. J. Roth and W. Krassowska, Chaos **8**, 204 (1998).

[35] B. Roth, Phys Rev E **55**, 1819 (1997).

[36] N. G. Sepulveda, B. J. Roth, and J. P. Wikswo, Biophys. J. **55**, 987 (1989).

[37] S. Alonso, F. Sagues, and A. S. Mikhailov, Science **299**, 1722 (2003).

[38] M. S. Wathen *et al.*, Circulation **110**, 2591 (2004).

[39] V. Krinsky, Prob. Cybernetics **20**, 59 (1968).

[40] A. Stamp, G. Osipov, and J. Collins, Chaos **12**, 931 (2002).

[41] G. Sivagangabalan *et al.*, Pacing and Clinical Electrophysiology **31**, 1095 (2008).

[42] M. A. Allessie *et al.*, Circulation **84**, 1689 (1991).

[43] J. J. Fox *et al.*, NJP **5**, 101 (2003).

[44] J. J. Fox *et al.*, Circ. Res. **90**, 289 (2002).

[45] J. J. Fox, J. McHarg, and R. F. Gilmour, AJP-Heart Circ. Physiol. **282**, H516 (2002).

[46] J. J. Fox, R. F. Gilmour, and E. Bodenschatz, Phys. Rev. Lett. **89**, 198101 (2002).

[47] M. L. Koller, M. L. Riccio, and R. F. Gilmour, Am J Physiol **275**, H1635 (1998).

[48] A. R. M. Gelzer *et al.*, Circulation **118**, 1123 (2008).

[49] P. L. Johnson *et al.*, Annals of Biomedical Engineering **30**, 180 (2002).

[50] S. Saksena *et al.*, Am J Cardiol **76**, 913 (1995).

[51] G. P. Walcott, C. R. Killingsworth, and R. E. Ideker, Resuscitation **59**, 59 (2003).

[52] P. Bittihn *et al.*, Philos T R Soc A **368**, 2221 (2010).

[53] P. Bittihn *et al.*, NJP **10**, 103012 (2008).

[54] C. M. Ripplinger, V. I. Krinsky, V. P. Nikolski, and I. R. Efimov, AJP-Heart Circ. Physiol. **291**, H184 (2006).

[55] W. Li, C. M. Ripplinger, Q. Lou, and I. R. Efimov, Heart Rhythm **6**, 1020 (2009).

[56] F. H. Fenton *et al.*, Circulation **120**, 467 (2009).

[57] S. Luther *et al.*, in preparation (2010).

[58] R. J. Sweeney, R. M. Gill, J. L. Jones, and P. R. Reid, J. Card. Elec. **7**, 134 (1996).

[59] L. M. Loew and L. L. Simpson, Biophys. J. **34**, 353 (1981).

[60] E. Fluhler, V. Burnham, and L. Loew, Biochemistry **24**, 5749 (1985).

[61] L. M. Loew *et al.*, Journal of Membrane Biology **130**, 1 (1992).

[62] V. V. Fedorov *et al.*, Heart Rhythm **4**, 619 (2007).

[63] L. C. Baker *et al.*, AJP-Heart Circ. Physiol. **287**, H1771 (2004).

[64] J. M. Davidenko *et al.*, Nature **355**, 349 (1992).

[65] J. P. Wikswo, S. F. Lin, and R. A. Abbas, Biophys. J. **69**, 2195 (1995).

[66] S. Lin, R. Abbas, and J. P. Wikswo, Rev Sci Instrum **68**, 213 (1997).

[67] I. R. Efimov, V. P. Nikolski, and G. Salama, Circ. Res. **95**, 21 (2004).

[68] D. W. Evertson *et al.*, IEEE Transactions on Biomedical Engineering **55**, 1241 (2008).

[69] C. M. Ripplinger *et al.*, Heart Rhythm **6**, 87 (2009).

[70] M. L. Riccio, M. L. Koller, and R. F. Gilmour, Circ. Res. **84**, 955 (1999).

[71] F. Qu *et al.*, Journal of Biomedical Optics **12**, 044019 (2007).

[72] M. Kay, P. Amison, and J. Rogers, IEEE Transactions on Biomedical Engineering **51**, 1219 (2004).

[73] S. Lin and J. P. Wikswo, J Biomed Opt **4**, 200 (1999).

[74] M. Kondo, V. Nesterenko, and C. Antzelevitch, Cardiovascular research **63**, 635 (2004).

[75] D. Mackenzie, Science **303**, 786 (2004).

[76] C. W. Zemlin, S. Mironov, and A. M. Pertsov, Cardiovasc. Res. **69**, 98 (2006).

[77] O. F. Sharifov, R. E. Ideker, and V. G. Fast, Cardiovasc. Res. **64**, 448 (2004).

[78] V. G. Fast, S. Rohr, A. M. Gillis, and A. G. Kleber, Circ. Res. **82**, 375 (1998).

[79] D. A. Hooks *et al.*, Circ. Res. **91**, 331 (2002).

[80] I. J. LeGrice *et al.*, Am J Physiol **269**, H571 (1995).

[81] S. Takagi *et al.*, J. of Theor. Biol. **230**, 489 (2004).

[82] A. G. Kléber and C. B. Riegger, J Physiol (Lond) **385**, 307 (1987).

[83] S. Weidmann, J Physiol (Lond) **210**, 1041 (1970).

[84] J. Keener, Journal of mathematical biology **29**, 629 (1991).

[85] O. F. Sharifov and V. G. Fast, J. Card. Elec. **14**, 1215 (2003).

[86] A. Arutunyan, L. M. Swift, and N. Sarvazyan, AJP-Heart Circ. Physiol. **283**, H741 (2002).

[87] M. Hiraoka *et al.*, Jpn Heart J **37**, 693 (1996).

[88] J. N. Weiss and K. I. Shine, Am J Physiol **242**, H619 (1982).

[89] J. N. Weiss and K. I. Shine, J Mol Cell Cardiol **13**, 699 (1981).

[90] T.-J. Wu *et al.*, Circ J **73**, 1803 (2009).

[91] J. Caldwell, F. L. Burton, G. L. Smith, and S. M. Cobbe, J. Card. Elec. **18**, 854 (2007).

[92] H. S. Lim, M. Lencioni, and H. Marshall, Pacing and Clinical Electrophysiology **33**, 549 (2009).